C02018: Doctor of Philosophy *CRICOS Code: 036570B*

June 10, 2020

Analog Least Mean Square Loop

for Self-Interference Cancellation in In-Band Full-Duplex Radios

---

Anh Tuyen Le

School of Electrical and Data Engineering
Faculty of Engg. & IT
University of Technology Sydney
NSW - 2007, Australia

Analog Least Mean Square Loop

for Self-Interference Cancellation in In-Band Full-Duplex Radios

A thesis submitted in partial fulfilment of the requirements
for the degree of

Doctor of Philosophy
in
Engineering

by

Anh Tuyen Le

to

School of Electrical and Data Engineering
Faculty of Engineering and IT
University of Technology Sydney
NSW - 2007, Australia

June 2020

AUTHOR'S DECLARATION

I, *Anh Tuyen Le* declare that this thesis, submitted in partial fulfilment of the requirements for the award of Doctor of Philosophy, in the *School of Electrical and Data Engineering*, *Faculty of Engineering and IT* at the University of Technology Sydney, Australia, is wholly my own work unless otherwise referenced or acknowledged. In addition, I certify that all information sources and literature used are indicated in the thesis. This document has not been submitted for qualifications at any other academic institution. This research is supported by the Australian Government Research Training Program.

SIGNATURE: Production Note: Signature removed prior to publication.

[Anh Tuyen Le]

DATE:JUNE 10, 2020

PLACE: Sydney, Australia

ACKNOWLEDGMENTS

First of all, I would like to express my deepest gratitude to my supervisor, Prof. Xiaojing Huang, for his endless guidance and great support throughout my PhD study. Prof. Huang has provided me an excellent research environment and has given me insightful advice and brilliant ideas. His great knowledge on mathematics and electronics has broaden my view on the link from theory to practice. He has also provided me the opportunity to learn from industrial experts by participating in his projects.

I would like to appreciate my co-supervisor, Dr. Le Chung Tran from University of Wollongong, for his essential guidance for my study. His invaluable comments and great encouragement have helped me to overcome many challenges in this study. I am thankful Dr. Tran for providing me the opportunity to take part in his research project which broaden my view to related fields.

I highly acknowledge Australian Research Council and University of Technology Sydney for providing me with the scholarships. Therefore, I could realize my dream about studying in an advanced education system like Australia's one.

I would like to thank Distinguished Prof. Yingjie Jay Guo, the Director of Global Big Data Technologies Centre (GBDTC) for his support and encouragement during my study. I also appreciate the staffs and fellow doctoral students at GBDTC, especially Mr. Hao Zhang, Mr. Yijang Nan, Miss. Haihan Sun, Ms. Gennie Tan, and Ms. Katie Gypsiotis for their kind helps and supports. I also acknowledge Chandranath Adak (UTS) for providing this thesis template.

A special thanks to my beloved wife, Phan Thi Thanh Huong, and my little girls, Le Phan Ngoc Anh, Le Phan Ngoc Linh. I am deeply grateful my wife for looking after our small family and taking care of our parents when I am studying. As a PhD in science, she shares with me the challenges of this journey, and always cheers me up when I face the difficulties. Their wonderful love and support provided me with an unlimited strength and faith so that I can achieve my academic goals.

List of Publications

Journals:

1. **A. T. Le**, L.C. Tran, X. Huang, and Y. J. Guo, “Beam-Based Analog Self-Interference Cancellation in Full-Duplex MIMO Systems," *IEEE Transactions on Wireless Communications*, vol. 19, no. 4, pp. 2460 - 2471, April 2020.

2. **A. T. Le**, L.C. Tran, X. Huang, and Y. J. Guo, “Analog least mean square loop for self-interference cancellation: A Practical Perspective," *Sensors*, vol. 20, no. 1, pp. 1-15, Jan. 2020.

3. **A. T. Le**, L.C. Tran, X. Huang, and Y. J. Guo, “Analog least mean square loop with I/Q imbalance for self-interference cancellation in full-duplex radios", *IEEE Transactions on Vehicular Technology*, vol. 68, no. 10, pp. 9848 - 9860, Aug. 2019.

4. **A. T. Le**, L.C. Tran, X. Huang, Y. J. Guo, and J. Vardaxoglou,“Frequency domain characterization and performance bounds of ALMS loop for RF self-interference cancellation", *IEEE Transactions on Communications*, vol. 67, no. 1, pp. 682-692, Jan. 2019.

5. **A. T. Le**, L.C. Tran and X. Huang, “Cyclostationary analysis of analog least mean square loop for self-interference cancellation in in-band full-duplex systems", *IEEE Communication Letters*, vol. 21, no. 12, pp. 2738-2741, Sept. 2017.

Conferences:

6. **A. T. Le**, L.C. Tran, X. Huang, and Y. J. Guo, “Analog least mean square loop for self-interference cancellation: Implementation and measurements," in *Proceedings of 29th International Telecommunication Networks Application Conference (ITNAC)*, Aukland, New Zealand, Nov. 2019, pp. 1-5 (Best Student Paper Award)

7. **A. T. Le**, L.C. Tran, X. Huang, and Y. J. Guo, “Beam-based analog self-interference cancellation with auxiliary transmit chains in full-duplex MIMO systems," *Proceedings of 2019 IEEE 20th International Workshop on Signal Processing Advances in Wireless Communications (SPAWC)*, Cannes, France, July 2019, pp. 1-5

8. **A. T. Le**, L.C. Tran, X. Huang, Y. J. Guo, and J. Vardaxoglou,“Analog least mean square loop for self-interference cancellation in generalized continuous wave SAR," in *Proceedings of 88th IEEE Vehicular Technology Conference (VTC Spring)*, Chicago, USA, 2018, pp. 1-5

9. **A. T. Le**, L. C. Tran, and X. Huang, “On performance of analog least mean square loop for self-interference cancellation in in-band full-duplex OFDM systems," in Proceedings of 85th IEEE Vehicular Technology Conference (VTC Spring), Sydney, Australia, 2017, pp. 1-5.

TABLE OF CONTENTS

List of Publications iii

List of Figures ix

List of Tables xii

List of Abbreviations xiii

List of Symbols xv

Abstract xvii

1 Introduction 1

1.1 Background 1

1.1.1 In-Band Full-Duplex Operation 1

1.1.2 Self-Interference 2

1.2 Motivation and Contribution 4

1.3 Thesis Outline 7

2 Literature Review 9

2.1 Self-Interference Mitigation 9

2.1.1 Propagation Domain Suppression 9

2.1.2 Digital Self-Interference Cancellation 11

2.1.3 Radio Frequency Domain Cancellation 13

2.2 Least Mean Square Algorithm 15

2.3 Analog Least Mean Square Loop 17

3 ALMS Loop with Different Signal Properties 21

3.1 ALMS Loop for OFDM Systems 21

3.1.1 OFDM System Model 21

3.1.2 Cyclostationary Analysis 22
3.1.3 Simulation Results 26
3.2 Single-Carrier and Multi-Carrier IBFD Systems 27
3.2.1 Signal Models 28
3.2.2 General Solution of Weighting Error Function 30
3.2.3 Conclusion 34
3.3 ALMS Loop with Deterministic Signal in FD SAR 34
3.3.1 Introduction 34
3.3.2 GCW-SAR Signal Model 36
3.3.3 Stationary Analysis 38
3.3.4 Simulation Results 41
3.3.5 Conclusion 43

4 Frequency Domain Characterization and Performance Bounds of ALMS Loop 45
4.1 Introduction 45
4.2 Steady State Analysis of ALMS Loop 46
4.2.1 Signal Models 46
4.2.2 Steady State Analysis 48
4.3 Frequency-Domain Analysis of Residual SI 52
4.3.1 Eigen-Decomposition of Autocorrelation Matrices 52
4.3.2 Frequency Domain Characterization of ALMS Loop 54
4.3.3 Performance Lower Bounds 55
4.4 Simulation Results 58
4.5 Conclusion 59

5 ALMS Loop with IQ Imbalance 61
5.1 Introduction 61
5.2 System Architecture and Signal Models 62
5.2.1 In-Band Full-Duplex Transceiver with ALMS Loop 62
5.2.2 I/Q Imbalanced Signal Models 64
5.3 Effects of I/Q Imbalance 65
5.3.1 Impact on Loop Gain 65
5.3.2 Impact on Cancellation Performance 67
5.4 Simulation Results 74
5.5 Conclusion 77

6 ALMS Loop for In-Band Full-Duplex MIMO Systems **79**
6.1 Introduction . . . 79
6.2 Principle of Beam-Based Analog SIC . . . 81
6.2.1 Beam-Based SIC . . . 81
6.2.2 ALMS Loop . . . 84
6.3 Stationary Analysis . . . 85
6.3.1 Cancellation Performance . . . 85
6.4 Reference Signals Generation . . . 90
6.4.1 Using Additional Transmit Chains . . . 90
6.4.2 Selecting from Transmitted Signals . . . 92
6.5 Conclusion . . . 98

7 ALMS Loop - A Practical Perspective **99**
7.1 Introduction . . . 99
7.2 Related Works . . . 100
7.2.1 Analog Multi-Tap Adaptive Filters . . . 100
7.2.2 ALMS Loop . . . 102
7.3 Implementation of ALMS loop . . . 103
7.4 Measurement Results . . . 106
7.4.1 Measurement Setup . . . 106
7.4.2 Measurement Results . . . 107
7.5 Conclusion . . . 109

8 Conclusion and Future Work **113**
8.1 Conclusion . . . 113
8.2 Future Work . . . 115

A Appendix **117**
A.1 Proof of Constant $E_h\{H(e^{j\omega_k})\}$ . . . 117
A.2 Derivation of $ISRLB_a$ and $ISRLB_d$ . . . 117
A.2.1 $ISRLB_a$ . . . 117
A.2.2 $ISRLB_d$ . . . 118
A.3 Derivation of Residual SI Power . . . 120
A.4 Solution of Steady-State Weighting Error Function . . . 121
A.5 Derivation of Modeling Error . . . 124
A.6 Derivation of Weighting Error Functions . . . 125

Bibliography **129**

LIST OF FIGURES

FIGURE **Page**

1.1 IBFD radio terminal. 3
1.2 SI components and the requirements of SIC. 3
1.3 Three steps of SIC. 4
1.4 Five researches problems. 5

2.1 Propagation domain passive approaches: (a) Physical separation; (b) Spatial separation; (c) Antiphase control; (d) Cross-polarization. 10
2.2 Amount of suppression by antenna separation at 2.45 GHz. 10
2.3 Digital cancellation using channel modelling methods 12
2.4 RF domain SIC approaches: (a) Additional transmit chain; (b) Multi-tap adaptive filter. 13
2.5 Multi-tap filter SIC techniques: (a) Time-domain approaches; (b) Frequency-domain approaches. 14
2.6 One tap of a closed-loop multi-tap filter. 15
2.7 L-tap transversal adaptive filter structure. 16
2.8 L-tap transversal continuous-time adaptive filter structure. 17
2.9 ALMS loop structure. 19
2.10 Earlier research on ALMS loop. 20

3.1 $g(t,\tau)$ with $T_o = 80T_s$ and pulse shaping roll-off factor 0.25. 23
3.2 (a) Normalized weight error; and (b) Normalized weight error variation. . . . 24
3.3 ISRLB versus αT_s with various windowing roll-off factors β_o. 25
3.4 Simulated and theoretical weighting coefficients of ALMS loop with T_s spacing. 27
3.5 Simulated and theoretical convergence curves for residual interference power of the ALMS loop with T_s and $T_s/2$ spacing in the first scenario. 28
3.6 (a) Normalized weight error; and (b) Normalized weight error variation with the loop gain $\mu A^2 = 1000$, $\alpha T_s = 0.003$, $T_o = 80T_s$, and $\beta_s = \beta_o = 0.25$ 33
3.7 ISRLB of the two systems with various values of β_s and β_o. 34
3.8 The autocorrelation function of $P(t)$ with chirp rate $k_r = 2.5 \times 10^{12}$. 39
3.9 The residual SI power in the first scenario for $T_d = 1/nB$, with $n = 1$, 2 and $L = 4$, 8, respectively. 42

3.10 The residual SI power in the second scenario for $T_d = 1/nB$ with $n = 1, 2,$ and $L = 4, 8,$ respectively. 43

4.1 The ALMS loop structure. 47
4.2 (a) Raised cosine spectrum; (b) $S_X(e^{j\omega})$; (c) $S_X(e^{j\omega_k})$ versus eigenvalues λ_k, with $L = 256$, $A^2 = 100$, $\beta = 0.2$, $T_d = T_s/2$, $T_s = 1$. 53
4.3 Frequency dependent attenuation factors with various values of β, $L = 256$, $A^2 = 100$, $T_d = T_s/2$. 55
4.4 ISR lower bounds versus β with $a = 2000, 2200,$ and 2500. 57
4.5 PSDs of the SI $Z(t)$, residual SI $V(t)$, and residual SI after the matched filter $\tilde{V}(t)$ with $\beta = 0.5$, $\mu A^2 = 1000$, $T_d = T_s/2$, and $L = 8$. 59
4.6 ISRs in the analog domain and digital domain versus β with $\mu A^2 = 1000$, $T_d = T_s/2$. 60

5.1 The ALMS loop structure. 63
5.2 The loop gain ratio versus amplitude. 67
5.3 The normalized autocorrelation function of the transmitted signals. 68
5.4 $\overline{DF}$ versus amplitude and phase errors with different β for $L = 8$ and (a) $f_c = 2432$ MHz and (b) $f_c = 5200$ MHz. 71
5.5 $\overline{DF}$ versus amplitude and phase errors with different L for $\beta = 0.25$ and (a) $f_c = 2432$ MHz and (b) $f_c = 5200$ MHz. 72
5.6 DF versus amplitude and phase errors when $\beta = 0$ and $T_d = T_s$. 75
5.7 The complex signals $x_1(t)$ and $x_2(t)$ with $\rho_1 = \rho_2 = 3$ dB, $\theta_1 = \theta_2 = 5°$. 76
5.8 Residual SI powers in single-carrier system with $\rho_1 = \rho_2 = 3$ dB, $\theta_1 = \theta_2 = 5°$ and (a) $f_c = 2432$ MHz and (b) and $f_c = 5200$ MHz. 76
5.9 Residual SI powers in OFDM system with $\rho_1 = \rho_2 = 3$ dB, $\theta_1 = \theta_2 = 5°$ and (a) $f_c = 2432$ MHz and (b) $f_c = 5200$ MHz. 77

6.1 Proposed beam-based analog SIC structure. 82
6.2 ALMS loop for beam-based cancellation structure. 84
6.3 Beam-based analog SIC with auxilary transmit chains. 90
6.4 The averaged and converged interference suppression ratio. 91
6.5 Normalized SI and residual SI powers for (a) 8×8 IBFD MIMO systems and (b) 2 beams IBFD MIMO systems. 92
6.6 Proposed beam-based analog SIC structure. 93
6.7 Transformation from $\underline{\mathbf{h}}$ to $\bar{\tilde{\mathbf{u}}}$. 93

6.8 (a) Geometric mean of D_Ω and (b) ISR for all possible selections of $\mathbf{A}_r$ 95
6.9 SI channel impulse response $h_{2,4}(t)$ (top) and modeled tap coefficients $h_{2,4}(l)$ (bottom) for (a) arbitrary and (b) T_d spaced delay between multipaths. 96
6.10 Interference suppression ratio under (a) arbitrary delay interference channel and (b) T_d spaced interference chanel. 97
6.11 Interference suppression ratio with the worst reference signals. 97

7.1 Multi-tap adaptive filter structure. 101
7.2 Output spectra of (a) a multiplier or a modulator with an LPF and (b) an unfiltered modulator. 103
7.3 A practical structure of the ALMS loop. 104
7.4 Prototype of the ALMS loop and a part of the receiver. 105
7.5 The measurement setup. 107
7.6 Measurement results for 20 MHz bandwidth. 108
7.7 Measurement results for 50 MHz bandwidth. 109
7.8 Cancellation performances with different roll-off factors. 110
7.9 Cancellation performances with OFDM signal. 110

List of Tables

Table **Page**

6.1 Comparison with existing methods for IBFD MIMO 98

7.1 Comparison of existing multi-tap adaptive filters 101
7.2 Summary of publications on ALMS loops 102

List of abbreviations

ADC Analog-to-Digital Converter

AGC Automatic Gain Control

ALMS Analog Least Mean Square

AP Access Point

BPF Bandpass Filter

CSI Channel State Information

CW Continuous Wave

DF Degradation Factor

DFT Discrete Fourier Transform

DSP Digital Signal Processing

FPGA Field Programmable Gate Array

GCW-SAR Generalized Continuous Wave Synthetic Aperture Radar

I/Q In-phase/ Quadrature

IBFD In-band Full-duplex

IC Integrated Circuits

ISR Interference suppression Ratio

ISRLB Interference suppression Ratio Lower Bound

LMS Least Mean Square

LO Local Oscillation

MIMO Multiple Input Multiple Output

ODE Ordinary Differential Equation

OFDM Orthogonal Frequency-Division Multiplexing

PA Power Amplifier

RC Resistor-Capacitor

RF Radio Frequecy

RRC Root-raised Cosine

Rx Receive

SAR Synthetic Aperture Radar

SI Self-Interference

SIC Self-Interference Cancellation

SISO Single Input Single Output

Tx Transmit

LIST OF SYMBOLS

$\mathbf{A}$ The beamforming matrix

a_i The i-th complex data symbol

α Decay constant of the lowpass filter

$\mathbb{C}$ The complex set

h_l The l-tap of the modelled SI channel coefficient

$\mathbf{H}(l)$ The SI channel coefficient matrix in IBFD MIMO systems

$h(t)$ The real SI channel impulse response

$\mathbf{I}_M$ The identity matrix of order M

$\otimes$ The Kronecker product

L The total number of taps in the ALMS loop

$\mathbf{\Lambda}$ The diagonal matrix composed by eigenvalues of the autocorrelation matrix

λ_l The l-th eigenvalue of the autocorrelation matrix

μ The LNA gain

$n(t)$ The additive Gaussian noise

$P_{d_m}(t)$ The residual signal power at the m-th receiver chain

$\Phi(\tau)$ The autocorrelation funtion of transmitted signal

$\mathbf{\Phi}$ The autocorrelation matrix of transmitted signal

$p(t)$ Transmit pulse shaping filter

$\mathbf{Q}$ The orthonormal modal matrix composed by eigenvectors of the autocorrelation matrix

$s(t)$ The signal of interest

T_d The delay unit between two adjacent taps

T_s The transmitted symbol duration

$u_l(t)$ The weighting error function

V_X Root mean square amplitude of the transmitted signal

$x(t)$ Transmitted RF signal

$z(t)$ Self-interference RF signal

Abstract

Recently, In-band full-duplex (IBFD) transmission, which allows transceivers to transmit and receive simultaneously on a single frequency band, is regarded as a promising solution for the problem of frequency spectrum shortage. However, a fundamental challenge encountered in realizing IBFD communications is self-interference (SI), which is the strong interference imposed by the transmitter blocking its co-located receiver from the signal of interest. Therefore, to enable the IBFD mode, great efforts have been devoted to mitigate SI to beyond the noise floor level. Among various approaches proposed in the radio frequency (RF) domain, analog least mean square (ALMS) loop is a promising structure for SI cancellation (SIC) due to its simplicity and efficiency. However, the behaviours of the ALMS loop have not been fully understood and its application was proposed for single-carrier and single antenna IBFD communication systems only.

This study aims at tackling the problem of SI in the RF domain for various IBFD systems using the ALMS loop. The contributions of this thesis are as follows. Firstly, the performances of the ALMS loop with different transmitted signals is investigated. It shows that due to the cyclostationary effect of the transmitted signals, SI cannot be removed completely by the ALMS loop but there exists an irreducible SI. The lower bounds of this irreducible SI are derived for both single-carrier and multi-carrier IBFD systems. Additionally, it proves that the ALMS loop also performs well with deterministic signals in full-duplex synthetic aperture radars. Secondly, by characterizing the ALMS loop in the frequency domain, the achievable levels of SIC by the ALMS loop in both

analog and digital domains are revealed. Thirdly, the performance of the ALMS loop under hardware impairment conditions is investigated. More importantly, a degradation bound is found to determine how much of compensation should be obtained from other means of SI mitigation for a given level of imperfection. Fourthly, a novel beam-based analog SIC structure employing the ALMS loop is proposed for IBFD multiple input multiple output (MIMO) systems to significantly reduce the number of adaptive filters required for SIC in IBFD MIMO systems. Finally, a practical structure of the ALMS loop is proposed and a prototype is implemented using off-the-shelf components to provide experimental results confirming all the theoretical findings. The analyses and practical results in this thesis provide a comprehensive view of the ALMS loop and prove its potential application for SIC in different IBFD radios.

CHAPTER 1

INTRODUCTION

1.1 Background

1.1.1 In-Band Full-Duplex Operation

Wireless communication plays a crucial role in our lives. People, vehicles and devices are all surrounded by radio signals serving the demands of communications, entertainment, safety, control and so on. It is forecasted that the number of networked devices and connections will be up to 27.1 billions in 2021 [1]. In addition, wider bandwidth allocated for each connection is also demanded. Nowadays, communications include not only voice call and text messages, but also video conferencing, streamlines, data sharing and so on. However, radio spectrum, the medium of wireless transmission remains unchanged and hence becomes a bottleneck for the growth of wireless communication. Therefore, spectral resource must be exploited more efficiently. Currently, wireless devices operate in the half-duplex mode in which two different frequency bands are required to transmit and receive. Otherwise, if only a single frequency band is allocated, the transceiver has to transmit and receive at different time slots. Therefore, to enhance the efficiency of spectral exploitation, in-band full-duplex (IBFD) operation has been proposed. In this mode, only one frequency band is required for a pair of transceivers to communicate simultaneously. Since IBFD can double channel capacity, it is determined as one of the key technologies for the fifth generation (5G) mobile network [2].

Beside doubling channel capacity, IBFD transmission is also beneficial in various

applications. Firstly, for a multi-hop network, an IBFD relay node can forward the receiving packets. Therefore, transmission delay can be significantly reduced compared to that of a half-duplex counterpart. Secondly, in a cognitive radio network, a secondary user can easily recognize the appearance of the primary user by sensing while transmitting. As a result, the secondary user will not interfere with the primary one, and collision will be avoided [3]. Another advantage of this innovation can be found in cellular networks where IBFD allows to reduce the interference from the same frequency cells. Hence, the distance between the same frequency cells can be reduced. IBFD can also help to solve the hidden terminal problem in multiple access networks. Considering a scenario of multiple nodes having data in their buffer for direct transmission to and reception from a common access point (AP). If a node starts transmitting its data to the AP and the AP simultaneously starts transmitting data back to this node, the other nodes will hear the transmissions from the AP and delay their transmissions to avoid collisions. Even if the AP has no data to send back to the first node, it still repeats an “ACK" for that node so as to prevent the other nodes from transmitting [4]. Finally, IBFD is expected to be a key advantage in military operations because this technology can be used in a joint jammer and communication system which can make an electronic attack to opponents while intercepting the signal of interest [5].

1.1.2 Self-Interference

Over decades, IBFD was believed to be impossible as stated in [6] because of interference. Due to the IBFD operation, the transmitted signal interferes to its co-located receiver, so called self-interference (SI), by propagating over a very short distance (in separated antenna case) and being reflected from the surrounding obstacles. Since the SI power is much higher than that of the signal of interest, it can saturate or even damage the receiver and hence, blocks the receiver from the desired signal. The problem of SI is demonstrated in Fig. 1.1 [7].

Obviously, removing SI is a fundamental problem to enable the IBFD mode. Since SI has the same frequency as the desired signal, it cannot be removed by a traditional band-pass filter as in half-duplex systems. Instead, some mechanisms are required to mitigate the level of SI to below the noise floor before decoding the received signal. As an example, the requirement of SI cancellation (SIC) for a WIFI system is presented in Fig. 1.2 [8]. Particularly, in a WIFI system, the transmit power is 20 dBm, while the receiver noise floor is approximately -90 dBm. To enable the IBFD mode, at least 110 dB of SIC must be obtained to reduce the SI below the level of noise floor. However, realizing

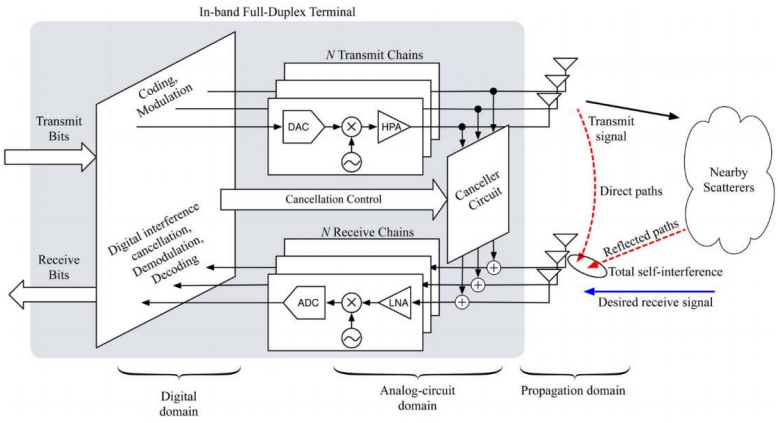

Figure 1.1: IBFD radio terminal.

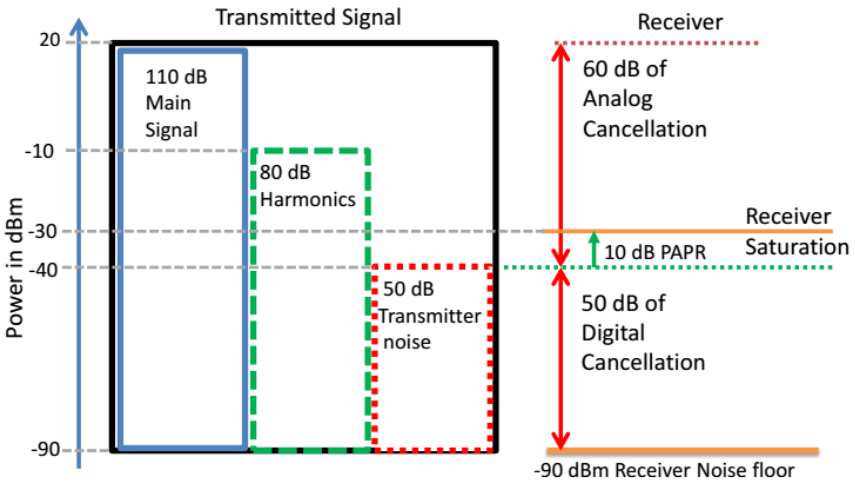

Figure 1.2: SI components and the requirements of SIC.

such 110 dB of SIC is very challenged since the SI is unknown. Although the digital baseband signal is known by the transmitter, the radio frequency (RF) transmitted signal is quite different from its baseband incarnation because analog components in the radio transmit chain affect the signal in both linear and non-linear ways. For example, the power amplifiers can distort the signal by generating the high-order components and add more noise. The RF signal can also be slightly inaccurate due to the local oscillator which may have frequency shift or phase noise. As a result, the RF transmitted signal includes the up-converted version of the baseband signal, the high order components as well as unknown transmitter noise.

In order to tackle the problem of SI, intensive researches have been conducted us-

ing many different approaches which can be categorized into three steps including propagation-domain suppression, analog domain domain, and digital domain cancellation [7] as depicted in Fig. 1.3. Particularly, propagation domain approaches intend to

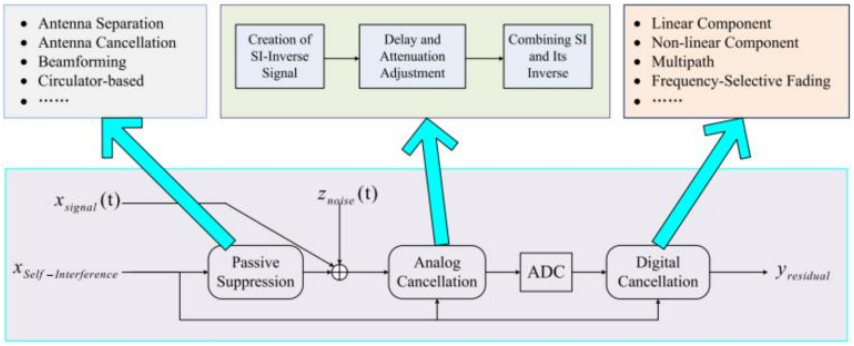

Figure 1.3: Three steps of SIC.

suppress the level of SI at the input of receive antenna. Analog domain cancellation methods, which can be implemented in RF stage or intermediate frequency stage, aim to generate a signal mimicking SI to subtract it from the received signal. Digital domain cancellation employed the knowledge of clean transmitted data from the transmitter side to estimate the digitized SI. Obviously, to achieve the requirement of SIC, two or three steps of SI mitigation must be combined.

1.2 Motivation and Contribution

With many great potential benefits, IBFD is one of the key technologies for future wireless communications. However, to make this scheme practical, great efforts need to be devoted to tackle the fundamental problem of SIC. As indicated before, since SI is unknown, suppressing it to below the level of noise floor is challenged especially when considering other factors such as device size, power consumption, implementation cost, and complexity.

Among various SI mitigation approaches in the literature, analog least mean square (ALMS) loop proposed in [9] is a promising structure to sufficiently cancel SI in the radio frequency domain with low complexity. By using a low-pass filter to replace an ideal integrator, the ALMS loop forms an adaptive filter without any requirement of digital signal processing and channel state information.

This thesis aims at investigating the behaviors of the ALMS loop and adopting it in any IBFD systems. To achieve this ultimate goal, there are five research problems left

from [9] need to be tackled as shown in Fig.1.4. The first problem is the consideration

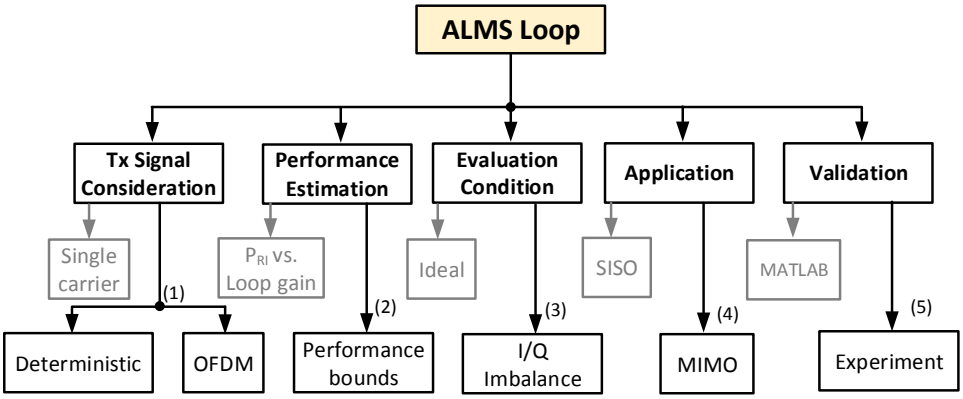

Figure 1.4: Five researches problems.

of transmitted signal properties on the performance of the ALMS loop. In [9], single-carrier signalling has been investigated. In this thesis, the analyses are extended to multi-carrier signalling such as orthogonal frequency-division multiplexing (OFDM) which is commonly used in WIFI systems, and deterministic chirp signals in radar. Secondly, the performance lower bounds in both RF and digital domains are derived to estimate the level of cancellation given by the ALMS loop. Thirdly, the problem of in-phase/quadrature (I/Q) imbalance occurred in the structure is considered to identify its impact on the performance of the ALMS loop. Next, the problem of how to adopt this adaptive filter in IBFD MIMO systems is investigated. Finally, the challenge in implementing the ALMS loop using off-the-shelf components and obtaining the practical results is tackled to validate the theoretical analyses.

The contributions of this thesis are summarized as follows. Firstly, it shows that the ALMS loop can work with both single-carrier and multi-carrier signallings. By proposing a general solution of the weighting error function, this thesis provides a tool to examine the performance of the ALMS loop with any transmitted signals which satisfy a given condition. Using this solution, it shows that the weighting error function of the ALMS loop in case of OFDM signal has wider variation range compared to that in single-carrier systems. As a result, the irreducible interference suppression lower bound is potentially much smaller compared to that in OFDM systems. In addition, the investigation of the ALMS loop with chirp signals provides a design guide for this structure so that it can be applied in full-duplex synthetic aperture radar systems.

Secondly, a simulation result in [9] shows that the ALMS loop amplifies the high frequency components at the edge of residual signal spectrum, yet this phenomenon has not been investigated. By analyzing the residual SI power in the frequency domain, the attenuation factor which causes this effect is identified. Furthermore, by considering the residual SI at both RF domain and digital domain, it is shown that this effect will be removed by the matched filter. Thus, the level of cancellation will be much higher considering at the digital domain. Then, by deriving the interference suppression lower bounds, a formula is provided to estimate the level of cancellation achieved by the ALMS loop from its parameters and transmitted signal properties such as the roll-off factor of the transmit pulse shaping filter and its power.

Thirdly, taking into account the problem of I/Q imbalance within the ALMS loop, this thesis shows that I/Q imbalance leads to the change of loop gain but it can be easily compensated by adjusting the gain at the LNA. In addition, stationary analysis quantifies the impact on the level of cancellation by a degradation factor and proves that the ALMS loop is robust to the frequency-independent I/Q imbalance. More importantly, by revealing the upper bound of the degradation factor, it provides a means to define how much compensation from other SIC stages is required for a given level of I/Q imbalances.

Fourthly, a novel beam-based analog SIC structure is proposed to significantly reduce the hardware complexity for IBFD MIMO systems. In an $N \times N$ IBDF system, the SI appearing at each receive chain are from N transmitters so that conventional N^2 adaptive filters are required. If the adaptive filter involves digital signal processing (DSP) to update its tap weights, the DSP complexity also increases quadratically compared to that in single antenna systems. The proposed structure can reduce the number of adaptive filters to linearly scale with the number of transmitted beams. An algorithm to select reference signals for the ALMS loops is also developed to further simplify the structure.

Finally, a practical structure of the ALMS loop is proposed to implement using off-the-self components. Based on this structure, a prototype of the ALMS loop with two taps has been developed to provide some experimental results. Particularly, measurement results with different signal bandwidths are about 3 dB lower than the estimated levels calculated from theoretical analyses which are only obtained with much higher number of taps. The experiments with different roll-off factors and an OFDM signal confirm the conclusions drawn from the first research problem.

1.3 Thesis Outline

Chapter 1 introduces the background information about IBFD operations and the problem of SIC in realizing this mode. Research motivation and contributions are then presented in this chapter.

Chapter 2 reviews the state-of-the-art approaches proposed in the literature to mitigate SI. This chapter also presents the background of the LMS algorithm and how the ALMS loop is developed from this technique.

Chapter 3 presents the study on the impact of transmitted signal property on the performance of the ALMS loop.

Chapter 4 evaluates the behaviors of the ALMS loop in the frequency domain and considers the performance bounds in both RF and digital domains.

Chapter 5 considers the impacts of I/Q imbalances occurred in the ALMS loop on its performance. An upper bound of the degradation factor is derived to estimate how much of compensation is required in other stages.

Chapter 6 proposes a beam-based analog SIC structure which employs the ALMS loops as adaptive filters. The development of the proposed structure is described from mathematical aspect to hardware implementation.

Chapter 7 focuses on the practical perspective of the ALMS loop by proposing an implementable structure using of-the-shelf components. It then describes the prototype and experiment results which verify all theoretical analyses.

Chapter 8 summarizes the major contributions of this research, and proposes future work plan.

CHAPTER 2

LITERATURE REVIEW

In this Chapter, some research works related to SI mitigation are firstly reviewed. Then, brief information about least mean square algorithm in digital adaptive filter is provided. Finally, a review on the operation and performance of the ALMS loop proposed in [9] is presented.

2.1 Self-Interference Mitigation

2.1.1 Propagation Domain Suppression

Propagation domain methods aim at reducing the level of SI at the input of the receive chain. These techniques can be further categorized into passive methods and active approaches [10], which are briefly described as follows.

Some typical passive propagation domain methods are presented in Fig. 2.1. It is seen that, in most of these techniques, multiple antennas are employed to reduce the coupling from the transmitter to the receiver. In Fig. 2.1(a), physical separation techniques locate transmit and receive antennas at a distance d to obtain a free space propagation loss [11, 12]. The relationship between d and the level of SI suppression for the carrier frequency of 2.45 GHz is illustrated in Fig. 2.2 [13]. Obviously, the longer d is, the higher attenuation will be achieved. Although this approach may not be suitable for compact size devices, its simplicity is very useful to quickly develop an IBFD front-end. Physical separation can be combined with spatial separation, demonstrated in Fig. 2.1(b)

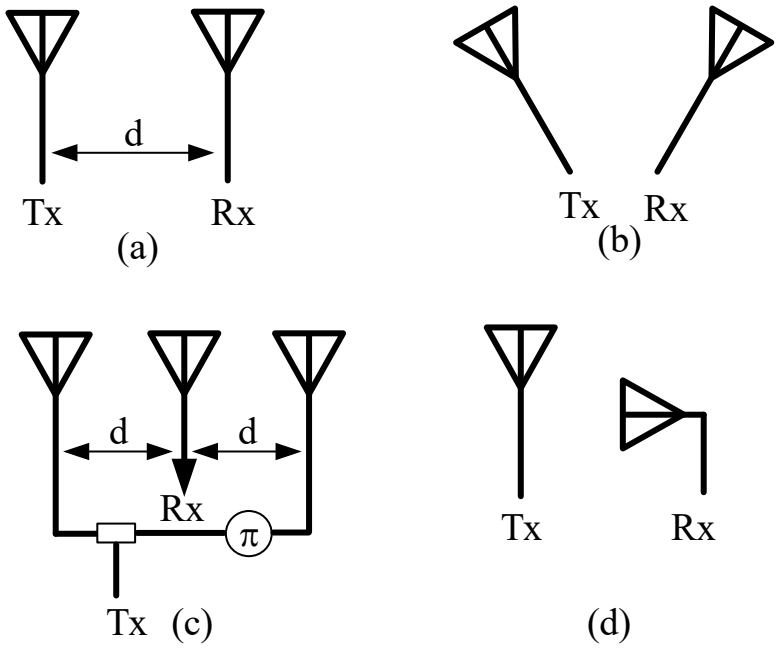

Figure 2.1: Propagation domain passive approaches: (a) Physical separation; (b) Spatial separation; (c) Antiphase control; (d) Cross-polarization.

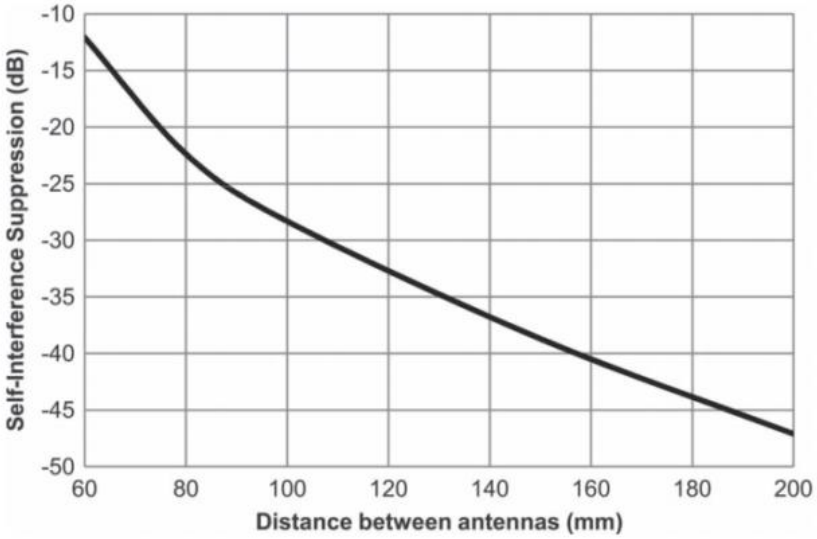

Figure 2.2: Amount of suppression by antenna separation at 2.45 GHz.

to increase the attenuation. In this case, directional antennas are employed and pointed to different directions to reduce their spatial beam overlap [14]. This method is suitable

for IBFD relay systems.

Figure 2.1 (c) is an example of passive phase control approaches which aim to create near-field nulls in the antenna radiation pattern. In this configuration, the transmitted signal and its 180 degree phase shifted version are respectively fed into two transmit antennas which are symmetrically located at a distance d from the receive antenna. Since the RF signals from the two transmitted antennas are out of phase and have the same amplitude, they cancel each other at the receive antenna. This method has been demonstrated for dipole [15], monopole [16] and patch [17] antennas. Since the antiphase transmitted signals are simultaneously emitted, this approach requires a careful system planning to avoid the far-field impact.

Cross-polarization methods shown in Fig. 2.1(d) isolate the transmitter and receiver by using cross-polarized antennas. Demonstrations of this method can be found in [18] with linear polarization and in [19, 20] with circular polarization. As pointed out in [10], the level of isolation achieved by this approach depends on manufacturing accuracy of antennas as well as the surrounding environment.

Active propagation domain methods require additional circuits or signal processing to mitigate the level of SI presented at the receiver. A popular approach in this category is using an impedance tuning circuit which includes a network of adjustable capacitors or varactors at the output of the receive antenna to terminate the SI from antenna to the ground [21, 22]. However, this technique can only mitigate the direct propagation path of the SI. For a complicated SI channel such as in IBFD MIMO systems, the impedance tuning circuit becomes less efficient.

Another active propagation domain method is beamforming in the transmitter to create a null at the location of receive antennas. Beamforming can be controlled by digital signal processing [23, 24] or by analog components in the RF front-end [25]. When beamforming is formed in the digital domain, it requires multiple transmit antennas. As for the case of analog, a combination of attenuators and phase shifters can control the transmit beam with just one antenna. In both cases, consideration on the far-field radiation is required to avoid the impact of this technique on the communication link.

2.1.2 Digital Self-Interference Cancellation

Digital cancellation is applied after ADC to mitigate the residual SI and recovered the signal of interest. These approaches can be classified into two categories including channel modeling and blind cancellation.

Channel modeling methods exploit the knowledge of the baseband interfering signal and use adaptive filtering techniques to generate the cancellation signal as shown in Fig. 2.3. Many different techniques have been proposed to estimate the SI channel response, the nonlinear components and noise caused by the analog devices in both transmit and receive chains. In particular, least square algorithm has been use to update the tap weight values in linear finite impulse response filters [26, 27]. For distortions caused by the power amplifier in the transmitter, Taylor series expansion has been used in [8, 28, 29] to approximate the non-linear functions. In addition, Hammerstein channel models which includes a nonlinear estimation filter and a linear one have been proposed in [30, 31] to possibly mitigate both the memory effects in the transmit channel and the non-linear distortion components of the PA. As pointed out in [32], these methods require high computational complexity to estimate the SI channel and nonlinear components. They are also sensitive to the statistic of the transmitted signal and surrounding environment.

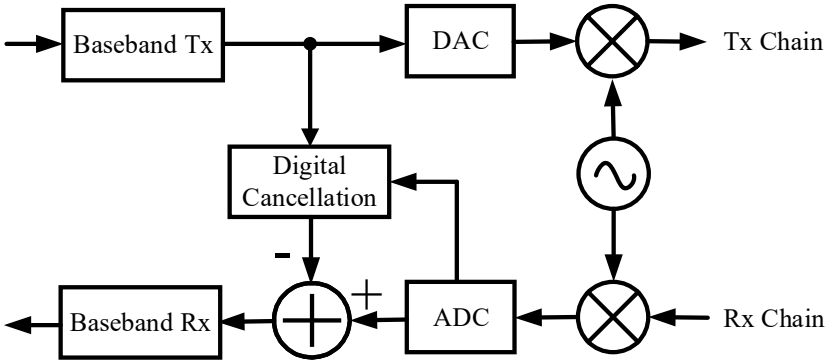

Figure 2.3: Digital cancellation using channel modelling methods

Blind cancellation methods do not require the channel state information. Instead, the mixing of the desired signal and residual SI is considered as a blind source separation problem. Since these signals are independent and non-Gaussian, independent component analysis algorithm can be applied to detect the signal of interest directly [33, 34]. Although this technique can reduce the computational complexity compared to estimation based one, it has to assume that the SI channel is static and requires a training period to search for the de-mixing matrix. Otherwise, an additional receiver chain is included into the transceiver for signal detection.

2.1.3 Radio Frequency Domain Cancellation

RF domain cancellation approaches strive to generate a signal that mimics SI in order to subtract it from the input of the receiver [35]. There are two main different ways to generate the cancellation signal. One is utilizing additional transmit chains to up-convert the calculated cancellation baseband signal as in Fig. 2.4(a). The other is employing a multi-tap adaptive filter to modify the amplitude and phase of the transmitted RF signal as in 2.4(b).

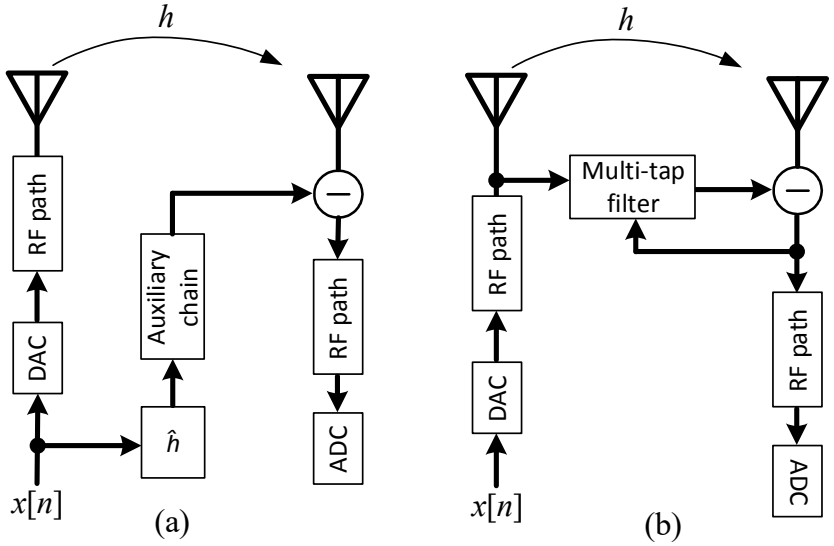

Figure 2.4: RF domain SIC approaches: (a) Additional transmit chain; (b) Multi-tap adaptive filter.

Auxiliary transmit chain or so-called digitally assisted approaches [10] utilize digital signal processing to estimate the SI channel $\hat{h}$ from the residual SI and the clean transmitted data $x(n), n = -\infty, \ldots, \infty$ to generate the baseband of the cancellation signal. Examples of this structure can be found in [12, 36, 37]. Since the modification of the cancellation signal is conducted in the baseband, this method can benefit from a digital adaptive filter, which is more flexible and can be implemented with higher number of taps than analog counterparts. However, an additional transmit chain not only consumes more energy and creates more noise, but more importantly, it has different properties of distortion and noise caused by analog components in the auxiliary RF chain compared to those in the original transmitted signal [38]. Thus, this problem becomes a bottleneck of this technique and the highest reported level of cancellation was only 30 dB [12].

On the other hand, multi-tap adaptive filter based techniques can potentially overcome the aforementioned bottleneck problem. As shown in Fig. 2.4(b), the RF transmitted

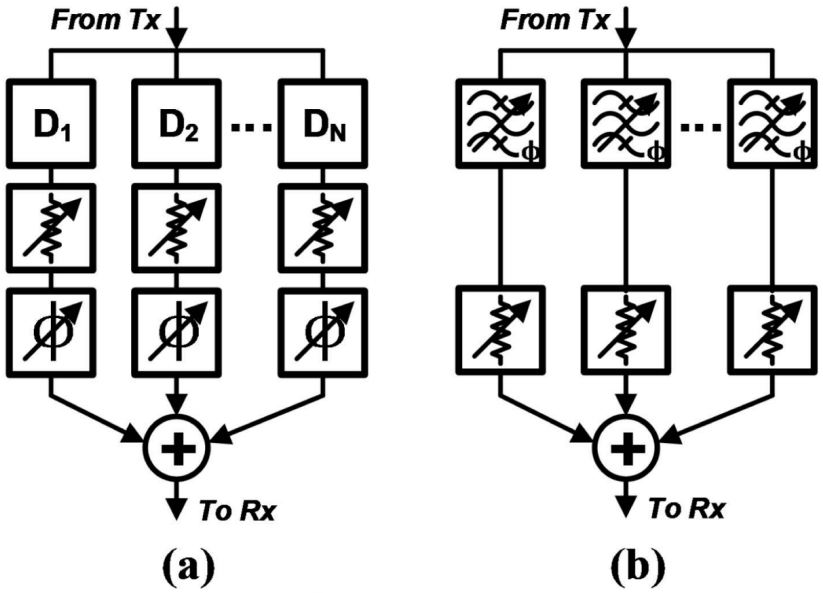

Figure 2.5: Multi-tap filter SIC techniques: (a) Time-domain approaches; (b) Frequency-domain approaches.

signal is employed as a reference at the input of the canceller so that the cancellation signal has the same distortion and noise properties as the SI. Generally, a multi-tap filter includes N branches, or so-called taps, to independently modify the amplitude and phase of the reference signal. Then, by combining the outputs of all the taps, the cancellation signal is obtained to cancel the SI at the input of the receiver.

Multi-tap cancellers can be implemented in the time-domain or in the frequency domain as shown in Fig. 2.5(a) and Fig. 2.5(b) [10], respectively. In the former case, each tap of these filters has a different time delay and a mechanism to modify the amplitude (e.g. attenuator) and phase (e.g. phase shifter) of the delayed reference signal. Examples of these filters can be found in [8, 38–40]. In the latter case, narrow-band band-pass filters (BPF), which have different center frequencies, are used to sample the reference signal in the frequency domain such as in [41–43]. One advantage of frequency-domain multi-tap filters is that they can avoid delay lines, which may be challenging if a very fine amount of delay is required in time-domain approaches. The reason is that a very fine delay is obtained by a microstrip trace or a coaxial cable, hence increasing the physical dimension of the time-domain based multi-tap filters. However, one problem with the frequency-domain based approaches is that, although BPF filters can be adjustable, they are normally static rather than adaptive as time-domain counterparts. Therefore, multi-tap adaptive filters are preferable for SIC in the RF stage.

In order to form an adaptive multi-tap filter, a closed-loop is necessary. As shown in Fig. 2.6, after cancellation, the residual signal is looped-back to the weights calculator block of the tap to synthesize the weighting coefficient $w(t)$, which will modify the phase and amplitude of the delayed signal. Since the residual SI is involved to the process of

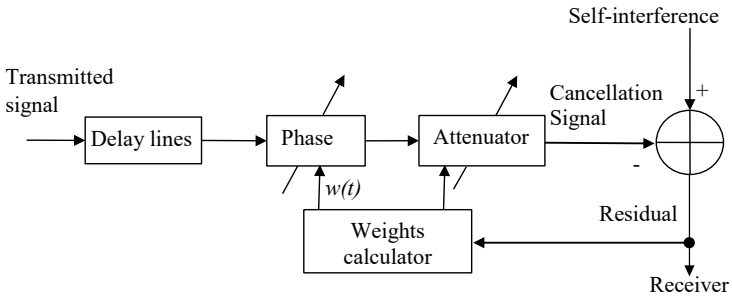

Figure 2.6: One tap of a closed-loop multi-tap filter.

finding weighting coefficients, the cancellation signal can properly mimic the practical impairments such as nonlinear components of the transmit power amplifier (PA) and the variation of the SI channel. Hence, the residual SI is minimized and the SI is canceled efficiently. The looped-back residual signal can be obtained in the RF domain as in [35, 38, 39, 44] or in the digital domain after the ADC as in [8, 45]. One problem with the digitalized looped-back signal is that in conventional receivers, an automatic gain controlled (AGC) amplifier is normally required to stabilize the level of the received signal which can be affected by multi-path fading. Consequently, the AGC amplifier will also stabilize the residual SI reducing the accuracy of the weighting coefficients obtained in this way.

The above analyses have shown that a time-domain multi-tap adaptive filter is a promising SIC scheme. It is also proved in [44] that this structure is suitable for wide-band applications. Next section reviews the problem of how to synthesize the optimized weighting coefficients to minimize the residual SI.

2.2 Least Mean Square Algorithm

Adaptive filters have been widely used for various applications such as noise cancellation, channel equalization, and modelling systems where filters' parameters need to be adapted to estimate time-varying signals. Among many different methods to adjust filter's coefficients, the least mean square (LMS) algorithm proposed by Widrow and Hoff

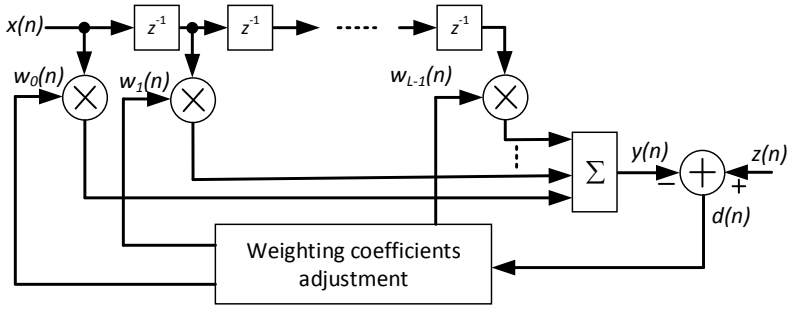

Figure 2.7: L-tap transversal adaptive filter structure.

in 1960 is the most popular one due to its simplicity and robustness to signal statistic [46]. A general structure of a digital transversal finite impulse response adaptive filter is shown in Fig. 2.7 [47]. The adaptive filter including L taps whose weighting coefficients $w_l(n), l = 0,\ldots,L-1$, can be adjusted to generate the output $y(n)$ from the input $x(n)$ as

$$y(n) = \sum_{l=0}^{L-1} w_l(n)x(n-l). \tag{2.1}$$

The weighting coefficients are adjusted so that $y(n)$ efficiently mimics $z(n)$. It means that the mean square error, defined as $\zeta = E\{d^2(n)\} = E\{[z(n)-y(n)]^2\}$ where $E\{.\}$ is expectation operation, is minimized.

The LMS algorithm is an alternative computational method to determine the optimum $w_l(n), l = 0,\ldots,L-1$ by replacing the statistic expectation operation by its instantaneous estimated value $\hat{\zeta} = d^2(n)$. Then, instead of solving a set of linear equations yielded by differentiating ζ with respect to $w_l(n), l = 0,\ldots,L-1$ to find the optimized weighting coefficients, the LMS algorithm is a recursive gradient method to update the filter coefficients as

$$\mathbf{w}(n+1) = \mathbf{w}(n) - \mu\nabla d^2(n) \tag{2.2}$$

where $\mathbf{w}(n) = [w_0(n)\ w_1(n)\cdots\ w_{L-1}(n)]^T$, μ is the algorithm step size parameter and $\nabla = \left[\frac{\partial}{\partial w_0}\frac{\partial}{\partial w_1}\cdots\frac{\partial}{\partial w_{L-1}}\right]^T$ is a column vector of the gradient operator. From $\nabla d^2(n) = -2d(n)\mathbf{x}(n)$ where $\mathbf{x}(n) = [x(n)\ x(n-1)\cdots\ x(n-L+1)]$, we get the LMS recursion as

$$\mathbf{w}(n+1) = \mathbf{w}(n) + 2\mu d(n)\mathbf{x}(n). \tag{2.3}$$

From (2.3), we can see that LMS algorithm is very simple to implement in the digital domain. Therefore, many RF domain SIC multi-tap adaptive filters such as [11, 38, 40, 44] require an additional down-converter and ADC to digitalize the RF

residual signal. Then, the LMS algorithm is applied to update the weighting coefficients. However, this additional receiver chain leads to more hardware complexity and produces more noise for the receiver.

Widrow et. al proved that the LMS algorithm can also be applied for continuous signal [48] by converting (2.2) into an integration operation. The updating equation for the tap weight coefficient $w_l(t)$ can be expressed as

$$w_l(t) = -2\mu \int_0^t \nabla_{w_l} d^2(\tau) d\tau. \tag{2.4}$$

From (2.4), the structure of an L-taps continuous-time LMS adaptive filter is presented in Fig. 2.8 [49]. In this structure, an ideal integrator is required to update the weighting

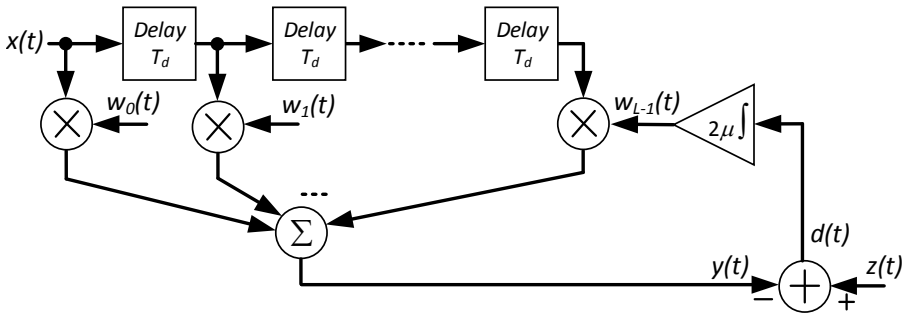

Figure 2.8: L-tap transversal continuous-time adaptive filter structure.

coefficient for each tap. Due to ideal integrators are only available at low frequency, continuous-time LMS adaptive filters have been used in wired digital communications such as voice-band modem [50, 51] and asymmetric digital subscriber lines (ADSL) [52]. To applied in the RF domain SIC, a mixer is used to down-convert the RF residual SI before implementing a continuous-time adaptive filter [39].

2.3 Analog Least Mean Square Loop

The unavailability of RF integrators makes the implementation of continuous-time LMS adaptive filters being complicated. To overcome this problem, a more practical analog LMS algorithm has been proposed in [9] by replacing (2.4) with the following equation

$$\frac{w_l(t)}{dt} + \alpha w_l(t) = -\frac{\mu\alpha}{K_1 K_2} \frac{\partial d^2(t)}{\partial w_l(t)},\ l = 0,\ldots,L-1 \tag{2.5}$$

where μ, α, K_1, and K_2 are constant parameters defining the convergence of the filter. Since (2.5) represents a low-pass filter with the impulse response $\alpha e^{-\alpha t}$ for $t > 0$ and the

input signal $-\left(\frac{\mu\alpha}{K_1K_2}\frac{\partial d^2(t)}{\partial w_l(t)}\right)$, the analog LMS (ALMS) adaptive filter can be implemented purely in the RF domain without ideal integrators and DSP. The weighting coefficient is expressed by convolving the filter impulse response with the input signal as

$$w_l(t) = -\frac{\mu\alpha}{K_1K_2}\int_0^t e^{-\alpha(t-\tau)}\frac{\partial d^2(\tau)}{\partial w_l(\tau)}d\tau. \tag{2.6}$$

Since $z(t)$ is independent to $w_l(t), l = 0,\ldots,L-1$, $\frac{\partial d^2(t)}{\partial w_l(t)} = -2d(t)\frac{\partial y(t)}{\partial w_l(t)}$. Assuming the ALMS filter is implemented in an IBFD system with transmitted signal $x(t)$= Re$\{X(t)e^{j2\pi f_c t}\}$ where $X(t)$ and f_c are the baseband equivalent and the carrier frequency, we have

$$\frac{\partial d^2(t)}{\partial w_l(t)} = -2d(t)X(t-lT_d)e^{j2\pi f_c(t-lT_d)}. \tag{2.7}$$

Therefore, the weighting coefficient of the proposed ALMS algorithm is obtained by

$$w_l(t) = \frac{2\mu\alpha}{K_1K_2}\int_0^t e^{-\alpha(t-\tau)}d(\tau)X(\tau-lT_d)e^{j2\pi f_c(\tau-lT_d)}d\tau. \tag{2.8}$$

Based on (2.8), the ALMS loop was proposed in [9] as shown in Fig. 2.9.

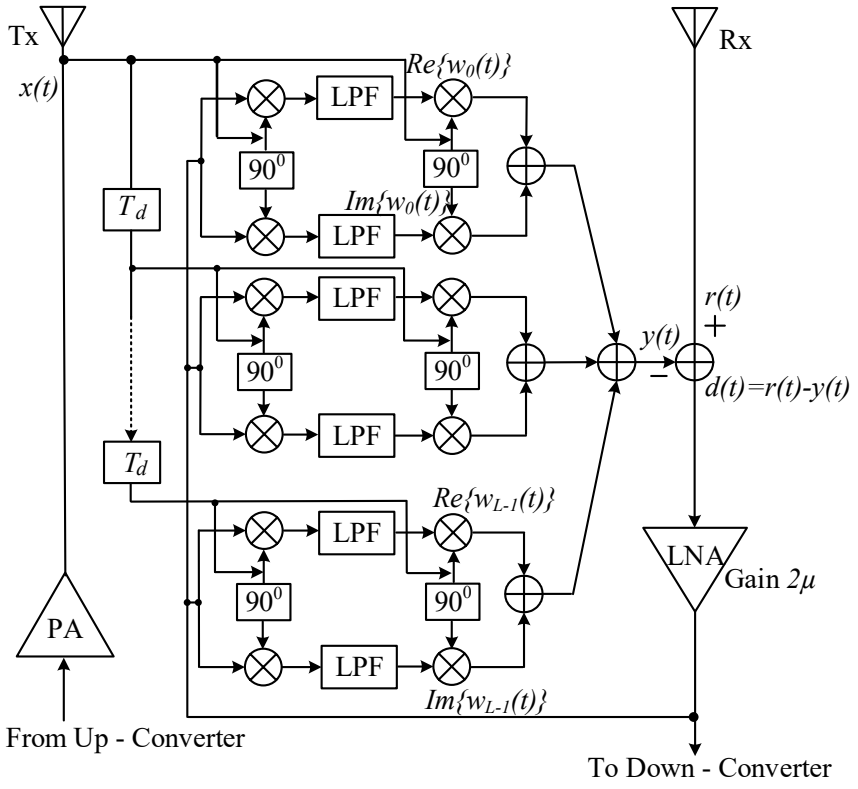

Figure 2.9: ALMS loop structure.

In this structure, the residual signal is amplified by an LNA with 2μ gain and then looped-back to the input of all the taps. An in-phase/quadrature (I/Q) demodulator is employed at each tap to multiply the looped-back signal with the delayed reference signal which acts as $\partial d^2(t)/\partial w_l(t)$. The multipliers in two branches of the demodulator have the same dimensional constant K_1. The outputs of the LPFs will be $w_l(t)K_2$ where K_2 is the dimensional constant of the multipliers, which are also assumed to be the same in the modulator. Here, the dimensional constant of a multiplier K is defined by the ratio of the product of input voltages over the output voltage, i.e., $K = V_{in1}V_{in2}/V_{out}$. Therefore, in overall, the output of the adaptive filter will be scaled by $1/K_1K_2$. From this structure, the cancellation signal is represented by

$$y(t) = \mathrm{Re}\Big\{\sum_{l=0}^{L-1} w_l^*(t)X(t-lT_d)e^{j2\pi f_c(t-lT_d)}\Big\}. \tag{2.9}$$

Due to the IBFD operation, at the input of the receiver, there appears the SI $z(t)$, the signal of interest $s(t)$, and noise $n(t)$, i.e., $r(t) = z(t)+s(t)+n(t) = \mathrm{Re}\Big\{[Z(t)+S(t)+N(t)]e^{j2\pi f_c t}\Big\}$ where $Z(t), S(t), N(t)$ are the low-pass equivalent of those signals, respectively. The SI channel is modelled as an L-tap delay line filter, i.e.,

$$z(t) = \mathrm{Re}\Big\{\sum_{l=0}^{L-1} h_l^* X(t-lT_d)e^{j2\pi f_c t}\Big\} \tag{2.10}$$

where $h_l, l = 0,\ldots,L-1$ are the tap coefficients. From (2.9) and (2.10), the residual SI signal, denoted $v(t)$, can be expressed as

$$v(t) = \mathrm{Re}\Big\{\sum_{l=0}^{L-1} [h_l - w_l(t)e^{j2\pi f_c lT_d}]X(t-lT_d)e^{j2\pi f_c t}\Big\}. \tag{2.11}$$

Defining the weighting error function $u_l(t)= h_l - w_l(t)e^{j2\pi f_c lT_d}$ as the difference between the channel coefficient and weighting coefficient of the l-th tap of the adaptive filter, $u_l(t)$ represents the performance of the ALMS loop. The weighting error function has been comprehensively investigated in [9] under both micro and macro scales.

Fig. 2.10 summarizes the earlier results on the ALMS loop presented in [9]. After proposing the ALMS loop structure and describing its operation, the impact of the transmitted signal has been considered for a single-carrier system. It has shown that due to the cyclostationary property of the transmitted signal, the weighting error function will not converge to a stable value, but it always varies in a range. Hence, this variation leads to an irreducible interference. The convergence behavior of the ALMS loop is also proved to be jointly determined by the decay constant α of the LPF and the loop gain

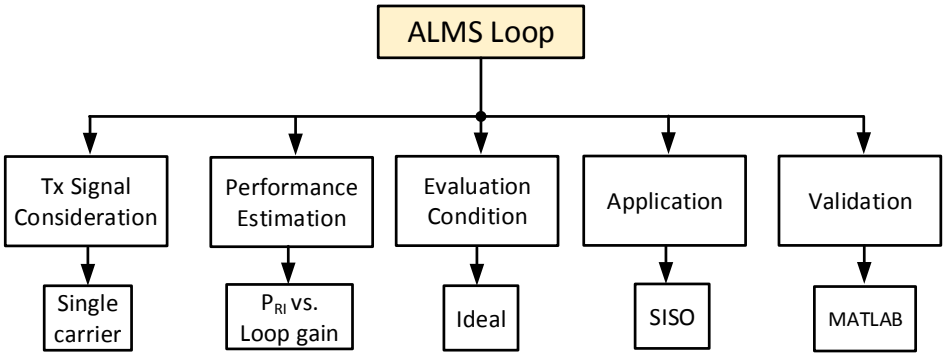

Figure 2.10: Earlier research on ALMS loop.

$\mu V_X^2/K_1K_2$ where V_X is the mean square amplitude of the baseband transmitted signal. Then, by using stationary analysis, the residual SI has been derived and the level of cancellation under a given SI channel has been determined. However, these analyses are conducted under ideal condition of the ALMS loop. The problem of I/Q imbalances which may occur in the I/Q demodulators and modulators has not been evaluated. In addition, the application of the ALMS loop is only shown with the single input single output (SISO) system only. Finally, the analyses are all confirmed by simulation in MATLAB.

CHAPTER 3

ALMS LOOP WITH DIFFERENT SIGNAL PROPERTIES

It has been shown in [9] that properties of the transmitted signals have a significant impact on the performance of the ALMS loop. The analyses in [9] were conducted for the single-carrier system only. Therefore, to adopt the ALMS loop to other IBFD systems, the behaviors of the ALMS loop with different transmitted signals are evaluated. Particularly, the ALMS loop performance with multi-carrier signalling in an OFDM system is firstly investigated using both cyclostationary and stationary analyses. Secondly, the performance of the ALMS loop with OFDM signal is compared to that with single-carrier signal. Finally, the ALMS loop is studied with deterministic chirp signal for its potential applications in full-duplex synthetic aperture radar (SAR) systems.

3.1 ALMS Loop for OFDM Systems

3.1.1 OFDM System Model

In an OFDM system, the transmitted signal $x(t)$ is defined as

$$x(t) = \mathrm{Re}\{X_o(t)e^{j2\pi f_c t}\} \tag{3.1}$$

where $X_o(t)$ is the complex envelope of the OFDM signal with a cyclic prefix and f_c is the carrier frequency. $X_o(t)$ is represented by

$$X_o(t) = \sum_{n=-\infty}^{\infty} \sum_{m=-\infty}^{\infty} \sum_{k=-N_{st}/2, k\neq 0}^{N_{st}/2} a_{k,m} e^{j2\pi \frac{k}{N}(n-m\frac{T_o}{T_s})} w(n-m\frac{T_o}{T_s}) p(t-nT_s) \tag{3.2}$$

where k is the k-th sub-carrier; m is the m-th OFDM symbol; n is the sample index; t is continuous time; T_s is the sampling period of the baseband signal; T_o is the OFDM symbol period; N_{st} is the total number of data subcarriers; N is the number of samples in one OFDM symbol excluding cyclic prefix; $w(n)$ is the windowing function; and $p(t)$ is the pulse shaping function. The root mean square amplitude of the transmitted signal is defined as $V_X = \sqrt{\frac{1}{T_o}\int_0^{T_o} E\{|X(t)|^2\}dt}$, where $E\{.\}$ stands for expectation. The load is normalized to 1Ω so that the average power of $X_o(t)$ is V_X^2. The complex data symbols $a_{k,m}$ are assumed to be independent to each other such that the ensemble expectation

$$E\{a_{k,m}^* a_{k',m'}\} = \begin{cases} 1, & \text{for } k = k', m = m' \\ 0, & \text{for } k \neq k', m \neq m'. \end{cases} \tag{3.3}$$

3.1.2 Cyclostationary Analysis

Cyclostationary analysis is applied to evaluate the performance of the ALMS loop under the impact of several factors including the properties of the transmitted signal, loop gain, and the parameter of the LPF. This analysis is important to derive the lower bound of the irreducible interference given by the ALMS loop and digital cancellation.

3.1.2.1 Autocorrelation Function

The autocorrelation function of an OFDM signal is defined as $\Phi_o(t,\tau) = E\{X_o^*(t)X_o(t-\tau)\}$. Let $l = n - mT_o/T_s$ in (3.2) and define $g(t,\tau) = \sum_{m=-\infty}^{\infty} p^*(t-mT_o)p(t-mT_o-\tau)$. Using the property expressed in (3.3), the autocorrelation function can be expressed as

$$\Phi_o(t,\tau) = \sum_{l=-\infty}^{\infty}\sum_{l'=-\infty}^{\infty}\sum_{k=-N_{st}/2,k\neq 0}^{N_{st}/2} e^{-j2\pi\frac{k}{N}(l'-l)} \times w(l)w(l')g(t-lT_s,(l^{'}-l)T_s+\tau). \tag{3.4}$$

When $p(t)$ is a Raised Cosine pulse shaping function with roll-off factor 0.25, $g(t)$ is shown in Fig. 3.1. It can be seen that $g(t,\tau) \approx 0$ when τ is any integer multiple of T_s. Therefore, the autocorrelation function at $\tau = 0$ can be approximated as $\Phi_o(t,0) = N_{st}\sum_{l=-\infty}^{\infty} w^2(l)g(t-lT_s,0)$. For simplicity, the convolution of $w^2(l)$ with $g(t,0)$ can be further approximated as a periodic function with a continuous window in one period, i.e., $\Phi_o(t,0) \approx V_X^2\sum_{l=-\infty}^{\infty} w^2(t-lT_o)$ where $w(t), 0 \leq t \leq T_o$ is the normalized windowing function such that $\frac{1}{T_o}\int_0^{T_o} w^2(t)dt = 1$.

3.1.2.2 Solution for Weighting Error Function

The interference channel is modeled as a multi-tap filter so that the equivalent baseband $Z(t)$ of the SI can be expressed as $Z(t) = \sum_{l=0}^{L-1} h_l^* X_o(t-lT_s)$ where L is the number of

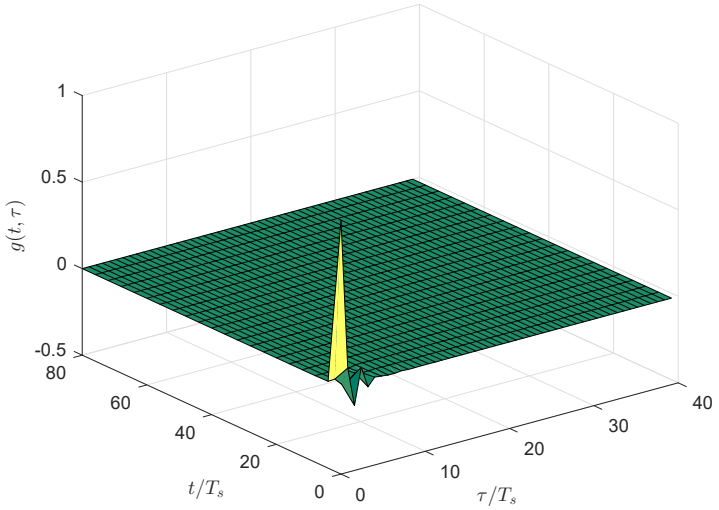

Figure 3.1: $g(t,\tau)$ with $T_o = 80T_s$ and pulse shaping roll-off factor 0.25.

taps, and tap delay is equal to the sampling period T_s for simplicity. The performance of ALMS loop therefore can be represented by the error $u_l(t)$ between the l-th tap coefficient of interference channel model and the corresponding weight of the adaptive filter. The expected value of $u_l(t)$ is derived in [9] as $\bar{u}_l(t) = h_l - \frac{\mu\alpha V_X^2}{K_1 K_2}\int_0^t e^{-\alpha(t-\tau)}\bar{u}_l(\tau)\tilde{\Phi}_o(\tau,0)d\tau$ where $\tilde{\Phi}_o(\tau,0) = \frac{1}{V_X^2}\Phi_o(t,0)$ is the normalized autocorrelation function. Solving this equation, the final expression of $\bar{u}_l(t)$ is obtained as

$$\bar{u}_l(t) = h_l\left[\frac{1+\mu A^2 e^{-\alpha(1+\mu A^2)t}}{1+\mu A^2}\right]e^{-\alpha\mu A^2\int_0^t(\tilde{\Phi}_o(\tau,0)-1)d\tau} \tag{3.5}$$

where $A = V_X/\sqrt{K_1 K_2}$. Applying the windowing function recommended in IEEE802.11a [53], which is converted to the continuous function and normalized as

$$w(t) = \sqrt{\frac{4(1+\beta_o)}{4-\beta_o}}\begin{cases} sin^2(\frac{\pi}{2}(\frac{t}{T_1})) & 0 \le t < T_1 \\ 1 & T_1 \le t < T_2 \\ sin^2(\frac{\pi}{2}(\frac{T_o-t}{T_1})) & T_2 \le m < T_o \end{cases} \tag{3.6}$$

where $T_1 = \beta T_o/(1+\beta_o)$ and $T_2 = T_o/(1+\beta_o)$ with β_o as the roll-off factor of the windowing function, we have

$$\bar{u}_l(t) = h_l\frac{1+\mu A^2 e^{-\alpha(1+\mu A^2)t}}{1+\mu A^2}e^{-\alpha\mu A^2 q(t)} \tag{3.7}$$

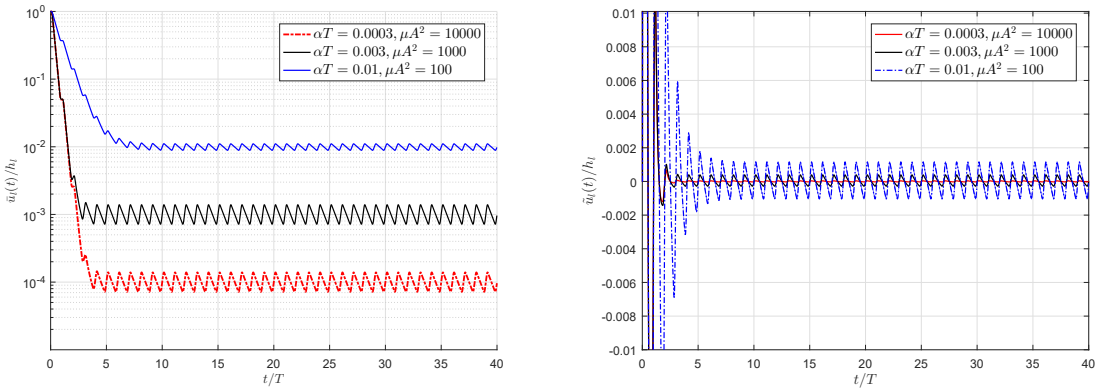

(a) (b)

Figure 3.2: (a) Normalized weight error; and (b) Normalized weight error variation.

with $q(t)$ in period $[0, T_o]$ derived as

$$q(t) = \begin{cases} \frac{5(\beta_o-1)}{2(4-\beta_o)}t - \frac{2\beta_o T_o}{(4-\beta_o)\pi} sin(\frac{\pi t}{T_1}) + \\ \frac{\beta_o T_o}{4\pi(4-\beta_o)} sin(\frac{2\pi t}{T_1}) & 0 \le t < T_1 \\ \frac{5\beta_o}{4-\beta_o}(t - T_o/2) & T_1 \le t < T_2 \\ \frac{5(\beta_o-1)}{2(4-\beta_o)}(t-T_o) + \frac{2\beta_o T}{(4-\beta_o)\pi} sin(\frac{\pi(T_o-t)}{T_1}) - \\ \frac{\beta T_o}{4\pi(4-\beta_o)} sin(\frac{2\pi(T_o-t)}{T_1}) & T_2 \le t < T_o. \end{cases} \tag{3.8}$$

Since $q(t)$ is a periodic function with the period of T_o, the error function $\bar{u}_l(t)$ has cyclostationary property, i.e., it does not converge to a stable value but varies accordingly. The normalized $\bar{u}_l(t)$ and its variation with the error without cyclostationary behavior $\tilde{u}_l(t)$ are presented in Fig. 3.2(a) and Fig. 3.2(b) respectively.

Discussion

1. When applied to a multi-carrier system, the ALMS loop behaves similarly as in a single-carrier counterpart. The weight error function $\bar{u}_l(t)$ and $\tilde{u}_l(t)$ are both periodic of OFDM symbol period T_o and respectively converge to $h_l \frac{1}{1+\mu A^2} e^{-\mu A^2 \alpha q(t)}$ and $h_l \frac{1}{1+\mu A^2}(e^{-\mu A^2 \alpha q(t)} - 1)$ when $t \to \infty$. The convergence speed is driven by the loop gain μA^2 and the LPF parameter α.

2. The residual interference power and interference suppression ratio (ISR) can be calculated as in [9] $P_{RI} = \frac{1}{1+\mu A^2} \frac{A^2}{2} \sum_{l=0}^{L-1} |h_l|^2$ and $ISR = \frac{P_{RI}}{P_I} = \frac{1}{(1+\mu A^2)^2}$ respectively.

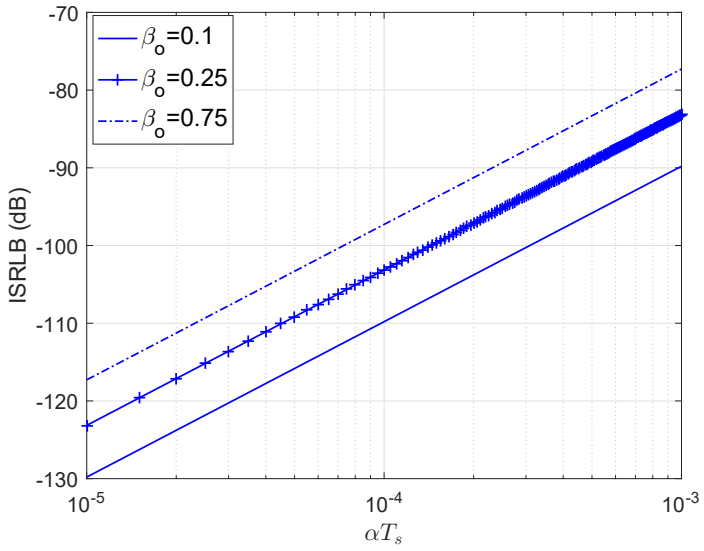

Figure 3.3: ISRLB versus αT_s with various windowing roll-off factors β_o.

3. The irreducible interference power is calculated by

$$\begin{aligned} P_{II} &= P_I \frac{1}{T_o}\int_0^{T_o}\left[\frac{1}{1+\mu A^2}(e^{-\alpha\mu A^2 q(t)}-1)\right]^2 dt \\ &\approx P_I \frac{1}{T_o}\int_0^{T_o}[\alpha q(t)]^2 dt. \end{aligned} \tag{3.9}$$

Therefore, irreducible ISR lower bound is

$$ISRLB = \frac{P_{II}}{P_I} = \frac{\alpha^2 T_o^2 \beta^2}{(4-\beta_o)^2(1+\beta_o)^2}\left\{\frac{25}{12}(1-\beta_o)^2 + \frac{5\beta_o}{16\pi^2}(81-55\beta_o)\right\}. \tag{3.10}$$

From (3.10), it can be seen that the ISRLB of an OFDM system is determined by the LPF constant α and the roll-off factor β_o of the windowing function. This relationship is presented in Fig. 3.3.

Fig. 3.3 shows that the windowing function plays an important role in the performance of ALMS filter. The ISRLB becomes smaller if the windowing function has closer form of the rectangular one.

From the ISRLB expression, the LPF parameter can be determined in order that the ISRLB is much smaller than ISR. In this case, stationary analysis can be applied to evaluate the behavior of the ALMS loop. Under this macro-scale analysis, the weight error function and interference residual power are solved with non-ideal signal autocorrelation, fractionally-spaced taps ALMS filter and general interference channel. Since

the transmitted signal is treated as a stationary process, both ensemble expectation and time average is applied to the autocorrelation function of the OFDM signal. It means that the solutions for the time and ensemble averaged weight function $\bar{\bar{w}}(t)$ and the residual interference power P_{RI} are not different from those of a single-carrier case. Therefore, the results derived in [9] can be applied for this case. Specifically, the matrix of weight function $\bar{\bar{\mathbf{w}}}(t) = [\bar{\bar{w}}_0(t)\ \bar{\bar{w}}_1(t)..\ \bar{\bar{w}}_{L-1}(t)]^T$ is found as

$$\bar{\bar{\mathbf{w}}}(t) = \text{diag}\left\{e^{-j2\pi f_c T_d l}\right\}\mathbf{Q}\,\text{diag}\left\{\frac{\mu\lambda_l}{1+\mu\lambda_l}(1-e^{-(1+\mu\lambda_l)\alpha t}\right\}\mathbf{Q}^{-1}\mathbf{h} \tag{3.11}$$

and the $P_{RI}(t)$ is calculated by

$$P_{RI}(t) = \frac{1}{2}\epsilon^2 + \frac{1}{2}\mathbf{h}^H\mathbf{Q}\,\text{diag}\left\{\frac{\lambda_l}{(1+\mu\lambda_l)^2}\right\}\mathbf{Q}^{-1}\mathbf{h} \tag{3.12}$$

where ϵ is the error between the real SI $Z(t)$ and the modeled one; $\mathbf{h}$ is the one-column matrix of the modeled tap coefficients $\mathbf{h} = [h_0\ h_1\ ...\ h_{L-1}]^T$; $\mathbf{Q}$ and λ_l are the orthonormal modal matrix and the eigenvalues of the normalized autocorrelation matrix $\mathbf{\Phi}$ with each element defined by

$$\bar{\Phi}_o(\tau) = \frac{1}{K_1K_2T_o}\int_0^{T_o}\Phi_o(t,\tau)dt. \tag{3.13}$$

It is shown in [9] that the ISR can be calculated from $P_{RI}(t)$ and $P_I(t)$ as

$$ISR = \frac{\epsilon^2 + \mathbf{h}^H\mathbf{Q}\,\text{diag}\left\{\frac{\lambda_l}{(1+\mu\lambda_l)^2}\right\}\mathbf{Q}^{-1}\mathbf{h}}{\epsilon^2 + \mathbf{h}^H\mathbf{\Phi}\mathbf{h}} \tag{3.14}$$

Using these formulas, the weight error functions, the normalized residual interference power, and ISR can be determined.

3.1.3 Simulation Results

The simulation is performed with an OFDM system specified in the IEEE802.11 standard. Transmitted data is generated with sampling period of $T_s = 5\ ns$ and modulated using BPSK before going through a 64-point IFFT block. Cyclic prefix is then added which occupies one fourth of an OFDM symbol. The IEEE 802.11 windowing function and the RC pulse shaping function are utilized with the roll-off factors $\beta_o = 0.25$. The power of the transmitted signal is set at 0 dBm, and the multiplier dimensional constants are set to be $K_1K_2 = 0.001V^2$ so that $A = 10$. Another loop gain parameter μ is selected as $\mu = 10$. α is determined using the expression of $ISRLB = 10^{-10}$. Simulations are conducted under two scenarios of interference channel which are set as the same as in [9]. Specifically, the first scenario assumes that the reflected paths of the interference

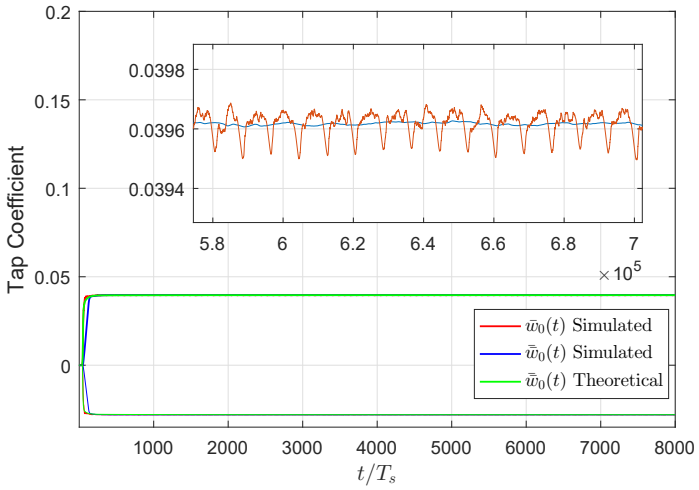

Figure 3.4: Simulated and theoretical weighting coefficients of ALMS loop with T_s spacing.

channel have the delays of multiple T_s so that the interference channel is chosen as $h(t) = 10^{\frac{-25}{20}}\{[\frac{\sqrt{2}}{2} - 0.5j]\delta(t) - 0.4\delta(t - T_s) + 0.3\delta(t - 3T_s)\}$. The second scenario considers the general case of interference channel where the reflected paths have arbitrary delays, i.e., $h(t) = 10^{\frac{-25}{20}}\{[\frac{\sqrt{2}}{2} - 0.5j]\delta(t) - 0.4\delta(t - 0.9T_s) + 0.3\delta(t - 3.3T_s)\}$. The performance of the ALMS loop filter with 8 taps spaced at T_s and 16 taps spaced at $T_s/2$ are also investigated.

The convergence curves of the first tap coefficients $\bar{w}_0(t)$ under the first scenario with T_s spaced is presented in Fig. 3.4. At macro scale, the simulated weights coefficients converge to almost the same values calculated from (3.11). At micro scale shown in the inset, the simulated $\bar{w}_0(t)$ varies with the period of OFDM symbol T_o. This figure shows both cyclostationary effect and the expectation in stationary analysis for the weighting error function. The convergence curves of the residual interference power for two cases of tap spacing in the first interference channel scenario are presented in Fig. 3.5. It is seen that the simulated curves in both cases coincide with the theoretical ones calculated from (3.12). The SI is canceled at a higher level when T_s spacing is utilized. The reason is that modeling error for T_s spacing is zero whereas it is 7.508×10^{-11} for the $T_s/2$ case.

3.2 Single-Carrier and Multi-Carrier IBFD Systems

As can be seen from Section 3.1, the key to analyze the performance of the ALMS loop is the weighting error function which can be derived from an integral equation. In

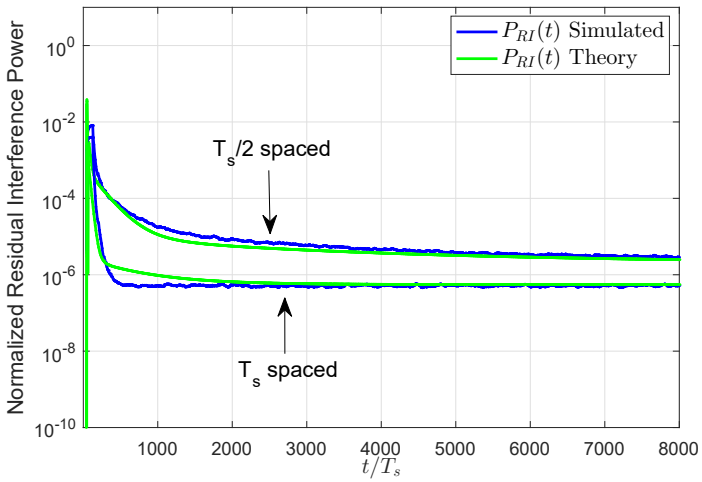

Figure 3.5: Simulated and theoretical convergence curves for residual interference power of the ALMS loop with T_s and $T_s/2$ spacing in the first scenario.

this Section, the solution of the weighting error function is extended in a general case. This general solution can be applied to investigate the performance of the ALMS loop employed in any IBFD system. It is revealed that, due to the cyclostationary effects of the transmitted signal, the weighting error function cannot converge to a stable value, but it varies periodically. Consequently, there always exists an irreducible SI whose power depends on the variation of the weighting error function. The solution is then applied to compare the performance of the ALMS loop in a single-carrier system to that in a multi-carrier such as an orthogonal frequency division multiplexing (OFDM) system. It is shown that the convergence speed of the weighting error function is the same in both cases and depends on the loop gain. However, the weighting error function in the single-carrier system has a smaller variation than that in the OFDM case. The irreducible interference suppression ratio lower bounds (ISRLB) are also derived for the two systems respectively. Comparison between them shows that more SI cancellation can be ultimately achieved for the single-carrier system.

3.2.1 Signal Models

Consider an IBFD system including a baseband part which can operate in either single-carrier or OFDM mode and an RF part employing an ALMS loop. The transmitted RF signal is expressed as $x(t) = Re\{X(t)e^{2\pi f_c t}\}$ where f_c is the carrier frequency, and $X(t)$ is the baseband equivalent which is further denoted as $X_s(t)$ in the single-carrier mode and

$X_o(t)$ in the OFDM mode. Mathematically, $X_s(t)$ and $X_o(t)$ can be expressed as

$$X_s(t) = \sum_{i=-\infty}^{\infty} a_i p(t - iT_s) \tag{3.15}$$

and

$$X_o(t) = \sum_{n=-\infty}^{\infty} \sum_{m=-\infty}^{\infty} \sum_{k=-N_{st}/2, k\neq 0}^{N_{st}/2} a_{k,m} e^{j2\pi \frac{k}{N}(n - m\frac{T_o}{T_s})} \cdot w\left[n - m\frac{T_o}{T_s}\right] p(t - nT_s) \tag{3.16}$$

respectively, where a_i, and $a_{k,m}$ are the i-th data symbol in the single-carrier system and the data symbol on the k-th sub-carrier of the m-th OFDM symbol respectively; T_s is the symbol period of the single-carrier system and also the sample period of the OFDM system; T_o is the OFDM symbol period; N_{st} is the total number of data sub-carriers; N is the number of samples in one OFDM symbol excluding cyclic prefix; $w[n]$ is the discrete windowing function applied to an OFDM symbol; and $p(t)$ is the pulse shaping function. The root mean square amplitude of the transmitted signal is defined as $V_X = \sqrt{\frac{1}{T}\int_0^T E\{|X(t)|^2\}dt}$, where $E\{.\}$ stands for expectation; T is the period of transmitted data symbol, i.e., T_s or T_o. The complex data symbols a_i and $a_{k,m}$ are assumed to be independent to each other in single-carrier and OFDM systems respectively. The autocorrelation function of the transmitted baseband signal $X(t)$ is defined as $\Phi(t,\tau) = E\{X^*(t)X(t-\tau)\}$. With the symbol independence assumption, the autocorrelation functions of single-carrier and OFDM signals can be derived as

$$\Phi_s(t,\tau) = \sum_{i=-\infty}^{\infty} p^*(t - iT_s)p(t - \tau - iT_s) \tag{3.17}$$

and

$$\Phi_o(t,\tau) = \sum_{l=-\infty}^{\infty} \sum_{l'=-\infty}^{\infty} \sum_{k=-N_{st}/2, k\neq 0}^{N_{st}/2} e^{-j2\pi \frac{k}{N}(l'-l)} \cdot w[l]w[l']g(t - lT_s, (l^{'} - l)T_s + \tau) \tag{3.18}$$

respectively, where $g(t,\tau) = \sum_{m=-\infty}^{\infty} p^*(t - mT_o)p(t - mT_o - \tau)$. It is seen that $\Phi_s(t,\tau) = \Phi_s(t + T_s, \tau)$ and $\Phi_o(t,\tau) = \Phi_o(t + T_o, \tau)$ for all t and τ. Therefore, both transmitted signals $X_s(t)$ and $X_o(t)$ can be treated as wide-sense cyclostationary processes.

As presented in [9], the performance of the ALMS loop can be determined by the weighting error function $u_l(t) = h_l - w_l(t)e^{j2\pi f_c l T_d}$ whose expected value $\bar{u}_l(t)$ can be derived as

$$\bar{u}_l(t) = h_l - \frac{\mu\alpha}{K_1K_2}\int_0^t e^{-\alpha(t-\tau)} \sum_{l'=0}^{L-1} \bar{u}_{l'}(\tau)\Phi(\tau, (l-l')T_d)d\tau. \tag{3.19}$$

This equation shows that the weighting error function not only depends on the loop parameters α, μ and K_1K_2 but also relates to the autocorrelation function of the transmitted

signal, and thus the cyclostationary properties will have significant impact on the ALMS loop performance.

3.2.2 General Solution of Weighting Error Function

It is very difficult to solve (3.19) in a general case. However, if the autocorrelation function of the transmitted signal satisfies that

$$\Phi(t,\tau) = \begin{cases} V_X^2\tilde{\Phi}(t,0), & \text{for } \tau = 0 \\ 0 & \text{for } \tau = \text{integer multiples of } T_d \end{cases} \tag{3.20}$$

where $\tilde{\Phi}(t,0)$ is the normalized autocorrelation function, (3.19) can be simplified as

$$\bar{u}_l(t) = h_l - \alpha\mu A^2 \int_0^t e^{-\alpha(t-\tau)}\bar{u}_l(\tau)\tilde{\Phi}(\tau,0)d\tau \tag{3.21}$$

where $A^2 = V_X^2/K1K2$. Taking the differentiation with respect to t on both sides of ((3.21)), we have

$$\begin{aligned} \frac{d\bar{u}_l(t)}{dt} &= \mu A^2\alpha^2 \int_0^t e^{-\alpha(t-\tau)}\bar{u}_l(\tau)\tilde{\Phi}(\tau,0)d\tau - \mu\alpha A^2\bar{u}_l(t)\tilde{\Phi}(t,0) \\ &= \alpha\Big[h_l - \bar{u}_l(t)\Big] - \mu\alpha A^2\bar{u}_l(t)\tilde{\Phi}(t,0) \end{aligned} \tag{3.22}$$

which can be further rearranged in the form of the ordinary differential equation (ODE), i.e.,

$$\frac{d\bar{u}_l(t)}{dt} + \alpha\Big[1 + \mu A^2\tilde{\Phi}(t,0)\Big]\bar{u}_l(t) = \alpha h_l. \tag{3.23}$$

The solution for the homogeneous form of the ODE, i.e., $U'(t) + \alpha\Big[1 + \mu A^2\tilde{\Phi}(t,0)\Big]U(t) = 0$ can be found by rearranging it as

$$\frac{U'(t)}{U(t)} = -\alpha\Big[1 + \mu A^2\tilde{\Phi}(t,0)\Big]. \tag{3.24}$$

Integrating both sides from 0 to t, we get $\ln U(t) = -\alpha\int_0^t \Big[1 + \mu A^2\tilde{\Phi}(\tau,0)\Big]d\tau + \ln U(0)$ so that

$$U(t) = U(0)e^{-\alpha\int_0^t \Big[1+\mu A^2\tilde{\Phi}(\tau,0)\Big]d\tau}. \tag{3.25}$$

Replacing $U(0)$ by a function $f(t)$, $\bar{u}_l(t) = f(t)e^{-\alpha\int_0^t \left[1+\mu A^2\tilde{\Phi}(\tau,0)\right]d\tau}$ is the solution for the non-homogeneous form of the ODE. Taking the differentiation of $\bar{u}_l(t)$ and substituting it into (3.23) we get $f'(t) = \alpha h_l e^{-\alpha\int_0^t \left[1+\mu A^2\tilde{\Phi}(\tau,0)\right]d\tau}$. Therefore,

$$f(t) = \alpha h_l \int_0^t e^{\alpha\int_0^\tau \left[1+\mu A^2\tilde{\Phi}(v,0)\right]dv}d\tau + C$$

where C is any constant. The solution for $\bar{u}_l(t)$ is thus

$$\begin{aligned}\bar{u}_l(t) &= \left[\alpha h_l \int_0^t e^{\alpha\int_0^\tau \left[1+\mu A^2\tilde{\Phi}(v,0)\right]dv} d\tau + C\right] e^{-\alpha\int_0^t \left[1+\mu A^2\tilde{\Phi}(\tau,0)\right]d\tau} \\ &= \left[\alpha h_l \int_0^t e^{-\alpha(1+\mu A^2)(t-\tau)} e^{\alpha\mu A^2\int_0^\tau \left[\tilde{\Phi}(v,0)-1\right]dv} d\tau + Ce^{-\alpha(1+\mu A^2)t}\right] e^{-\alpha\mu A^2\int_0^t \left[\tilde{\Phi}(\tau,0)-1\right]d\tau}.\end{aligned} \tag{3.26}$$

When $\alpha\mu A^2\int_0^\tau[\tilde{\Phi}(v,0)-1]dv \ll 1$ and $t \gg 1/\alpha(1+\mu A^2)$,

$$\int_0^t e^{-\alpha(1+\mu A^2)(t-\tau)} e^{\alpha\mu A^2\int_0^\tau \left[\tilde{\Phi}(v,0)-1\right]dv} d\tau \approx \frac{1}{\alpha(1+\mu A^2)}. \tag{3.27}$$

Therefore, $\bar{u}_l(t) \approx \left[\frac{h_l}{1+\mu A^2} + Ce^{-(1+\mu A^2)t}\right] e^{-\mu A^2\alpha\int_0^t \left[\tilde{\Phi}(\tau,0)-1\right]d\tau}$. From the initial condition that $\bar{u}_l(0) = h_l$ we have $C = h_l\frac{\mu A^2}{1+\mu A^2}$, and hence the final solution is

$$\bar{u}_l(t) = \left[h_l \frac{1+\mu A^2 e^{-\alpha(1+\mu A^2)t}}{1+\mu A^2}\right] e^{-\mu A^2\alpha q(t)} \tag{3.28}$$

where $q(t) = \int_0^t \left[\tilde{\Phi}(\tau,0)-1\right]d\tau$.

Due to the cyclostationary properties of $\tilde{\Phi}(\tau,0)$, we see that $e^{-\mu\alpha A^2 q(t)}$ is a periodic function so that $\bar{u}_l(t)$ varies periodically. If there was no cyclostationary effect, the weighting error function, denoted as $\breve{u}_l(t)$, would have the expectation $E\{\breve{u}_l(t)\} = h_l\frac{1+\mu A^2 e^{-\alpha(1+\mu A^2)t}}{1+\mu A^2}$, which would converge to a stable value $h_l\frac{1}{1+\mu A^2}$ when $t \gg 1/\alpha(1+\mu A^2)$. In this case the residual SI could be further removed in the digital domain. However, the presence of cyclostationary effect in the residual SI makes it impossible to be completely removed in digital domain. Thus there always exists an irreducible interference whose power P_{II} is determined by the variation between $u_l(t)$ and $\breve{u}_l(t)$. The expected value of this variation is denoted as $\tilde{u}_l(t) = E\{u_l(t)-\breve{u}_l(t)\} = h_l\frac{1}{1+\mu A^2}(e^{-\mu A^2\alpha q(t)}-1)$ when $t \gg 1/\alpha(1+\mu A^2)$. Since $E\{|X|^2\} \geq |E\{X\}|^2$ for any random process X, the time averaged P_{II} is

$$\begin{aligned}P_{II} &= \frac{A^2}{2}\sum_{l=0}^{L-1}\frac{1}{T}\int_0^T E\left\{\left|u_l(t)-\breve{u}_l(t)\right|^2\right\}dt \\ &\geq \frac{A^2}{2}\sum_{l=0}^{L-1}\frac{1}{T}\int_0^T \left|E\left\{u_l(t)-\breve{u}_l(t)\right\}\right|^2 dt = \frac{A^2}{2}\sum_{l=0}^{L-1}\frac{1}{T}\int_0^T |\tilde{u}(t)|^2 dt \\ &= P_I\frac{1}{T}\int_0^T \left[\frac{1}{1+\mu A^2}(e^{-\alpha\mu A^2 q(t)}-1)\right]^2 dt \approx P_I\frac{1}{T}\int_0^T [\alpha q(t)]^2 dt\end{aligned} \tag{3.29}$$

where $P_I = \frac{A^2}{2}\sum_{l=0}^{L-1}|h_l|^2$ is the normalized interference power. Based on the lower bound of P_{II}, the irreducible interference suppression lower bound (ISRLB) defined as

$$ISRLB = \frac{P_I\frac{1}{T}\int_0^T[\alpha q(t)]^2 dt}{P_I} = \frac{1}{T}\int_0^T [\alpha q(t)]^2 dt \tag{3.30}$$

can be used as a measure to compare the performance of the ALMS loop for different types of the transmitted signal. Therefore, ISRLB is an important figure to be considered in the cancellation design process. In the following section, we compare the performance of the ALMS loop in a single-carrier system with that in a multi-carrier one to show the impact of cyclostationary properties.

3.2.2.1 Single-Carrier Versus OFDM

To apply the above solution of the weighting error function of the ALMS loop to the two systems, their respective autocorrelation functions are firstly examined. For a single-carrier system with RRC pulse shaping function, it is shown in [9] that $\Phi_s(t,\tau)$ satisfies (3.20) with a closed-form as

$$\Phi_s(t,\tau) \approx \begin{cases} V_X^2\left(\frac{2\beta_s}{\pi} cos\frac{2\pi t}{T_s} + 1\right), & \text{for } \tau = 0 \\ 0, & \text{for } \tau = \text{integer multiples of } T_s \end{cases} \tag{3.31}$$

where β_s is the roll-off factor of the RRC pulse shaping function. Hence, $q(t)$ for the single-carrier system is derived as $q_s(t) = T_s\frac{\beta_s}{\pi^2} sin\frac{2\pi t}{Ts}$ [9, Eq.(17)]. In case of the multi-carrier system, an IEEE802.11a baseband is taken as an example. As proved in Section 3.1.2, the autocorrelation function of the OFDM signal has a closed form of a periodic function of t whose period contains the continuous window $w^2(t)$, i.e.,

$$\Phi_o(t,(l-l')T_d) \approx \begin{cases} V_X^2 \sum_{m=-\infty}^{\infty} w^2(t-mT_o), & \text{for } l = l' \\ 0, & \text{for } l \neq l' \end{cases} \tag{3.32}$$

where $w(t)$, $0 \le t \le T_o$, is the normalized continuous windowing function, such that $\frac{1}{T_o}\int_0^{T_o} w^2(t)dt = 1$. It means that $\Phi_o(t,\tau)$ satisfies the condition (3.20). For the discrete windowing function recommended in the IEEE802.11a standard [53], using the autocorrelation function of the OFDM signal in Section 3.1.2, we have

$$q_o(t) = \begin{cases} \frac{5(\beta_o-1)}{2(4-\beta_o)}t - \frac{2\beta_o T_o}{(4-\beta_o)\pi} sin(\frac{\pi t}{T_1}) + & \\ \frac{\beta_o T_o}{4\pi(4-\beta_o)} sin(\frac{2\pi t}{T_1}) & 0 \le t < T_1 \\ \frac{5\beta_o}{4-\beta_o}(t - T_o/2) & T_1 \le t < T_2 \\ \frac{5(\beta_o-1)}{2(4-\beta_o)}(t-T_o) + \frac{2\beta_o T_o}{(4-\beta_o)\pi} sin(\frac{\pi(T_o-t)}{T_1}) & \\ -\frac{\beta_o T_o}{4\pi(4-\beta_o)} sin(\frac{2\pi(T_o-t)}{T_1}) & T_2 \le t < T_o. \end{cases} \tag{3.33}$$

From $q_s(t)$, $q_o(t)$, and (3.28) we can obtain the weighting error functions for the single-carrier and OFDM systems as $\bar{u}_{l,s}(t)$ and $\bar{u}_{l,o}(t)$, respectively. To compare the performance

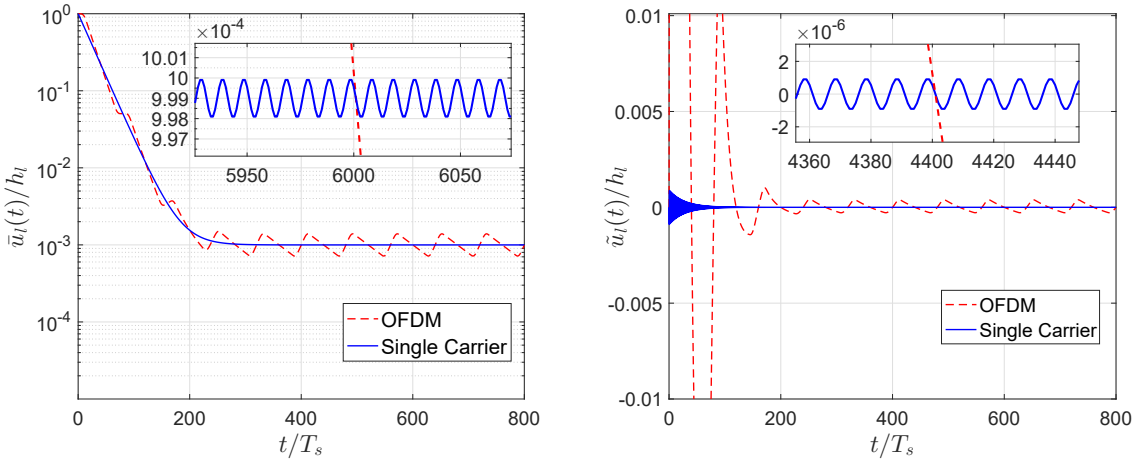

(a) (b)

Figure 3.6: (a) Normalized weight error; and (b) Normalized weight error variation with the loop gain $\mu A^2 = 1000$, $\alpha T_s = 0.003$, $T_o = 80T_s$, and $\beta_s = \beta_o = 0.25$.

of the ALMS loop in the two systems, the convergence curve of the normalized weighting error function $\bar{u}_l(t)/h_l$ for the two cases under loop gain $\mu A^2 = 1000$, $\alpha T_s = 0.003$ and $T_o = 80T_s$ are plotted in Fig. 3.6(a). The normalized variation $\tilde{u}_l(t)/h_l$ is presented in Fig. 3.6(b). The insets in Fig. 3.6 show a closer look for the $\bar{u}_{l,s}(t)$ and $\tilde{u}_{l,s}(t)$, respectively.

From Fig. 3.6, it can be concluded that with the same loop gain μA^2 and the RC constant α, the convergence speeds of $\bar{u}_{l,s}(t)$ and $\bar{u}_{l,o}(t)$ are the same for both cases of the transmitted signals. Moreover, both $\bar{u}_{l,s}(t)$ and $\bar{u}_{l,o}(t)$ do not converge to a stable value, but they vary with periods T_s and T_o, respectively. In terms of variation, as shown in Fig. 3.6(a), $\tilde{u}_{l,s}(t)$ varies in a smaller range than $\tilde{u}_{l,o}(t)$ does. Thus, the ISRLB of the single-carrier system is expected to be smaller than that of the OFDM counterpart. Substituting $q_s(t)$ and $q_o(t)$ into (3.15), we obtain the ISRLB for the single-carrier and OFDM systems as $ISRLB_s = \frac{1}{2}\left(\alpha T_s \frac{\beta_s}{\pi^2}\right)^2$, and $ISRLB_o = \frac{\alpha^2 T_o^2 \beta_o^2}{(4-\beta_o)^2(1+\beta_o)^2}\left\{\frac{25}{12}(1-\beta_o)^2 + \frac{5\beta_o}{16\pi^2}(81-55\beta_o)\right\}$, respectively. Putting the $ISRLB_s$ and $ISRLB_o$ together in Fig. 3.7 as functions of αT_s and various values of the roll-off factors β_s, β_o, we see that, with the same value of β_s and β_o except for $\beta_s = 0$ and $\beta_o = 0$, $ISRLB_s$ is much smaller than $ISRLB_o$. It means that when the ALMS loop has exactly the same tap spacing as the SI channel, the SI in the single-carrier system can be suppressed to a much lower level than that in the ODFM system. The reason is that the weighting coefficients of the ALMS loop are affected by the autocorrelation function of the transmitted signal as analyzed. As the period of an OFDM symbol is much longer than that of a data symbol in the single-carrier

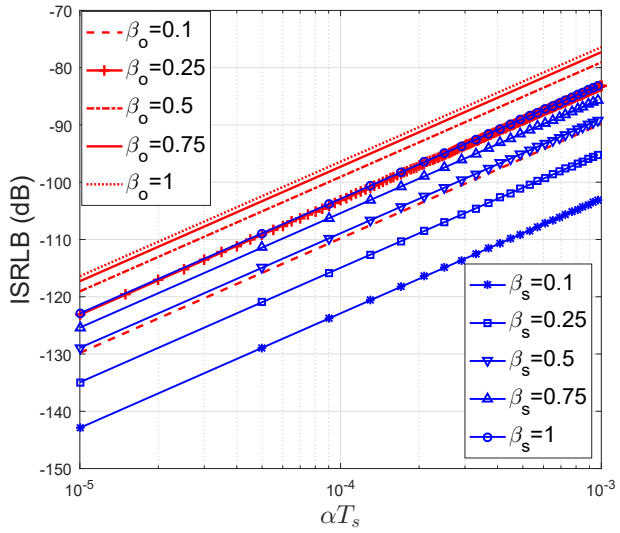

Figure 3.7: ISRLB of the two systems with various values of β_s and β_o.

system, the weight coefficients in the OFDM system vary more significantly.

3.2.3 Conclusion

The general solution for the weighting error function is derived to reveal the significant impacts of cyclostationary properties of the transmitted signal on the performance of the ALMS loop. Applying this solution to both single-carrier and OFDM IBFD systems, it is shown that, given the same loop gain and other parameters, the SI can be potentially canceled more effectively to a smaller level of ISRLB in the single-carrier system than that in the OFDM system due to the different cyclostationary properties of the transmitted signals. Determining the ISRLB is an important consideration in the SIC design process.

3.3 ALMS Loop with Deterministic Signal in FD SAR

3.3.1 Introduction

The combination of a full-duplex (FD) radio technique and continuous wave (CW) radar, called generalized continuous wave synthetic aperture radar (GCW-SAR), has been developed recently [54]. With GCW-SAR, the slow time sampling in azimuth direction used in conventional pulsed SAR and frequency modulated (FM) CW SAR systems is

no longer required and thus some intrinsic limitations, such as the minimum antenna area constraint [55], can be removed. This new SAR concept enables the development of future high resolution and wide swath remote sensing technologies. However, due to the simultaneous transmitting and receiving operations, GCW-SAR also faces a severe problem of SI. Therefore, SIC is a key issue to be addressed for realization of GCW-SAR.

The requirement of SIC for wireless FD systems can be achieved by three levels of cancellation at propagation (or antenna), RF front-end, and digital domains [4]. However, there are two main differences between SIC in GCW-SAR systems and that in FD communication systems. Firstly, in a GCW-SAR system, a chirp signal is periodically transmitted rather than a random signal as in the communication counterpart. As a result, the behaviors of the cancellation circuits in GCW-SAR systems such as the convergence and stabilization properties may be affected. Secondly, in the GCW-SAR systems, digital domain cancellation may not be required as the residual SI does not need to be lower than the noise floor level as in the FD communication system. The reason is that the received signals in GCW-SAR can be considered as time delayed transmitted signals. The useful received signals are the far-field reflections, whereas the SI can be regarded as near field reflections which can be easily removed after image compression. Therefore, for GCW-SAR, the antenna and RF domain SIC will be of a significant importance since SIC is required to protect the ADC from being saturated by the strong SI. As an example, a GCW-SAR system can have a similar configuration as in a practical airborne FMCW-SAR system [56]. The transmit power is 18 dBm, and the receiver noise floor is at -90 dBm. If the ADC in the receiver has the dynamic range of 60 dB, and the signal-to-interference ratio required for a normal FD operation is -45 dB, the level of residual SI must be less than -90 - (-45) = -45 dBm. The SIC required can be calculated by 18 - (-45) = 63 dB. Hence, about 70 dB of SIC must be achieved before digitalized by the ADC.

Such 70 dB of SIC can be achieved by two steps of SIC in the propagation domain and the RF domain. In the first step, the transmit and receive antennas are separated with a distance to attenuate the level of SI as in [57]. For example, with the operating frequency at 5 GHz, at least 25 dB of SI attenuation can be achieved when the transmit and receive antennas are located at a distance of 100 mm or higher. The rest of the required SIC can be obtained in the second step by employing the ALMS loop in the RF domain.

As proved in [9, 58, 59], the transmitted signal properties have a noticeable impact on the performance of the ALMS loop. However, the analyses in these publications are only conducted for the random signals in IBFD communication systems. Therefore, two

questions that could be raised are *whether the ALMS loop works with deterministic signals, like in a GCW-SAR system, and if yes, how well it performs in this case*.

To answer these questions, the performance of the ALMS loop in a GCW-SAR system is evaluated with chirp signaling. A stationary analysis is applied to investigate the average convergence behavior of the loop by deriving the ensemble and time averaged weighting error function of the loop, which is the solution of an integral equation. It is proved that the ALMS loop can also work with the chirp signal in the GCW-SAR by a proper selection of the tap delay and number of taps in the loop. In particular, the tap delay of the loop must be selected according to the bandwidth of the chirp signal to avoid spectral overlapping. The number of taps in the loop is also constrained so that only one period of the autocorrelation function of the chirp signal is involved in the solution of the weighting error function. Simulation results show that about 45 dB SI suppression can be achieved with the ALMS loop under the selected simulation parameters. Combined with antenna separation, the total SI suppression requirement can be satisfied for a practical GCW-SAR system. Hence, the contributions of this Section are twofold. Firstly, it shows that the ALMS loop can work with both deterministic and random signals. Secondly, it proves that 70 dB of SIC can be obtained by using antenna separation and the ALMS loop in the RF domain with the given parameters. This level of SIC provides a reference for future researches on GCW-SAR.

3.3.2 GCW-SAR Signal Model

Considering a GCW-SAR system, which employs the ALMS loop in the RF front-end as in Fig. 2.9, the transmitted signal $x(t)$ is defined as

$$x(t) = \mathrm{Re}\{X(t)e^{j2\pi f_c t}\} \tag{3.34}$$

where $X(t)$ is the low-pass equivalent of the transmitted signal and f_c is the carrier frequency. In a conventional pulsed SAR system, a chirp signal pulse $P(t)$ is transmitted, and $P(t)$ can be expressed as

$$P(t) = \mathrm{rect}(\frac{t}{T})e^{j\pi k_r t^2} \tag{3.35}$$

where T is the pulse duration and k_r is the chirp rate. However, in the GCW-SAR, the chirp signal $P(t)$ is transmitted periodically with the period of T, hence $X(t)$ is represented by $X(t) = \sum_{l=-\infty}^{\infty} V_X P(t - lT)$ where V_X is the root mean square amplitude of the transmitted chirp signal, and it can be calculated by $V_X = \sqrt{\frac{1}{T}\int_0^T |X(t)|^2 dt}$. The

load is normalized to 1 Ω so that the average power of $X(t)$ is V_X^2. At the input of the receiver, the received signal $r(t)$ is a combination of the SI $z(t)$, the reflected signal $s(t)$ from the target and the additive Gaussian noise $n(t)$, i.e.,

$$r(t) = z(t) + s(t) + n(t). \tag{3.36}$$

The low-pass equivalents of these signals are denoted as $Z(t)$, $S(t)$, $N(t)$, respectively. The reflected signal $S(t)$ is a sum of a number of transmitted signals with different delays and attenuations, so that it can be modeled as

$$S(t) = \int \sigma(\tau) X(t-\tau) d\tau \tag{3.37}$$

where $\sigma(t)$ represents the reflection coefficients which are related to the radar cross sections of the surveyed area and their associated phases at the receiver antenna.

The GCW-SAR system is equipped with separated transmit and receive antennas, and they are located at a distance of 100 mm. Hence, at least 25 dB of SI attenuation can be achieved by the propagation loss [57]. In order to cancel the remaining SI, the ALMS loop is employed. The structure of the ALMS loop in GCW-SAR systems is still the same as that in IBFD communication systems. The weighting coefficient $w_l(t)$ of the l-th tap is also obtained by

$$w_l(t) = \frac{2\mu\alpha}{K_1 K_2} \int_0^t e^{-\alpha(t-\tau)} [r(\tau) - y(\tau)] X(\tau - lT_d) e^{j2\pi f_c(\tau - lT_d)} d\tau. \tag{3.38}$$

The cancellation signal $y(t)$ at the output of the ALMS loop is represented by

$$y(t) = \mathrm{Re}\Big\{ \sum_{l=0}^{L-1} w_l^* X(t - lT_d) e^{j2\pi f_c(t - lT_d)} \Big\}. \tag{3.39}$$

The SI channel is modeled as a multi-tap filter so that the equivalent baseband version $Z(t)$ of the SI can be presented as $Z(t) = \sum_{l=0}^{L-1} h_l^* X(t - lT_d)$ where L is the number of taps, and the tap delay of the SI channel is assumed to be equal to that in the ALMS loop for convenience at the moment. More general modeling of the SI channel will be discussed later in Section 3.3.4.

The weighting error function which shows the performance of the ALMS loop is written as

$$u_l(t) = h_l - \frac{\mu\alpha}{K_1 K_2} \int_0^t e^{-\alpha(t-\tau)} \Big[\sum_{l'=0}^{L-1} u_{l'}(\tau) X^*(\tau - l'T_d) + S^*(\tau) + N^*(\tau) \Big] X(\tau - lT_d) d\tau. \tag{3.40}$$

3.3.3 Stationary Analysis

A stationary analysis is applied to evaluate the performance of the ALMS loop for the GCW-SAR system. This requires that both ensemble expectation and time averaging should be considered to derive the convergence behavior of the loop.

3.3.3.1 Weighting Error Function

Taking ensemble expectation of the above equation and assuming that the reflection coefficients are random and very small so that the ensemble expectation $E\{S^*(\tau)X(\tau - lT_d)\}$ is negligible in comparison with $E\{Z^*(\tau)X(\tau - lT_d)\}$, we have

$$\bar{u}_l(t) = h_l - \frac{\mu\alpha}{K_1K_2}\int_0^t e^{-\alpha(t-\tau)}\sum_{l'=0}^{L-1}\bar{u}_{l'}(\tau)X^*(\tau - l'T_d)X(\tau - lT_d)d\tau, \tag{3.41}$$

where $\bar{u}_l(t) = E\{u_l(t)\}$. Eq. (3.38) implies that the ALMS loop starts at $t = 0$. In general, the ALMS loop can start at any time instant t_0, thus (3.41) can be re-written as

$$\bar{u}_l(t+t_0) = h_l - \frac{\mu\alpha}{K_1K_2}\int_{t_0}^{t+t_0} e^{-\alpha(t+t_0-\tau)}\sum_{l'=0}^{L-1}\bar{u}_{l'}(\tau)X^*(\tau - l'T_d)X(\tau - lT_d)d\tau. \tag{3.42}$$

Defining $\tau' = \tau - t_0$, we have

$$\bar{u}_l(t+t_0) = h_l - \frac{\mu\alpha}{K_1K_2}\int_0^t e^{-\alpha(t-\tau')}\sum_{l'=0}^{L-1}\bar{u}_{l'}(\tau'+t_0)X^*(\tau'+t_0 - l'T_d)X(\tau'+t_0 - lT_d)d\tau'. \tag{3.43}$$

Taking time average over one period T of $\bar{u}_l(t+t_0)$ with respect to the starting time t_0, we obtain the ensemble and time averaged weighting error function $\bar{\bar{u}}_l(t)$ defined as

$$\begin{aligned}\bar{\bar{u}}_l(t) &= \frac{1}{T}\int_0^T \bar{u}_l(t+t_0)dt_0 \\ &= h_l - \frac{\mu\alpha}{K_1K_2T}\int_0^T\int_0^t e^{-\alpha(t-\tau')}\sum_{l'=0}^{L-1}\bar{u}_{l'}(\tau'+t_0)X^*(\tau'+t_0 - l'T_d)X(\tau'+t_0 - lT_d)d\tau'dt_0.\end{aligned} \tag{3.44}$$

Since α is very small, $\bar{u}_l(t)$ changes slowly and it can be seen as a constant in one period of T, i.e., $\bar{u}_l(t+t_0) \approx \bar{\bar{u}}_l(t)$, thus (3.44) can be written as

$$\begin{aligned}\bar{\bar{u}}_l(t) &= h_l - \mu\alpha\int_0^t e^{-\alpha(t-\tau')}\Big[\sum_{l'=0}^{L-1}\bar{\bar{u}}_{l'}(\tau')\frac{1}{K_1K_2T}\int_0^T X^*(\tau'+t_0 - l'T_d)X(\tau'+t_0 - lT_d)dt_0\Big]d\tau' \\ &= h_l - \mu\alpha\int_0^t e^{-\alpha(t-\tau')}\sum_{l'=0}^{L-1}\bar{\bar{u}}_l(\tau')\Phi((l-l')T_d)d\tau'\end{aligned} \tag{3.45}$$

where $\Phi((l-l')T_d)$ is the normalized autocorrelation function of the transmitted signal defined by

$$\Phi(\tau) = \frac{1}{K_1 K_2 T} \int_0^T X^*(t) X(t-\tau) dt. \tag{3.46}$$

To solve (3.45), we need to find the closed-form equation of the normalized autocorrelation function.

3.3.3.2 Autocorrelation Function of Transmitted Signal

Since $X(t)$ is a periodic function with the period T, $\Phi(\tau)$ is also periodic with the period T. Hence, the autocorrelation function can be expressed as $\Phi(\tau) = \sum_{l=-\infty}^{\infty} A^2 \Phi_P(\tau + lT)$ where $A^2 = V_X^2/K_1K_2$ and $\Phi_P(\tau)$ is the autocorrelation function of $P(t)$ defined as:

$$\begin{aligned}
\Phi_P(\tau) &= \frac{1}{T}\int_0^T P^*(t)P(t-\tau)d\tau \\
&= \frac{1}{T}\int_0^T \text{rect}(\frac{t}{T})\text{rect}(\frac{t-\tau}{T}) e^{-j\pi k_r t^2} e^{j\pi k_r (t-\tau)^2} dt \\
&= \frac{1}{T}\int_0^T \text{rect}(\frac{t}{T})\text{rect}(\frac{t-\tau}{T}) e^{j\pi k_r (-2t\tau+\tau^2)} dt.
\end{aligned} \tag{3.47}$$

Obviously, $\Phi_P(\tau) = 0$ if $\tau < -T$ and $\tau > T$. For $0 \le \tau \le T$, $\Phi_P(\tau)$ is found as

$$\Phi_P(\tau) = \frac{T-|\tau|}{T}\text{sinc}(\pi k_r \tau (T-|\tau|)). \tag{3.48}$$

$\Phi_P(\tau)$ is plotted in Fig. 3.8.

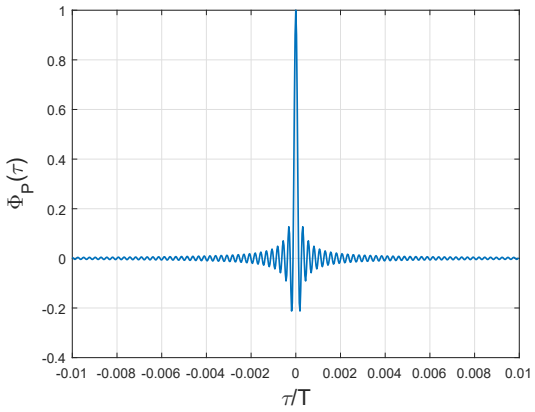

Figure 3.8: The autocorrelation function of $P(t)$ with chirp rate $k_r = 2.5 \times 10^{12}$.

3.3.3.3 Solution of Weighting Error Function

From $\Phi(\tau)$, (3.45) can be solved using the matrix form as in [9, pp. 7-8].

$$\bar{\tilde{\mathbf{u}}}(t) = \mathbf{h} - \mu\alpha \int_0^t e^{-\alpha(t-\tau)} \mathbf{\Phi} \bar{\tilde{\mathbf{u}}}(\tau) d\tau \tag{3.49}$$

where $\bar{\tilde{\mathbf{u}}}(t) = [\bar{\tilde{u}}_0(t)\ \bar{\tilde{u}}_1(t)\ \cdots \bar{\tilde{u}}_{L-1}(t)]^H$, $\mathbf{h} = [h_0\ h_1\ \cdots\ h_{L-1}]^H$, and

$$\mathbf{\Phi} = \begin{bmatrix} \Phi(0) & \Phi(-T_d) & \cdots & \Phi(-(L-1)T_d) \\ \Phi(T_d) & \Phi(0) & \cdots & \Phi(-(L-2)T_d) \\ \vdots & \vdots & \ddots & \vdots \\ \Phi((L-1)T_d) & \Phi((L-2)T_d) & \cdots & \Phi(0) \end{bmatrix}.$$

It can be seen from the matrix $\mathbf{\Phi}$ that, each row of $\mathbf{\Phi}$ consists of L samples of $\Phi(\tau)$ with sampling rate of $1/T_d$. From the Nyquist theorem, in order to avoid spectral overlapping, it is required that $1/T_d \geq 2\frac{B}{2}$, where $B/2$ is the maximum frequency of the chirp signal with the bandwidth B ($B = k_r T$). Therefore, the tap delay of the ALMS loop must be selected as $T_d = \frac{1}{nB}$ where n is integer, and $n \geq 1$. In addition, the number of taps L also has to be limited so that $(L-1)T_d \leq T$. This condition ensures that only one period of $\Phi(\tau)$ is involved in deriving $\bar{\tilde{\boldsymbol{u}}}(t)$. From these conditions, the solution for the weighting error functions derived in [9] can be applied to the chirp signal. In particular, the matrix $\mathbf{\Phi}$ is decomposed as $\mathbf{\Phi} = \mathbf{Q}\mathbf{\Lambda}\mathbf{Q}^{-1}$ where $\mathbf{Q}$ is the orthonormal modal matrix whose columns are the L eigenvectors of $\mathbf{\Phi}$, and $\mathbf{\Lambda}$ is a diagonal matrix whose diagonal includes L eigenvalues λ_l of $\mathbf{\Phi}$. Noted that λ_l are related to the loop gain A^2 as $\sum_{l=0}^{L-1} \lambda_l = L\Phi(0) = LA^2$. Using eigenvalue decomposition, $\bar{\tilde{\mathbf{u}}}(t)$ is solved in [9] as

$$\bar{\tilde{\mathbf{u}}}(t) = \mathbf{Q}\text{diag}\left\{\frac{1}{1+\mu\lambda_l} + \frac{\mu\lambda_l}{1+\mu\lambda_l} e^{-(1+\mu\lambda_l)\alpha t}\right\}\mathbf{Q}^{-1}\mathbf{h}. \tag{3.50}$$

In order to evaluate the level of cancellation, the power of the residual SI is derived as

$$\begin{aligned} P_{RI}(t) &= \frac{1}{K1K2}\bar{E}\{[z(t)-y(t)]^2\} \\ &= \frac{1}{K1K2}\bar{E}\left\{\left[Re\{Z(t) - \sum_{l=0}^{L-1}[h_l^* - u_l^*(t)]X(t-lT_d)\}e^{j2\pi f_c t}\right]^2\right\} \\ &= \frac{1}{2K1K2}\bar{E}\left\{\left|Z(t) - \sum_{l=0}^{L-1} h_l^* X(t-lT_d)\right|^2\right\} + \frac{1}{2K1K2}\bar{E}\left\{\left|\sum_{l=0}^{L-1} u_l^*(t)X(t-lT_d)]\right|\right\}, \end{aligned} \tag{3.51}$$

where $\bar{E}\{.\}$ denotes combined ensemble and time averaging.

In Section 2.3.3.1, the SI channel is modeled as L taps with the same tap delay as in the ALMS loop so that $Z(t) - \sum_{l=0}^{L-1} h_l^* X(t-lT_d) = 0$. However, in practice the SI

signal is better expressed by $Z(t) = \int_{-\infty}^{\infty} h^*(\tau)X(t-\tau)d\tau$ where h(t) is an arbitrary SI channel impulse response. In this case, the modeled tap coefficients h_l can be obtained by minimizing the normalized modeling error expressed as

$$\epsilon^2 = \frac{1}{K1K2}\bar{E}\left\{\left|Z(t) - \sum_{l=0}^{L-1} h_l^* X(t-lT_d)\right|^2\right\}. \tag{3.52}$$

Applying the principal of orthogonality, that is $\bar{E}\left\{[Z(t) - \sum_{l'=0}^{L-1} h_l^* X(t-l'T_d)]X(t-lT_d)\right\} = 0$, the normalized modeling error is derived in [9] as

$$\epsilon^2 = \int_{-\infty}^{\infty}\int_{-\infty}^{\infty} h^*(\tau)h(\tau')\Phi(\tau-\tau')d\tau d\tau' - \mathbf{h}^H\mathbf{\Phi}\mathbf{h}. \tag{3.53}$$

Substituting (3.50) and (3.52) into (3.51), the normalized power of residual SI can be found as

$$\begin{aligned} P_{RI}(t) = \frac{1}{2}\epsilon^2 + \frac{1}{2}\mathbf{h}^H\mathbf{Q}\text{diag}\Big\{&\frac{\lambda_l}{(1+\mu\lambda_l)^2} + \frac{2\mu\lambda_l^2}{(1+\mu\lambda_l)^2}e^{-(1+\mu\lambda_l)\alpha t} \\ &+ \frac{\mu^2\lambda_l^3}{(1+\mu\lambda_l)^2}e^{-2(1+\mu\lambda_l)\alpha t} - \bar{\lambda}e^{-2(1+\mu\lambda_l)\alpha t}\Big\}\mathbf{Q}^{-1}\mathbf{h}. \end{aligned} \tag{3.54}$$

3.3.3.4 Discussion

1. When applied to a GCW-SAR system where the transmitted signal is deterministic, the ALMS loop behaves similarly as in a FD communication system where the transmitted signal is random. The weighting error functions $\bar{\tilde{\mathbf{u}}}(t)$ converge to $\mathbf{Q}\text{diag}\left\{\frac{1}{1+\mu\lambda_l}\right\}\mathbf{Q}^{-1}\mathbf{h}$ when $t \to \infty$. The convergence speed is driven by the loop gain μA^2 and the LPF parameter α.

2. The above analyses are valid when the ALMS loop parameters satisfy two constraints of the tap delay $T_d \leq 1/B$ and the number of taps L, i.e., $(L-1)T_d \leq T$. These conditions are essential for practical system design.

3.3.4 Simulation Results

The simulations are performed for the GCW-SAR with the following parameters. The transmitted chirp signal has the period T of 40 μs, and its power is 20 dBm with 1 Ω load. The chirp rate is set with $k_r = 2.5\times10^{12}$ Hz^2 so that its bandwidth $B = k_rT = 100$ MHz. In the ALMS loop, the dimensional constants of the multipliers are set as $K_1K_2 = 0.001V^2$ so that $A = 10$. Another loop gain μ is selected as $\mu = 10$. The LPF parameter α is set

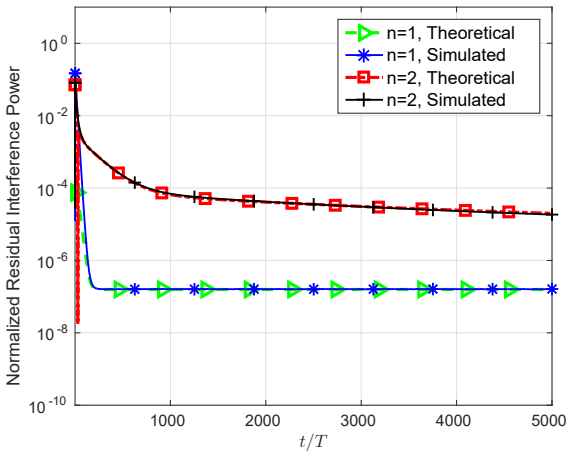

Figure 3.9: The residual SI power in the first scenario for $T_d = 1/nB$, with $n = 1, 2$ and $L = 4, 8$, respectively.

as $5 \times 10^{-5}\text{sec}^{-1}$. The tap delay is chosen as $T_d = \frac{1}{nB}$ with $n = 1, 2$, and the number of taps are $L = 4$ and $L = 8$, respectively.

In the first scenario, the SI channel is selected with the delays being multiples of $T_h = 1/B$, for example $h(t) = 10^{\frac{-25}{20}}\{[\frac{\sqrt{2}}{2} - 0.5j]\delta(t) - 0.4\delta(t - 2T_h) + 0.3\delta(t - 4T_h)\}$. It means that the ALMS loop has the same tap delay with the SI channel so that the modeling error is zero. The simulated and theoretical residual SI powers are presented in Fig. 3.9 for two cases of tap delay with $n = 1, 2$ and $L = 4, 8$, respectively. It is seen that the level of cancellation given by the ALMS loop can be more than 60 dB in case of $T_d = 1/B$.

In the second scenario, the delays of the SI channel are fractional of T_h, for instance, $h(t) = 10^{\frac{-25}{20}}\{[\frac{\sqrt{2}}{2} - 0.5j]\delta(t) - 0.4\delta(t - 0.9T_h) + 0.3\delta(t - 3.3T_h)\}$. The simulation results are presented in Fig. 3.10. In this case, the modeling error has a significant impact on the performance of the ALMS loop. Particularly, the modeling error in case of $T_d = 1/B$ is up to 4×10^{-3}. Hence, the level of cancellation in this scenario is much lower than that in the first scenario for the same $T_d = 1/B$. However, with the finer tap delay in the loop ($T_d = 1/2B$, $L = 8$), the modeling error is reduced to 3.1525×10^{-5}. Hence, the level of cancellation is more than 45 dB which satisfies the requirement of SIC for the GCW-SAR system.

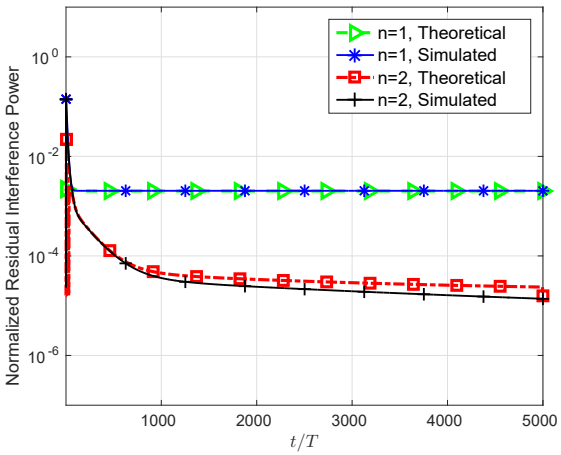

Figure 3.10: The residual SI power in the second scenario for $T_d = 1/nB$ with $n = 1, 2$, and $L = 4, 8$, respectively.

3.3.5 Conclusion

The stationary analysis is applied to investigate the behavior of the ALMS loop for the chirp signal in a GCW-SAR system. Analysis and simulation results show that the ALMS loop works with the deterministic chirp signal in an imaging radar system as well as the random information bearing signal in a wireless communication system. It can be concluded that for the given loop gain, when the tap delay in the loop is properly selected, the level of cancellation more than 45 dB can be achieved. Together with the attenuation in the propagation domain by employing a distance between the transmit and receive antennas, the level of SI can be suppressed up to 70 dB at the input of the ADC. Future works about GCW-SAR can refer to this level of SIC to investigate the impacts of the residual SI.

CHAPTER 4

FREQUENCY DOMAIN CHARACTERIZATION AND PERFORMANCE BOUNDS OF ALMS LOOP

4.1 Introduction

The spectra of residual SI obtained from experiment results in [9] show that the ALMS loop enhances the SI at the two edges of the signal spectrum. However, this phenomenon has not yet been analyzed and its impact on the SIC performance is not fully understood. In addition, as further studied in [58, 59], the properties of transmitted signals have significant impacts on the performance of the ALMS loop, but the roles of the tap delay and the number of taps in the loop in regards to the SIC performance have not been considered. As we all know, as long as the total level of SIC achieved in the propagation and RF domains is sufficient to allow the received signal to be digitized within the ADC's dynamic range, the SIC performance in the RF stage does not show the real impact on the performance of information detection since further optimal receiver algorithms including matched filtering and equalization will be performed in the digital domain. Therefore, it would make more sense to consider the performance of the ALMS loop in the digital domain after the matched filter. However, the analyses on ALMS loop performance in [9, 58, 59] are all conducted at the RF stage.

To overcome the aforementioned shortcoming, in this chapter, the performance of the ALMS loop is analyzed by evaluating the ISRs in both analog and digital domains in the receiver chain. In particular, the ISRs before and after the matched filter are firstly

derived by a steady state analysis, and eigenvalue decomposition is then performed to derive the frequency domain presentation of the ALMS loop. It is proved that although the ALMS loop has an effect of amplifying the frequency components of the residual SI at the edges of the signal spectrum, this effect is significantly reduced by the matched filter, leading to a much lower ISR at the output of the matched filter. Hence, unlike [9], the real effect of the ALMS loop on the SI suppression should be considered after the matched filter in the digital domain instead of before it in the analog domain. Furthermore, the lower bounds of ISRs in both analog and digital domains are derived to characterize the performance of the ALMS loop with regards to the transmitted signal property, the loop gain, the tap spacing, and the number of taps. From the relationship among these parameters, the full potential of SIC given by the ALMS loop can be determined.

Contributions of this chapter are twofold. First, it characterizes the phenomenon of frequency component enhancement produced by the ALMS loop to the residual SI, and proves mathematically that the matched filter reduces this enhancement, leading to a significant improvement of ISR in the digital domain. Second, the lower bound of ISR given by the ALMS loop in the digital domain derived in this chapter allows the designer to determine the expected level of suppression from the parameters of the transceiver and the cancellation circuit. More importantly, this expected level can be achieved by adjusting the remaining parameters when others are under constraints.

The rest of this chapter is organized as follows. Section 4.2 describes the system architecture and the signal models and performs the steady state analysis to find the expressions of ISRs in both analog and digital domains. In Section 4.3, the ISRs are analyzed in the frequency domain and their lower bounds are derived respectively. In Section 4.4, simulations are conducted to verify the theoretical findings. Finally, conclusions are drawn in Section 4.5.

4.2 Steady State Analysis of ALMS Loop

4.2.1 Signal Models

Considering an IBFD system employing the ALMS loop for SIC in the radio frequency domain as in Fig. 4.1. In this chapter, the analyses are only conducted with single-carrier signalling for the simplicity. Therefore, the signal models are described as follows. The transmitted signal $x(t)$ at the output of the power amplifier (PA) is modeled as $x(t) = Re\{X(t)e^{j2\pi f_c t}\}$ where f_c is the carrier frequency, and $X(t)$ is the baseband equivalent

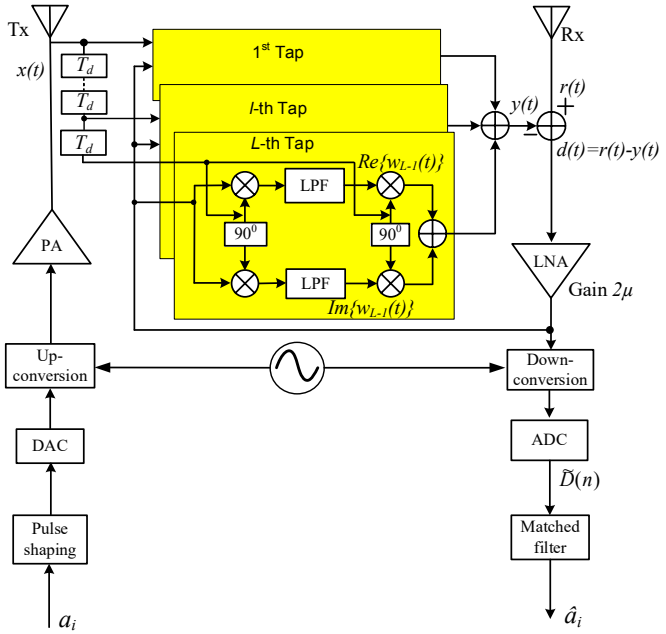

Figure 4.1: The ALMS loop structure.

which can be mathematically modeled as

$$X(t) = \sum_{i=-\infty}^{\infty} a_i V_X p(t - iT_s) \tag{4.1}$$

where a_i is the i-th complex data symbol, T_s is the symbol interval, V_X is the root mean square (RMS) value of the transmitted signal, and $p(t)$ is the pulse shaping function with unit power $\frac{1}{T_s}\int_0^{T_s} |p(t)|^2 dt = 1$. The transmitted data symbols a_i are assumed to be independent of each other, i.e., $E\{a_i^* a_{i'}\} = \begin{cases} 1, \text{ for } i = i' \\ 0, \text{ for } i \neq i' \end{cases}$ where $E\{.\}$ stands for ensemble expectation. The average power of $X(t)$ is defined as $\frac{1}{T_s}\int_0^{T_s} E\{|X(t)|^2\} dt = V_X^2$ over 1 Ω load. Due to the IBFD operation, at the input of the receiver, there are presences of the SI $z(t)$, the desired signal $s(t)$, and the additive Gaussian noise $n(t)$, i.e., $r(t) = z(t) + s(t) + n(t)$. The baseband equivalents of these signals are denoted as $R(t)$, $Z(t)$, $S(t)$ and $N(t)$ respectively. The cancellation signal $y(t)$ is combined from the L taps as

$$y(t) = Re\left\{\sum_{l=0}^{L-1} w_l^*(t) X(t - lT_d) e^{j2\pi f_c (t - lT_d)}\right\}. \tag{4.2}$$

Assume that the SI channel is modeled as an L-stage multi-tap filter where each tap has a coefficient h_l^* and delay T_d. Hence, the baseband equivalent of the SI $z(t)$ can be expressed as $Z(t) = \sum_{l=0}^{L-1} h_l^* X(t - lT_d)$.

The performance of the ALMS loop is represented by the weighting error function defined as $u_l(t) = h_l - w_l(t)e^{j2\pi f_c l T_d}$. As derived in [9, Eq.(11)], $u_l(t)$ can be expressed as

$$u_l(t) = h_l - \frac{\mu\alpha}{K_1 K_2}\int_0^t e^{-\alpha(t-\tau)}\left[\sum_{l'=0}^{L-1} u_{l'}(\tau)X^*(\tau - l'T_d) + S^*(\tau) + N^*(\tau)\right]X(\tau - lT_d)d\tau. \quad (4.3)$$

4.2.2 Steady State Analysis

4.2.2.1 Steady State of Weighting Error Function

Now the steady state analysis is applied to derive the residual SI power and the ISR at the output of the ALMS loop. The system is assumed to be steady after an initial start-up so that all the weighting coefficients are in their converged values. Both ensemble expectation and time averaging denoted as $\bar{E}\{.\}$ are used to evaluate the random processes involved in this analysis. The normalized autocorrelation function of the transmitted signal is defined by

$$\begin{aligned}\Phi(\tau) &= \frac{1}{K_1 K_2}\bar{E}\{X^*(t)X(t-\tau)\} \\ &= \frac{1}{K_1 K_2 T_s}\int_0^{T_s} E\{X^*(t)X(t-\tau)\}dt \\ &= \frac{V_X^2}{K_1 K_2 T_s}\int_{-\infty}^{\infty} p^*(t)p(t-\tau)dt \\ &= \frac{A^2}{T_s}\int_{-\infty}^{\infty} p^*(t)p(t-\tau)dt\end{aligned} \quad (4.4)$$

where $A^2 = V_X^2/K_1K_2 = \Phi(0)$ is the normalized power of the transmitted signal. To simplify (4.3), assuming that the transmitted signal is independent of the desired signal and the additive Gaussian noise, i.e., $\bar{E}\{S^*(t)X(t-\tau)\} = 0$ and $\bar{E}\{N^*(t)X(t-\tau)\} = 0$ for all τ. Performing both ensemble expectation and time averaging and applying the above assumptions to (4.3), we have

$$\bar{u}_l(t) = h_l - \mu\alpha\int_0^t e^{-\alpha(t-\tau)}\sum_{l'=0}^{L-1}\bar{u}_{l'}(\tau)\Phi((l-l')T_d)d\tau, \quad (4.5)$$

or, in matrix form

$$\bar{\mathbf{u}}(t) = \mathbf{h} - \mu\alpha\int_0^t e^{-\alpha(t-\tau)}\mathbf{\Phi}\bar{\mathbf{u}}(t)d\tau \quad (4.6)$$

where $\bar{u}_l(t) = \bar{E}\{u_l(t)\}$, $\bar{\mathbf{u}}(t) = [\bar{u}_0(t),\ \bar{u}_1(t)\ldots\bar{u}_{L-1}(t)]^H$, $\mathbf{h} = [h_0,\ h_1,\ldots,h_{L-1}]^H$, and $\mathbf{\Phi} = \begin{bmatrix} \Phi(0) & \Phi(-T_d) & \cdots & \Phi(-(L-1)T_d) \\ \Phi(T_d) & \Phi(0) & \cdots & \Phi(-(L-2)T_d) \\ \vdots & \vdots & \ddots & \vdots \\ \Phi((L-1)T_d) & \Phi((L-2)T_d) & \cdots & \Phi(0) \end{bmatrix}$. When $t \to \infty$, $\bar{\mathbf{u}}(t)$ converge to

their steady-state values $\bar{\tilde{\mathbf{u}}}$ so that $\bar{\tilde{\mathbf{u}}}(t)$ can be taken out of the integral in (4.6). It is also noted that $\alpha \int_0^t e^{-\alpha(t-\tau)} d\tau \Big|_{t\to\infty} \to 1$. Therefore, (4.6) becomes

$$\bar{\tilde{\mathbf{u}}} = \mathbf{h} - \mu \mathbf{\Phi} \bar{\tilde{\mathbf{u}}} \tag{4.7}$$

and hence

$$\bar{\tilde{\mathbf{u}}} = (\mathbf{I}_L + \mu \mathbf{\Phi})^{-1} \mathbf{h}. \tag{4.8}$$

4.2.2.2 Interference Suppression Ratios

ISR is an important metric to evaluate the performance of the cancellation circuit. In this subsection, the closed-form equations of ISRs before and after the matched filter are derived in the analog domain and digital domain, respectively.

ISR in analog domain: After SIC, the normalized power of residual SI $v(t) = z(t) - y(t)$ is derived as

$$\begin{aligned}
P_v(t) &= \frac{1}{K_1 K_2} \bar{E}\Big\{[z(t) - y(t)]^2\Big\} \\
&= \frac{1}{K_1 K_2} \bar{E}\Big\{\Big[Re\Big\{\Big[Z(t) - \sum_{l=0}^{L-1} (h_l^* - u_l^*(t)) X(t - lT_d)\Big] e^{j2\pi f_c t}\Big\}\Big]^2\Big\} \\
&= \frac{1}{2K_1 K_2} \bar{E}\Big\{\Big|Z(t) - \sum_{l=0}^{L-1} (h_l^* - u_l^*(t)) X(t - lT_d)\Big|^2\Big\} \\
&= \frac{1}{2K_1 K_2} \bar{E}\Big\{\Big[\sum_{l=0}^{L-1} u_l^*(t) X(t - lT_d) \sum_{l'=0}^{L-1} u_{l'}(t) X^*(t - l'T_d)\Big]\Big\} \\
&= \frac{1}{2} \bar{E}\Big\{\sum_{l=0}^{L-1} \sum_{l'=0; l' \neq l}^{L-1} u_l^*(t) \Phi\big((l - l')T_d\big) u_{l'}(t) + \Phi(0) \sum_{l=0}^{L-1} |u_l(t)|^2\Big\} \\
&= \frac{1}{2} \bar{\tilde{\mathbf{u}}}^H(t) \big[\mathbf{\Phi} - \Phi(0)\mathbf{I}_L\big] \bar{\tilde{\mathbf{u}}}(t) + \frac{1}{2} \Phi(0) \sum_{l=0}^{L-1} \bar{\tilde{u}}_l^2(t)
\end{aligned} \tag{4.9}$$

where $\bar{\tilde{u}}_l^2(t) = \bar{E}\{|u_l(t)|^2\}$ is the time-averaged mean square value of $u_l(t)$. From (4.3), following the steps shown in Appendix B in [9], when $\frac{d\bar{\tilde{u}}_l^2(t)}{dt} = 0$, $\bar{\tilde{u}}_l^2(t)$ satisfies the equation

$$(1 + \mu A^2) \sum_{l=0}^{L-1} \bar{\tilde{u}}_l^2(t) = Re\{\bar{\tilde{\mathbf{u}}}^H \mathbf{h}\} - \mu \bar{\tilde{\mathbf{u}}}^H (\mathbf{\Phi} - A^2 \mathbf{I}_L) \bar{\tilde{\mathbf{u}}}. \tag{4.10}$$

Substituting (4.8) to (4.10), we have

$$\sum_{l=0}^{L-1} \bar{\tilde{u}}_l^2(t) = \mathbf{h}^H (\mathbf{I}_L + \mu \mathbf{\Phi})^{-2} \mathbf{h} \tag{4.11}$$

and the steady state power of the residual interference is obtained from (4.9) as

$$P_v = \frac{1}{2}\mathbf{h}^H(\mathbf{I}_L + \mu\mathbf{\Phi})^{-1}\mathbf{\Phi}(\mathbf{I}_L + \mu\mathbf{\Phi})^{-1}\mathbf{h}. \tag{4.12}$$

If there was no cancellation, the normalized SI power would be

$$\begin{aligned} P_z &= \frac{1}{K_1K_2}\bar{E}\{[z(t)]^2\} \\ &= \frac{1}{K_1K_2}\bar{E}\left\{\left[Re\left\{\sum_{l=0}^{L-1} h_l^* X(t-lT_d)e^{j2\pi f_c t}\right\}\right]^2\right\} \\ &= \frac{1}{2K_1K_2}\bar{E}\left\{\sum_{l=0}^{L-1} h_l^* X(t-lT_d)\sum_{l'=0}^{L-1} h_{l'} X^*(t-l'T_d)\right\} \\ &= \frac{1}{2K_1K_2}\sum_{l=0}^{L-1}\sum_{l'=0}^{L-1} h_l^*\bar{E}\left\{X(t-lT_d)X^*(t-l'T_d)\right\}h_{l'} \\ &= \frac{1}{2}\sum_{l=0}^{L-1}\sum_{l'=0}^{L-1} h_l^*\Phi\big((l-l')T_d\big)h_{l'} = \frac{1}{2}\mathbf{h}^H\mathbf{\Phi}\mathbf{h}. \end{aligned} \tag{4.13}$$

Therefore, ISR before the matched filter in the analog domain, denoted as ISR_a, is determined by

$$ISR_a = \frac{P_v}{P_z} = \frac{\mathbf{h}^H(\mathbf{I}_L + \mu\mathbf{\Phi})^{-1}\mathbf{\Phi}(\mathbf{I}_L + \mu\mathbf{\Phi})^{-1}\mathbf{h}}{\mathbf{h}^H\mathbf{\Phi}\mathbf{h}}. \tag{4.14}$$

ISR in digital domain: After down-converted to baseband, the residual SI, denoted as $V(t)$, is expressed as

$$\begin{aligned} V(t) &= Z(t) - Y(t) \\ &= \sum_{l=0}^{L-1} h_l^* X(t-lT_d) - \sum_{l=0}^{L-1} w_l^*(t)X(t-lT_d)e^{-j2\pi f_c lT_d} \\ &= \sum_{l=0}^{L-1} u_l^*(t)X(t-lT_d). \end{aligned} \tag{4.15}$$

After the matched filter with the impulse response $p^*(-t)$, the filtered version of $V(t)$ is obtained as

$$\tilde{V}(t) = V(t) * p^*(-t) = \sum_{l=0}^{L-1} u_l^*(t)\tilde{X}(t-lT_d) \tag{4.16}$$

where $*$ stands for a linear convolution operation and

$$\tilde{X}(t) = X(t) * p^*(-t) \tag{4.17}$$

is the filtered version of the transmitted baseband signal. Similarly, the steady normalized power of the filtered residual SI is calculated as

$$\begin{aligned} P_{\tilde{V}} &= \frac{1}{K_1 K_2}\bar{E}\{|\tilde{V}(t)|^2\} \\ &= \frac{1}{K_1 K_2}\bar{E}\left\{\sum_{l=0}^{L-1} u_l^*(t)\tilde{X}(t-lT_d)\sum_{l'=0}^{L-1} u_{l'}(t)\tilde{X}^*(t-l'T_d)\right\} \\ &= \sum_{l=0}^{L-1}\sum_{l'=0,l\neq l'}^{L-1} \bar{\tilde{u}}_l^*(t)\Theta\big((l-l')T_d\big)\bar{\tilde{u}}_{l'}(t) + \Theta(0)\sum_{l=0}^{L-1}\bar{\tilde{u}}_l^2(t) \\ &= \bar{\tilde{\mathbf{u}}}^H(t)(\boldsymbol{\Theta}-\Theta(0)\mathbf{I}_L)\bar{\tilde{\mathbf{u}}}(t) + \Theta(0)\sum_{l=0}^{L-1}\bar{\tilde{u}}_l^2(t) \\ &= \mathbf{h}^H(\mathbf{I}_L+\mu\boldsymbol{\Phi})^{-1}\boldsymbol{\Theta}(\mathbf{I}_L+\mu\boldsymbol{\Phi})^{-1}\mathbf{h} \end{aligned} \tag{4.18}$$

where $\Theta(\tau) = \frac{1}{K_1K_2}\bar{E}\{\tilde{X}(t)\tilde{X}^*(t-\tau)\}$ and $\boldsymbol{\Theta} = \begin{bmatrix} \Theta(0) & \Theta(-T_d) & \cdots & \Theta(-(L-1)T_d) \\ \Theta(T_d) & \Theta(0) & \cdots & \Theta(-(L-2)T_d) \\ \vdots & \vdots & \ddots & \vdots \\ \Theta((L-1)T_d) & \Theta((L-2)T_d) & \cdots & \Theta(0) \end{bmatrix}$ are the normalized autocorrelation function of $\tilde{X}(t)$ and the corresponding autocorrelation matrix, respectively.

Meanwhile, if there was no cancellation, the steady normalized SI power after the matched filter would be

$$\begin{aligned} P_{\tilde{Z}} &= \frac{1}{K_1K_2}\bar{E}\{|Z(t)*p^*(-t)|^2\} \\ &= \frac{1}{K_1K_2}\bar{E}\left\{\Big|\sum_{l=0}^{L-1} h_l^*\tilde{X}(t-lT_d)\Big|^2\right\} \\ &= \sum_{l=0}^{L-1}\sum_{l'=0}^{L-1} h_l^*\Theta((l-l')T_d)h_{l'} \\ &= \mathbf{h}^H\boldsymbol{\Theta}\mathbf{h}. \end{aligned} \tag{4.19}$$

Therefore, the ISR after the matched filter in the digital domain, denoted as ISR_d, is

$$ISR_d = \frac{P_{\tilde{V}}}{P_{\tilde{Z}}} = \frac{\mathbf{h}^H(\mathbf{I}_L+\mu\boldsymbol{\Phi})^{-1}\Theta(\mathbf{I}_L+\mu\boldsymbol{\Phi})^{-1}\mathbf{h}}{\mathbf{h}^H\boldsymbol{\Theta}\mathbf{h}}. \tag{4.20}$$

4.3 Frequency-Domain Analysis of Residual SI

4.3.1 Eigen-Decomposition of Autocorrelation Matrices

The $L \times L$ matrix $\mathbf{\Phi}$ can be decomposed as $\mathbf{\Phi} = \mathbf{Q}\mathbf{\Lambda}\mathbf{Q}^{-1}$ where $\mathbf{Q}$ is the orthonormal modal matrix whose columns are the L eigenvectors of $\mathbf{\Phi}$ and $\mathbf{\Lambda} = \begin{pmatrix} \lambda_0 & 0 & \cdots & 0 \\ 0 & \lambda_1 & \cdots & 0 \\ \vdots & \vdots & \ddots & \vdots \\ 0 & 0 & \cdots & \lambda_{L-1} \end{pmatrix}$ is the spectral matrix whose main diagonal elements are the L eigenvalues of $\mathbf{\Phi}$. When LT_d is sufficiently large, the autocorrelation matrix $\mathbf{\Phi}$ can be approximated as a circulant matrix $\tilde{\mathbf{\Phi}}$ composed of a periodic autocorrelation function $\tilde{\Phi}(\tau) = \sum_{l=-\infty}^{\infty} \Phi(\tau + lLT_d)$. As proved in [60], the circulant matrix $\tilde{\mathbf{\Phi}}$ can be decomposed as $\tilde{\mathbf{\Phi}} = \mathbf{F}\mathbf{S}_\mathbf{X}\mathbf{F}^{-1}$ where $\mathbf{F}$ is the discrete Fourier transform (DFT) matrix of order L, $\mathbf{F} = \begin{pmatrix} 1 & 1 & \cdots & 1 \\ 1 & e^{-j\omega_1} & \cdots & e^{-j(L-1)\omega_1} \\ \vdots & \vdots & \ddots & \vdots \\ 1 & e^{-j\omega_{L-1}} & \cdots & e^{-j(L-1)\omega_{L-1}} \end{pmatrix}$ with $\omega_k = \frac{2\pi k}{L}, k = 0,1,\ldots,L-1$, $\mathbf{S}_X = \text{diag}\{S_X(e^{j\omega_0}), S_X(e^{j\omega_1}), \ldots, S_X(e^{j\omega_{L-1}})\}$, and $S_X(e^{j\omega_k})$ are obtained by taking the DFT of $\tilde{\Phi}(lT_d)$, i.e.,

$$S_X(e^{j\omega_k}) = \sum_{l=0}^{L-1} \tilde{\Phi}(lT_d) e^{-j\omega_k l} \tag{4.21}$$

for $k = 0,1,\ldots,L-1$, which are the L samples of the normalized power spectrum $S_X(e^{j\omega})$ of the transmitted signal sequence $X(nT_d)$ uniformly spaced about the unit circle. It means that when L is sufficiently large, the eigenvalues λ_k can be approximated as the power spectrum samples $S_X(e^{j\omega_k})$. To confirm this approximation, the eigenvalues λ_k are compared with the power spectrum $S_X(e^{j\omega_k})$ as below.

Suppose that the transmitter employs a root raised cosine pulse shaping filter. The autocorrelation function $\Phi(t)$ is a raised cosine pulse, which has the frequency response

$$P(f) = \begin{cases} T_s & \text{for } 0 \le |f| < \frac{1-\beta}{2T_s} \\ \frac{T_s}{2}\left[1 + \cos\left(\frac{\pi T_s}{\beta}(f - \frac{1-\beta}{2T_s})\right)\right] & \text{for } \frac{1-\beta}{2T_s} \le |f| \le \frac{1+\beta}{2T_s} \\ 0 & \text{for } |f| > \frac{1+\beta}{2T_s} \end{cases} \tag{4.22}$$

where β is the roll-off factor. Hence, the normalized power spectrum of $X(t)$ is $A^2P(f)$. With the sampling period T_d, the relationship between $S_X(e^{j\omega})$ and $P(f)$ can be expressed

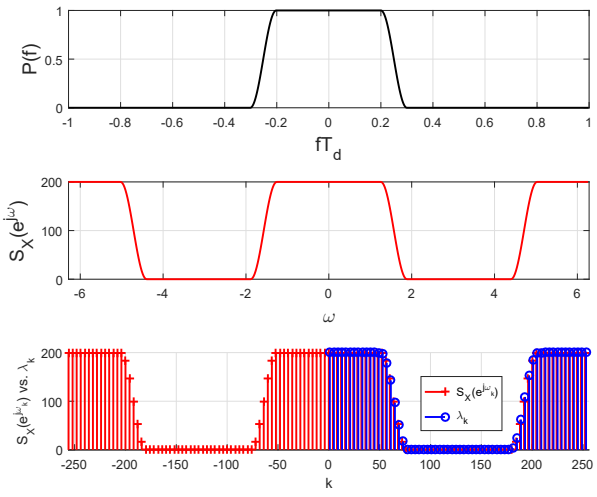

Figure 4.2: (a) Raised cosine spectrum; (b) $S_X(e^{j\omega})$; (c) $S_X(e^{j\omega_k})$ versus eigenvalues λ_k, with $L = 256$, $A^2 = 100$, $\beta = 0.2$, $T_d = T_s/2$, $T_s = 1$.

as

$$S_X(e^{j\omega}) = \frac{1}{T_d} \sum_{n=-\infty}^{\infty} A^2 P(\frac{\omega}{2\pi T_d} - \frac{n}{T_d}). \tag{4.23}$$

If $T_d \leq T_s/(1+\beta)$, there will be no spectral overlapping and hence

$$S_X(e^{j\omega}) = \frac{A^2}{T_d} P(\frac{\omega}{2\pi T_d}), \text{ for } -\pi < \omega < \pi. \tag{4.24}$$

Fig. 4.2 shows the raised cosine spectrum $P(f)$, $S_X(e^{j\omega})$, $S_X(e^{j\omega_k})$, and properly ordered λ_k for $L = 256$, $A^2 = 100$, $\beta = 0.2$, and $T_d = T_s/2$ where T_s is normalized to 1. We see that λ_k are very close to $S_X(e^{j\omega_k})$.

The same approximation can also be applied to the autocorrelation matrix $\mathbf{\Theta}$, i.e., it is close to a circulant matrix $\tilde{\mathbf{\Theta}}$ when L is sufficiently large. In this case, $\tilde{\mathbf{\Theta}}$ can be decomposed as $\tilde{\mathbf{\Theta}} = \mathbf{F}\mathbf{S}_{\tilde{X}}\mathbf{F}^{-1}$ where $\mathbf{S}_{\tilde{X}} = \text{diag}\{S_{\tilde{X}}(e^{j\omega_0}), S_{\tilde{X}}(e^{j\omega_1}), \ldots, S_{\tilde{X}}(e^{j\omega_{L-1}})\}$; $S_{\tilde{X}}(e^{j\omega_k})$ for $k = 0, \ldots, L-1$ are the L spectrum components obtained by taking DFT of $\tilde{\Theta}(lT_d)$ with $\tilde{\Theta}(\tau) = \sum_{l=-\infty}^{\infty} \Theta(\tau + lLT_d)$, and $S_{\tilde{X}}(e^{j\omega}) = \frac{A^2}{T_d} P^2(\frac{\omega}{2\pi T_d})$ for $-\pi < \omega < \pi$.

4.3.2 Frequency Domain Characterization of ALMS Loop

From the above decomposition, (4.14) and (4.20) can be simplified as

$$\begin{aligned} ISR_a &= \frac{\mathbf{h}^H\mathbf{F}(\mathbf{I}_L+\mu\mathbf{S}_X)^{-1}\mathbf{F}^{-1}\mathbf{F}\mathbf{S}_X\mathbf{F}^{-1}\mathbf{F}(\mathbf{I}_L+\mu\mathbf{S}_X)^{-1}\mathbf{F}^{-1}\mathbf{h}}{\mathbf{h}^H\mathbf{F}\mathbf{S}_X\mathbf{F}^{-1}\mathbf{h}} \\ &= \frac{\mathbf{h}^H\mathbf{F}\text{diag}\left\{\frac{S_X(e^{j\omega_k})}{\left[1+\mu S_X(e^{j\omega_k})\right]^2}\right\}\mathbf{F}^{-1}\mathbf{h}}{\mathbf{h}^H\mathbf{F}\text{diag}\{S_X(e^{j\omega_k})\}\mathbf{F}^{-1}\mathbf{h}} \\ &= \frac{\sum_{k=0}^{L-1}|H(e^{i\omega_k})|^2\frac{S_X(e^{j\omega_k})}{\left[1+\mu S_X(e^{j\omega_k})\right]^2}}{\sum_{k=0}^{L-1}|H(e^{i\omega_k})|^2 S_X(e^{j\omega_k})}, \end{aligned} \tag{4.25}$$

and

$$\begin{aligned} ISR_d &= \frac{\mathbf{h}^H\mathbf{F}(\mathbf{I}_L+\mu\mathbf{S}_X)^{-1}\mathbf{F}^{-1}\mathbf{F}\mathbf{S}_{\tilde{X}}\mathbf{F}^{-1}\mathbf{F}(\mathbf{I}_L+\mu\mathbf{S}_X)^{-1}\mathbf{F}^{-1}\mathbf{h}}{\mathbf{h}^H\mathbf{F}\mathbf{S}_{\tilde{X}}\mathbf{F}^{-1}\mathbf{h}} \\ &= \frac{\mathbf{h}^H\mathbf{F}\text{diag}\left\{\frac{S_{\tilde{X}}(e^{j\omega_k})}{\left[1+\mu S_X(e^{j\omega_k})\right]^2}\right\}\mathbf{F}^{-1}\mathbf{h}}{\mathbf{h}^H\mathbf{F}\text{diag}\{S_{\tilde{X}}(e^{j\omega_k})\}\mathbf{F}^{-1}\mathbf{h}} \\ &= \frac{\sum_{k=0}^{L-1}|H(e^{j\omega_k})|^2\frac{S_{\tilde{X}}(e^{j\omega_k})}{\left[1+\mu S_X(e^{j\omega_k})\right]^2}}{\sum_{k=0}^{L-1}|H(e^{j\omega_k})|^2 S_{\tilde{X}}(e^{j\omega_k})} \end{aligned} \tag{4.26}$$

where $H(e^{j\omega_k})$ is the frequency response of the SI channel. It can be seen from (4.25) and (4.26) that, in the frequency domain, the residual SI can be decomposed into two components. The first component is the frequency response of the SI channel $H(e^{j\omega_k})$. The second component in (4.25) (i.e., in the analog domain before the matched filter) is a frequency dependent attenuation factor introduced by the ALMS loop as $F_a(e^{j\omega}) = \frac{S_X(e^{j\omega})}{\left[1+\mu S_X(e^{j\omega})\right]^2}$. Also, in (4.26), the second component in the digital domain after the matched filter is a frequency dependent attenuation factor determined by both the ALMS loop and the matched filter as $F_d(e^{j\omega}) = \frac{S_{\tilde{X}}(e^{j\omega})}{\left[1+\mu S_X(e^{j\omega})\right]^2}$. Therefore, the residual SI before and after the matched filter can be analyzed in the frequency domain by comparing their second components. $F_a(e^{j\omega})$ and $F_d(e^{j\omega})$ with various values of β are plotted in Fig. 4.3, respectively.

Fig. 4.3 reveals that the ALMS loop has an effect of amplifying the frequency components of the residual SI leading to a peak at the edge of the signal spectrum. As a result, the ISR in the analog domain before the matched filter is higher when the roll-off factor is larger. However, this effect is significantly reduced by the matched filter as the peak no longer exists in $F_d(e^{j\omega})$. Hence, the ISR will be significantly improved in

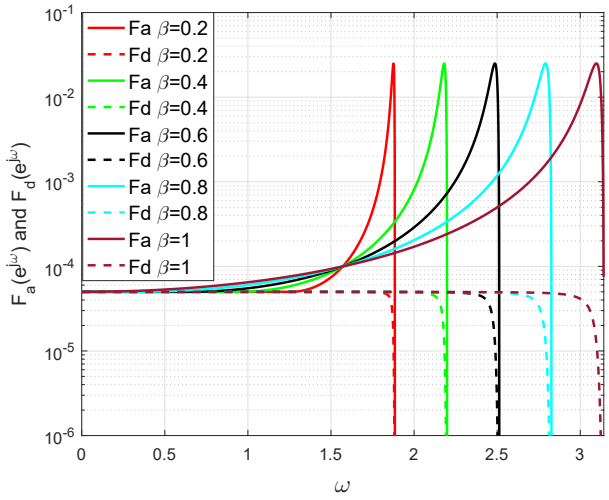

Figure 4.3: Frequency dependent attenuation factors with various values of β, $L = 256$, $A^2 = 100$, $T_d = T_s/2$.

the digital domain. It also means that the effect of the signal spectrum on ISR reduces significantly when it is considered in the digital domain. Therefore, it is concluded that the performance of the ALMS loop evaluated in the digital domain after the matched filter rather than in the analog domain as in [9] makes more sense to the IBFD system.

4.3.3 Performance Lower Bounds

The ISRs discussed in Section 4.3.1 are valid for a given SI channel. To derive the lower bounds of ISRs over random realizations of SI channels, defining the average ISRs in the analog domain and digital domain, respectively as

$$\begin{aligned}\overline{ISR}_a &= \frac{E_h\{P_v\}}{E_h\{P_z\}} = \frac{\sum_{k=0}^{L-1} E_h\{|H(e^{j\omega_k})|^2\} \frac{S_X(e^{j\omega_k})}{\left[1+\mu S_X(e^{j\omega_k})\right]^2}}{\sum_{k=0}^{L-1} E_h\{|H(e^{j\omega_k})|^2\} S_X(e^{j\omega_k})}, \\ &= \frac{\sum_{k=0}^{L-1} \frac{S_X(e^{j\omega_k})}{\left[1+\mu S_X(e^{j\omega_k})\right]^2}}{\sum_{k=0}^{L-1} S_X(e^{j\omega_k})}\end{aligned} \tag{4.27}$$

and

$$\begin{aligned}\overline{ISR}_d &= \frac{E_h\{P_{\tilde{V}}\}}{E_h\{P_{\tilde{Z}}\}} = \frac{\sum_{k=0}^{L-1} E_h\{|H(e^{j\omega_k})|^2\} \frac{S_{\tilde{X}}(e^{j\omega_k})}{\left[1+\mu S_X(e^{j\omega_k})\right]^2}}{\sum_{k=0}^{L-1} E_h\{|H(e^{j\omega_k})|^2\} S_{\tilde{X}}(e^{j\omega_k})} \\ &= \frac{\sum_{k=0}^{L-1} \frac{S_{\tilde{X}}(e^{j\omega_k})}{\left[1+\mu S_X(e^{j\omega_k})\right]^2}}{\sum_{k=0}^{L-1} S_{\tilde{X}}(e^{j\omega_k})}\end{aligned} \tag{4.28}$$

where $E_h\{.\}$ denotes expectation over the SI channel and $E_h\{|H(e^{j\omega_k})|^2\}$ is a constant for SI channels with independent and zero-mean tap coefficients (see Appendix A.1). Clearly, $\overline{ISR}_a$ and $\overline{ISR}_d$ can be purely examined by the spectrum components $S_X(e^{j\omega_k})$ and $S_{\tilde{X}}(e^{j\omega_k})$. To find the closed-form equation of $\overline{ISR}_a$ and $\overline{ISR}_d$, letting $L \to \infty$, the discrete components $S_X(e^{j\omega_k})$ and $S_{\tilde{X}}(e^{j\omega_k})$) can be replaced by the continuous power spectra $S_X(e^{j\omega})$ and $S_{\tilde{X}}(e^{j\omega})$, respectively. The lower bounds of $\overline{ISR}_a$ and $\overline{ISR}_d$ are obtained as

$$\begin{aligned}ISRLB_a = \overline{ISR}_a|_{L\to\infty} &= \frac{\frac{1}{2\pi}\int_0^{2\pi} \frac{S_X(e^{j\omega})}{\left[1+\mu S_X(e^{j\omega})\right]^2} d\omega}{\frac{1}{2\pi}\int_0^{2\pi} S_X(e^{j\omega}) d\omega} \\ &= \frac{\frac{1}{2\pi}\int_{-\pi}^{\pi} \frac{S_X(e^{j\omega})}{\left[1+\mu S_X(e^{j\omega})\right]^2} d\omega}{\frac{1}{2\pi}\int_{-\pi}^{\pi} S_X(e^{j\omega}) d\omega} = \frac{\int_{-1/2T_d}^{1/2T_d} \frac{A^2 P(f)}{\left[1+\mu\frac{A^2}{T_d}P(f)\right]^2} df}{\int_{-1/2T_d}^{1/2T_d} A^2 P(f) df},\end{aligned} \tag{4.29}$$

and

$$\begin{aligned}ISRLB_d = \overline{ISR}_d|_{L\to\infty} &= \frac{\frac{1}{2\pi}\int_0^{2\pi} \frac{S_{\tilde{X}}(e^{j\omega})}{\left[1+\mu S_X(e^{j\omega})\right]^2} d\omega}{\frac{1}{2\pi}\int_0^{2\pi} S_{\tilde{X}}(e^{j\omega}) d\omega} \\ &= \frac{\frac{1}{2\pi}\int_{-\pi}^{\pi} \frac{S_{\tilde{X}}(e^{j\omega})}{\left[1+\mu S_X(e^{j\omega})\right]^2} d\omega}{\frac{1}{2\pi}\int_{-\pi}^{\pi} S_{\tilde{X}}(e^{j\omega}) d\omega} = \frac{\int_{-1/2T_d}^{1/2T_d} \frac{A^2 P^2(f)}{\left[1+\mu\frac{A^2}{T_d}P(f)\right]^2} df}{\int_{-1/2T_d}^{1/2T_d} A^2 P^2(f) df}\end{aligned} \tag{4.30}$$

respectively. Assuming the raised cosine transmitted signal spectrum, the closed-form $ISRLB_a$ and $ISRLB_d$ in (4.29) and (4.30) are found (see Appendix A.2) as

$$ISRLB_a = \frac{1+\beta(\sqrt{a+1}-1)}{(1+a)^2}, \tag{4.31}$$

and

$$ISRLB_d = \frac{1+\beta\left[\frac{2(a+1)^2}{a^2}\left(1-\frac{1}{\sqrt{a+1}}-\frac{a\sqrt{a+1}}{2(a+1)^2}\right)-1\right]}{(1+a)^2(1-\beta/4)}. \tag{4.32}$$

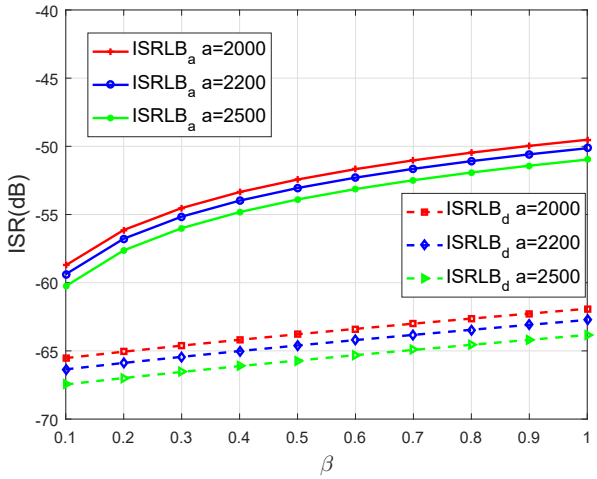

Figure 4.4: ISR lower bounds versus β with $a = 2000, 2200,$ and 2500.

where $a = \mu A^2 T_s / T_d$. It is obvious from these lower bounds that in the ideal case ($\beta = 0$) the ultimate level of cancellation is $ISRLB_u = 1/(1 + \frac{T_s}{T_d}\mu A^2)^2$. Comparison between $ISRL_a$ and $ISRLB_d$ with three example values of a is presented in Fig. 4.4. From (4.27), (4.28), (4.31), (4.32), and Fig. 4.4, some important observations are derived as below.

1. The level of cancellation given by the ALMS loop is determined by the loop gain μA^2, the roll-off factor β the tap delay T_d, and the number of taps L. It means that the expected level of cancellation can be achieved by either increasing the loop gain μA^2 or reducing the tap delay T_d. However for the latter case, larger number of taps L is required so that LT_d is sufficiently large and ISR_a can approach its lower bound.

2. $ISRLB_a$ increases significantly as the roll-off factor increases. As shown in Fig. 4.4, $ISRLB_a$ for $\beta = 1$ is about 10 dB higher than that for $\beta = 0.1$. However, the difference in $ISRLB_d$ is only about 3 dB over the whole range of β. This indicates that the matched filter significantly reduces the effects of the roll-off factor and the impact of the spectrum of the transmitted signal becomes negligible in the digital domain.

The first observation is a crucial conclusion for system design because it allows the designer to determine these parameters based on the expected level of cancellation given by the ALMS loop. Furthermore, understanding the relationship among these factors also allows the flexibility in designing the cancellation circuit. For example, if the power

of the system is limited, i.e, the gain of the ALMS loop is not high enough, the level of cancellation can still be achieved by a finer tap spacing. In case the size of the ALMS loop is constrained, the loop gain must be increased. The second observation once again states that the performance of the ALMS loop must be considered in the digital domain, and the best level of cancellation given by the ALMS loop is $ISRLB_d$.

4.4 Simulation Results

To verify the analytical results presented in Section 4.3, simulations are conducted in MATLAB for a single-carrier IBFD system which uses QPSK modulation and symbol duration $T_s = 20$ ns. The pulse shaping filter and the matched filter are both root raised cosine pulses with the roll-off factor β. The transmitted power is set to 0 dBm over 50 Ohm load. The transmitted power over 1 Ohm load is found by 0 dBm + $10\log_{10}(50) = 17$ dBm. Hence, the mean squared amplitude of the transmitted signal for 1 Ohm load is calculated by $V_X^2 = 2 \times 10^{(17-30)/10} = 0.1\ V^2$. The LNA in the receiver is selected with the gain of $\mu = 10$. The ALMS loop has the tap spacing $T_d = T_s/2$ and the number of taps L. The multiplier constants in all the taps are the same and are selected as $K_1K_2 = 0.001\ V^2$. Therefore, the gain of the ALMS loop is $\mu A^2 = 10 \times (0.1/0.001) = 1000$. By considering propagation loss between Tx and Rx antennas, the SI power is set to 25 dB lower than the transmitted signal power.

In the first simulation, the SI channel is chosen as $h(t) = 10^{\frac{-25}{20}}\{[\frac{\sqrt{2}}{2} - 0.5j]\delta(t) - 0.4\delta(t - 0.9T_s) + 0.3\delta(t - 3.3T_s)\}$, which means that the delays of the reflected paths are fractional of T_s. The ALMS loop has $L = 8$ taps with $T_s/2$ tap spacing. Both pulse shaping filter and matched filter have the roll-off factor of $\beta = 0.5$. The power spectrum densities (PSDs) of the baseband equivalent of the SI $Z(t)$, the residual SI in the analog domain $V(t)$, and the residual SI in the digital domain after the matched filter $\tilde{V}(t)$ are presented in Fig. 4.5. It is seen that there are two peaks at the edges of the $V(t)$. However, these peaks are removed in the spectrum of $\tilde{V}(t)$. This simulation confirms the analyses in Section 4.3.2.

In the second simulation, the SI channel has L propagation paths whose coefficients h_l are all independent and have a normal distribution with zero-mean. The power delay profile of the channel has an exponential distribution with the root mean square delay spread $\sigma = LT_s/4$. The ISRs at each point of the roll-off factor β for different values of L are calculated and averaged out over 1000 iterations. The simulated $\overline{ISR}_a$, $\overline{ISR}_d$ and their corresponding lower bounds $ISRLB_a$, $ISRLB_d$ are presented in Fig.

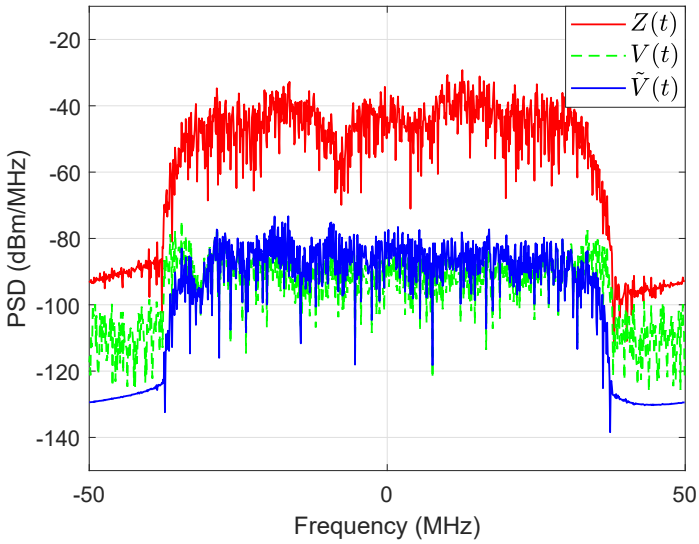

Figure 4.5: PSDs of the SI $Z(t)$, residual SI $V(t)$, and residual SI after the matched filter $\tilde{V}(t)$ with $\beta = 0.5,\ \mu A^2 = 1000,\ T_d = T_s/2,$ and $L = 8$.

4.6 for different values of L. The inset shows a closer look of $\overline{ISR}_d$. Clearly, when L is larger, $\overline{ISR}_a$ and $\overline{ISR}_d$ are closer to their lower bounds, respectively. This is because the autocorrelation matrix can be well approximated to a circulant matrix and the summation in (4.27) and (4.28) approaches the integration when L is sufficiently large. Note that in our analyses, the SI channel is assumed to have the same number of paths as in the ALMS loop. As a result, the SI channels with small number of taps are much shorter compared to those with larger number of taps. Therefore, $\overline{ISR}_a$ with smaller L go beyond the lower bound with infinite L. However, the matched filter reduces the effects of the SI channel so that $\overline{ISR}_d$ are still bounded by $ISRLB_d$.

4.5 Conclusion

In this chapter, the residual SI powers and the ISRs of an ALMS loop in both analog and digital domains of an IBFD system have been derived using the steady state analysis. The expression of the ISR in the time domain is then converted into the frequency domain by eigenvalue decomposition. From the frequency domain presentation, it is proved that the matched filter has an effect of reducing the peak frequency response of the ALMS loop so that the problem of frequency component enhancement caused by the ALMS loop to the residual SI can be significantly reduced in the digital domain. The corresponding

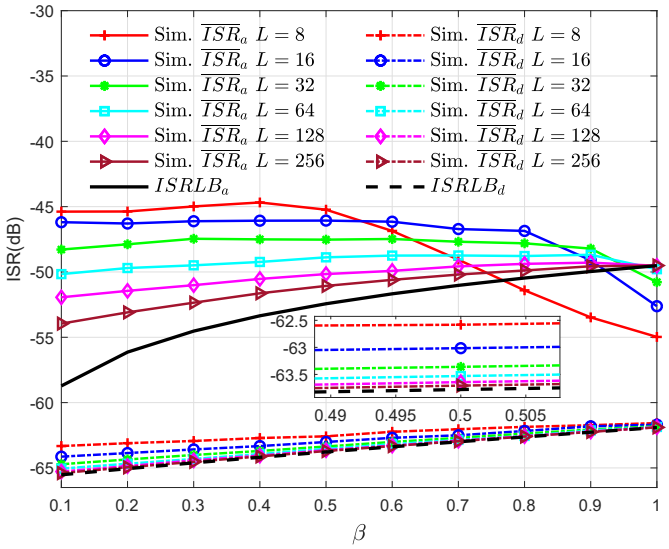

Figure 4.6: ISRs in the analog domain and digital domain versus β with $\mu A^2 = 1000$, $T_d = T_s/2$.

lower bounds of ISRs in both analog and digital domains have also been derived from frequency domain expressions. Comparison between these lower bounds shows that the performance of the ALMS loop should be considered in the digital domain and it is determined by four factors, namely, the loop gain μA^2, the tap delay T_d, the number of taps L, and the roll-off factor β. The finding of these lower bounds allows the designer to determine the desired level of cancellation given by the ALMS loop. It also provides a room to trade off among these factors to achieve the level of cancellation within given constraints.

CHAPTER 5

ALMS LOOP WITH IQ IMBALANCE

5.1 Introduction

The studies on the behaviors of the ALMS loop published in [9, 58, 59, 61] are all conducted under the perfect I/Q imbalance-free condition of the loop. However, since I/Q imbalances always exist in the modulators and demodulators used in the ALMS loop, it is important to examine how these I/Q imbalances impact on the loop performance, which is the main motivation of this Chapter. To the best of the author's knowledge, little work has been published in the literature considering this problem. Instead, most of the publications investigate the impact of I/Q imbalances appearing in the transceivers [62–66].

In this chapter, the ALMS loop proposed in [9] with frequency independent I/Q imbalances will be investigated in both single-carrier and OFDM FD systems. Firstly, the effect of I/Q imbalance on the loop gain is examined and compensated by adjusting the gains at other points in the loop. Secondly, the effect of I/Q imbalance on the cancellation performance is derived and quantified. Due to I/Q imbalance, the level of SIC given by the ALMS loop is degraded and can be presented by a degradation factor (DF). However, by averaging over random realizations of the SI channel, the DF is shown to be insignificant even under severe amplitude and phase errors. In addition, an upper bound of the DF is also derived so that the maximum possible level of degradation can be analytically determined for a given I/Q imbalance condition. Hence, the contributions of this chapter are threefold. Firstly, it provides an analytical means to investigate

the impacts of the I/Q imbalance on the performance of the ALMS loop. Secondly, it proves the robustness of the ALMS loop as an effective SIC architecture against practical imperfections. Finally, it derives a closed-form DF upper bound which is critical from the system design perspective. This upper bound provides a reference for evaluating the SIC performance in the RF domain and also determining how much compensation should be gained from other SIC stages such as propagation domain suppression and digital domain cancellation to satisfy the overall SIC requirement.

The rest of this chapter is organized as follows. In Section 5.2, the system architecture and the signal models are described. Then, the effects of I/Q imbalance on the loop gain and cancellation performance are investigated in Section 5.3. In Section 5.4, theoretical findings are verified by simulation results. Finally, conclusions are drawn in Section 5.5.

5.2 System Architecture and Signal Models

5.2.1 In-Band Full-Duplex Transceiver with ALMS Loop

Consider an FD transceiver terminal whose RF part is illustrated in Fig. 5.1. Owing to the FD operation, the received signal $r(t)$ is contaminated by a strong SI signal emitted from the local transmitter. In order to mitigate this SI, an ALMS loop is employed to generate a cancellation signal $y(t)$ and subtract it from the received signal at the input of the receiver. The ALMS loop, which comprises L taps, processes complex signals using I/Q structures. At the l-th tap, the looped-back signal is multiplied with the delayed transmitted signal using an I/Q demodulator. LPFs at the output of the demodulator act as integrators to synthesize the weighting coefficients $w_l(t), l = 0, 1, \ldots, L-1$. These weighting coefficients then modulate the same delayed transmitted signal at the modulator. The cancellation signal $y(t)$ is generated by combining the outputs of all the taps. After subtracting the reference signal from the received signal $r(t)$, the residual signal is amplified by the LNA and looped-back to the input of every tap.

Signal models are expressed as follows. The RF transmitted signal $x(t)$ is expressed as $x(t) = \mathrm{Re}\{X(t)e^{j2\pi f_c t}\}$, where f_c is the carrier frequency; $X(t)$ is the low-pass equivalent. Assuming that the baseband part of this FD transceiver can operate in either single-carrier or multi-carrier such as OFDM modes. Therefore, $X(t)$ is denoted as $X(t) = X_s(t)$ and $X(t) = X_o(t)$ in the single-carrier and OFDM modes, respectively. $X_s(t)$ and $X_o(t)$ are

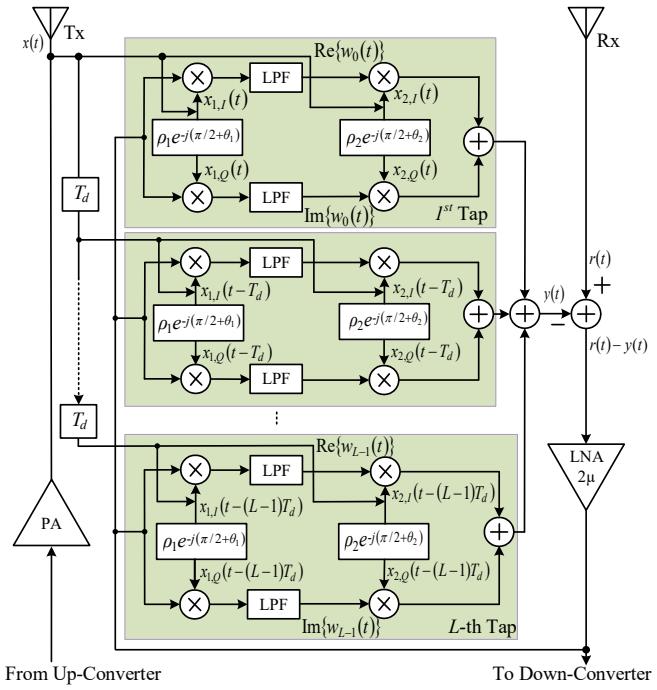

Figure 5.1: The ALMS loop structure.

modeled as

$$X_s(t) = \sum_{i=-\infty}^{\infty} a_i q(t - iT_s) \tag{5.1}$$

and

$$X_o(t) = \sum_{n=-\infty}^{\infty} \sum_{m=-\infty}^{\infty} \sum_{k=-N_{st}/2, k\neq 0}^{N_{st}/2} a_{k,m} e^{j2\pi \frac{k}{N}(n - m\frac{T_o}{T_s})} w\left[n - m\frac{T_o}{T_s}\right] q(t - nT_s) \tag{5.2}$$

respectively, where a_i, and $a_{k,m}$ are the i-th data symbol in the single-carrier system and the data symbol on the k-th sub-carrier of the m-th OFDM symbol respectively; T_s is the symbol period of the single-carrier system and also the sample period of the OFDM system; T_o is the OFDM symbol duration; N_{st} is the total number of data sub-carriers; N is the number of samples in one OFDM symbol excluding cyclic prefix; $w[n]$ is the discrete windowing function applied to an OFDM symbol; and $q(t)$ is the pulse shaping function. The complex data symbols a_i and $a_{k,m}$ are assumed to be independent to each other in both single-carrier and OFDM systems, i.e.,

$$E\{a_i^* a_{i'}\} = \begin{cases} 1, \text{ for } i = i' \\ 0, \text{ for } i \neq i' \end{cases}$$

and

$$E\{a^*_{k,m}a_{k',m'}\} = \begin{cases} 1, & \text{for } k = k', m = m' \\ 0, & \text{for } k \neq k', m \neq m'. \end{cases}$$

where $E\{.\}$ stands for ensemble expectation. The root mean square amplitude of the transmitted signal is defined as $V_X = \sqrt{\frac{1}{T}\int_0^T E\{|X(t)|^2\}dt}$ where T is the period of transmitted data symbol, i.e., T_s or T_o.

At the input of the receiver, the received signal $r(t)$ is a combination of the SI $z(t)$, the signal of interest $s(t)$, and the additive white Gaussian noise (AWGN) $n(t)$, i.e.,

$$r(t) = z(t) + s(t) + n(t) = \mathrm{Re}\Big\{\Big[Z(t) + S(t) + N(t)\Big]e^{j2\pi f_c t}\Big\}$$

where $Z(t)$, $S(t)$ and $N(t)$ are the low-pass equivalents of these signals respectively. For the ease of derivation, the SI channel is modeled as an L tapped delay line filter with tap delay T_d as in the ALMS loop, i.e.,

$$Z(t) = \sum_{l=0}^{L-1} h^*_l X(t - lT_d) \tag{5.3}$$

where $h^*_l, l = 0, 1, \ldots L-1$, are the SI channel coefficients.

5.2.2 I/Q Imbalanced Signal Models

It can be seen from the architecture that the ALMS loop processes the complex signals directly in the analog domain and hence the quadrature demodulators and modulators are required in the loop. Assuming that the I/Q imbalances of the demodulators and modulators are frequency-independent, and hence the phase shifters in the demodulators and modulators have constant amplitudes ρ_1 and ρ_2 as well as phase errors θ_1 and θ_2, respectively. Note that the microstrip traces in the two branches of each tap are also assumed to have the same length so that the phase shift caused by the signal traces is negligible or can be absorbed into the phase errors θ_1 and θ_2. Considering the demodulator of the first tap, the complex transmitted signal, denoted as $x_1(t)$ and presented at the demodulator, can be modeled as $x_1(t) = x_{1,I}(t) + jx_{1,Q}(t)$ where $x_{1,I}(t)$ and $x_{1,Q}(t)$ are the real transmitted signals at the I-branch and Q-branch respectively, and expressed as

$$\begin{aligned} x_{1,I}(t) &= \mathrm{Re}\{X(t)e^{j2\pi f_c t}\} = \frac{1}{2}\big[X(t)e^{j2\pi f_c t} + X^*(t)e^{-j2\pi f_c t}\big] \\ x_{1,Q}(t) &= \mathrm{Re}\{\rho_1 X(t)e^{j(2\pi f_c t - \pi/2 - \theta_1)}\} = \mathrm{Im}\{\rho_1 X(t)e^{j(2\pi f_c t - \theta_1)}\} \\ &= \frac{1}{2j}\big[\rho_1 X(t)e^{j(2\pi f_c t - \theta_1)} - \rho_1 X^*(t)e^{-j(2\pi f_c t - \theta_1)}\big]. \end{aligned} \tag{5.4}$$

Hence, the complex signal $x_1(t)$ is represented, in terms of the baseband equivalent $X(t)$, as

$$\begin{aligned} x_1(t) &= x_{1,I}(t) + jx_{1,Q}(t) \\ &= \frac{1+\rho_1 e^{-j\theta_1}}{2} X(t) e^{j2\pi f_c t} + \frac{1-\rho_1 e^{j\theta_1}}{2} X^*(t) e^{-j2\pi f_c t}. \end{aligned} \tag{5.5}$$

At the $l-$th tap, the product of $x_1(t-lT_d)$ and the looped-back signal is filtered by the LPF to attain the weighting coefficient, denoted as $w_l(t)$, which can be derived as [9, 67]

$$w_l(t+t_0) = \frac{2\mu\alpha}{K_1 K_2} \int_{t_0}^{t+t_0} e^{-\alpha(t+t_0-\tau)} [r(\tau) - y(\tau)] x_1(\tau - lT_d) d\tau \tag{5.6}$$

where K_1 and K_2 are the dimensional constants of the multipliers in the demodulator and modulator respectively, 2μ is the gain of the LNA, $\alpha = 1/RC$ is the decay constant of the resistor-capacitor LPF with resistance R and capacitance C, and $0 \le t_0 < T$ is an initial starting time. Similarly, the complex signal $x_2(t)$, presented in the modulator, can be expressed as

$$x_2(t) = \frac{1+\rho_2 e^{-j\theta_2}}{2} X(t) e^{j2\pi f_c t} + \frac{1-\rho_2 e^{j\theta_2}}{2} X^*(t) e^{-j2\pi f_c t}. \tag{5.7}$$

Hence, the cancellation signal $y(t)$ at the output of the ALMS loop can be expressed as

$$y(t) = \mathrm{Re}\Big\{ \sum_{l=0}^{L-1} w_l^*(t) x_2(t - lT_d) \Big\}. \tag{5.8}$$

For simplicity, denoting $\eta_i = \frac{1+\rho_i e^{-j\theta_i}}{2}$ and $\xi_i = \frac{1-\rho_i e^{j\theta_i}}{2}$, for $i = 1, 2$. From (5.6) and (5.7), $y(t)$ can be further expressed as

$$y(t) = \mathrm{Re}\Big\{ \sum_{l=0}^{L-1} w_l^*(t) \Big[\eta_2 X(t - lT_d) e^{j2\pi f_c (t - lT_d)} + \xi_2 X^*(t - lT_d) e^{-j2\pi f_c (t - lT_d)} \Big] \Big\}. \tag{5.9}$$

Clearly, the cancellation signal is affected by the I/Q imbalances at both modulators and demodulators.

5.3 Effects of I/Q Imbalance

5.3.1 Impact on Loop Gain

It has been proved in [9, 58, 59] that the loop gain, which is jointly determined by the LNA gain, the transmitted signal amplitude and the dimensional constants of the

multipliers in the modulator and demodulator, plays a vital role in the performance of the ALMS loop. The loop gain G is defined as

$$G = \frac{V_y}{V_d} \tag{5.10}$$

where V_y and V_d are the RMS voltages of the cancellation signal at the output and the residual SI signal at the input of the ALMS loop (before the LNA), respectively. From the loop architecture, when no I/Q imbalance presents, the loop gain G is calculated as

$$G = \frac{V_y}{V_d} = \frac{\frac{2\mu V_d V_x}{K_1}\frac{V_x}{K_2}}{V_d} = \frac{2\mu V_x^2}{K_1 K_2} \tag{5.11}$$

where V_x is the RMS voltage of the RF signal $x(t)$.

Since the I/Q imbalance causes the errors in phase and amplitude of the signals, it also impacts the total loop gain. The loop gain in the case of the I/Q imbalance, denoted as G', can be calculated as

$$G' = \frac{V_y}{V_d} = \frac{\frac{2\mu V_d V_{x_1}}{K_1}\frac{V_{x_2}}{K_2}}{V_d} = \frac{2\mu V_{x_1} V_{x_2}}{K_1 K_2} \tag{5.12}$$

where V_{x_1} and V_{x_2} are the RMS voltages of the I/Q imbalanced RF transmitted signals at the demodulator and modulator, respectively. The signal powers P_x and P_{x_i}(for $i = 1,2$) are derived as

$$\begin{aligned}
P_x &= V_x^2 = \frac{1}{T}\int_0^T E\{x^2(t)\}dt = \frac{1}{2T}\int_0^T E\left\{|X(t)|^2\right\}dt \\
P_{x_i} &= V_{x_i}^2 = \frac{1}{2T}\int_0^T E\left\{\left|\eta_i X(t)e^{j2\pi f_c t} + \xi_i X^*(t)e^{-j2\pi f_c t}\right|^2\right\}dt \\
&= \frac{1}{2T}\int_0^T E\left\{\left[\eta_i X(t)e^{j2\pi f_c t} + \xi_i X^*(t)e^{-j2\pi f_c t}\right]\left[\eta_i^* X^*(t)e^{-j2\pi f_c t} + \xi_i^* X(t)e^{j2\pi f_c t}\right]\right\}dt \\
&= \frac{1}{2T}\int_0^T E\left\{(|\eta_i|^2 + |\xi_i|^2)|X(t)|^2 + 2\mathrm{Re}\left\{\eta_i \xi_i^* X^2(t)e^{j4\pi f_c t}\right\}\right\}dt.
\end{aligned} \tag{5.13}$$

Since $E\{X^2(t)\} = 0$ for any zero mean complex random process $X(t)$, we have

$$\begin{aligned}
P_{x_i} &= \frac{(|\eta_i|^2 + |\xi_i|^2)}{2T}\int_0^T E\left\{|X(t)|^2\right\}dt \\
&= (|\eta_i|^2 + |\xi_i|^2)P_x.
\end{aligned} \tag{5.14}$$

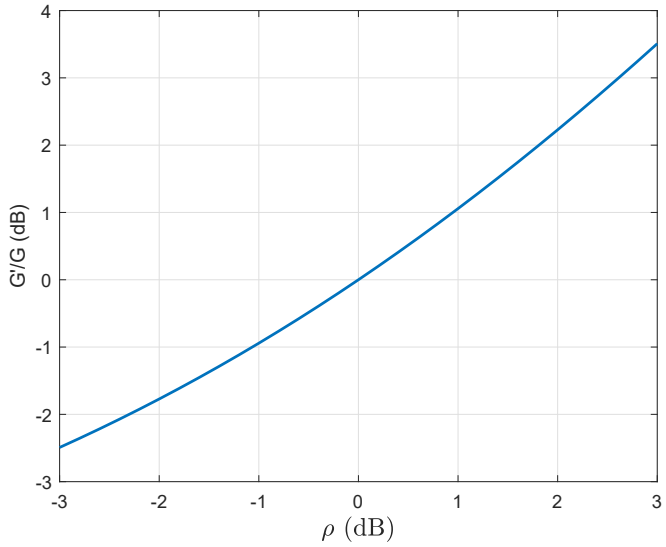

Figure 5.2: The loop gain ratio versus amplitude.

Therefore, the effect of I/Q imbalance on the loop gain can be represented by

$$\begin{aligned} G' &= \sqrt{(|\eta_1|^2 + |\xi_1|^2)(|\eta_2|^2 + |\xi_2|^2)}\,G \\ &= \frac{1}{2}\sqrt{(1+\rho_1^2)(1+\rho_2^2)}\,G. \end{aligned} \tag{5.15}$$

It is seen that the change on the loop gain is a function of the amplitudes of the phase shifters in the demodulators and the modulators only. Assuming that the phase shifters in the demodulators and modulators have the same amplitudes, i.e., $\rho_1 = \rho_2 = \rho$, the ratio $G'/G = \frac{1+\rho^2}{2}$ over a range of ρ is presented in Fig. 5.2. From this figure, the amplitude errors may contribute to the loop gain ($\rho > 0$ dB) or reduce the loop gain ($\rho < 0$ dB). The variation of the loop gain can be compensated accordingly by changing the gain at other stages in the loop such as the LNA.

5.3.2 Impact on Cancellation Performance

In this section, the impact of I/Q imbalance on the cancellation performance of the ALMS loop is investigated. In order to analyze the impact of I/Q imbalance under the same loop gain, the gain of the LNA 2μ can be scaled to $2\mu'$ with $\mu' = \frac{2\mu}{\sqrt{(1+\rho_1^2)(1+\rho_2^2)}}$. The following derivation will be conducted with this adjustment of the LNA gain. The residual SI power in case of the ALMS loop with I/Q imbalance is compared to that in the perfect case of no I/Q imbalance. In this analysis, the ALMS loop is considered in the steady state, i.e., all the weighting coefficients are converged to their stable values. Therefore,

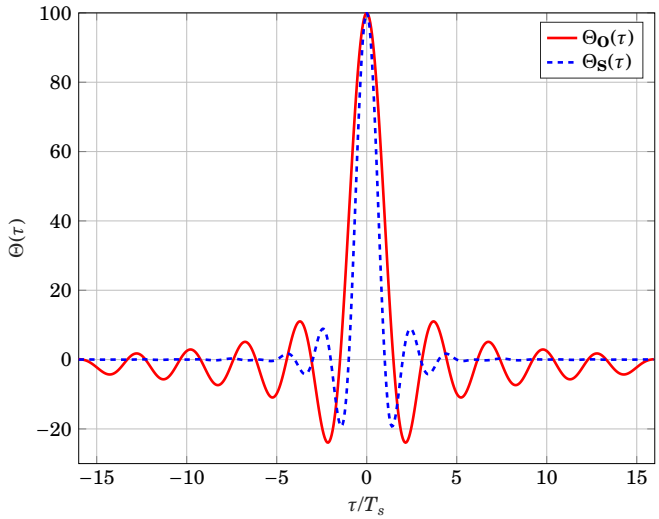

Figure 5.3: The normalized autocorrelation function of the transmitted signals.

both ensemble expectation and time averaging, denoted as $\bar{E}\{.\}$, are applied to evaluate all the processes. The normalized autocorrelation functions of the transmitted signal, denoted as $\Phi(\tau)$, is defined as

$$\begin{aligned}\Phi(\tau) &= \frac{1}{K_1 K_2}\bar{E}\{X^*(t)X(t-\tau)\} \\ &= \frac{1}{K_1 K_2 T}\int_0^T E\{X^*(t)X(t-\tau)\}dt.\end{aligned} \tag{5.16}$$

Denoting $A^2 = V_X^2/K_1K_2$, $\Phi(0) = \frac{1}{K_1K_2T}\int_0^T E\{|X(t)|^2\}dt = A^2$, which is the normalized power of the transmitted signal. Fig. 5.3 demonstrates the normalized autocorrelation functions of the single-carrier signal $\Phi_S(\tau)$ and OFDM signal $\Phi_O(\tau)$ with $A^2 = 100$. In this plot, $q(t)$ is a root-raised cosine (RRC) function in the single-carrier case and raised cosine (RC) function for the OFDM case. The windowing function for the OFDM signal is the one recommended in IEEE 802.11a. All pulse shaping filters and windowing function have the roll-off factor $\beta = 0.25$.

Defining the residual SI signal as $d(t) = z(t) - y(t)$, using the signal models in (5.3)

and (5.8), and denoting $u_l(t) = h_l - (\eta_2^* w_l(t) + \xi_2 w_l^*(t))e^{j2\pi f_c l T_d}$, $d(t)$ can be expressed as

$$\begin{aligned} d(t) = z(t) - y(t) &= \mathrm{Re}\Big\{ \sum_{l=0}^{L-1} h_l^* X(t - lT_d) e^{j2\pi f_c t} \Big\} \\ &- \mathrm{Re}\Big\{ \sum_{l=0}^{L-1} w_l^*(t) \Big[\eta_2 X(t - lT_d) e^{j2\pi f_c (t - lT_d)} + \xi_2 X^*(t - lT_d) e^{-j2\pi f_c (t - lT_d)} \Big] \Big\} \\ &= \frac{1}{2} \Big[\sum_{l=0}^{L-1} u_l^*(t) X(t - lT_d) e^{j2\pi f_c t} + \sum_{l=0}^{L-1} u_l(t) X^*(t - lT_d) e^{-j2\pi f_c t} \Big] \\ &= \mathrm{Re}\Big\{ \sum_{l=0}^{L-1} u_l^*(t) X(t - lT_d) e^{j2\pi f_c t} \Big\}. \end{aligned} \tag{5.17}$$

It means that the residual SI of the ALMS loop is determined by the weighting error function $u_l(t)$. The normalized residual SI power, denoted as $P_d(t)$, can be determined as

$$P_d(t) = \frac{1}{K_1 K_2} \bar{E}\{|d(t)|^2\}. \tag{5.18}$$

Substituting (5.17) into (5.18), after some manipulations (see Appendix A.3) and let $t \to \infty$, $P_d(t)$ converges to its steady-state

$$P_d = \frac{1}{2} \bar{\bar{\mathbf{u}}}^H \mathbf{\Phi} \bar{\bar{\mathbf{u}}} \tag{5.19}$$

where

$$\mathbf{\Phi} = \begin{bmatrix} \Phi(0) & \Phi(-T_d) & \cdots & \Phi(-(L-1)T_d) \\ \Phi(T_d) & \Phi(0) & \cdots & \Phi(-(L-2)T_d) \\ \vdots & \vdots & \ddots & \vdots \\ \Phi((L-1)T_d) & \Phi((L-2)T_d) & \cdots & \Phi(0) \end{bmatrix}$$ is the $L \times L$ autocorrelation matrix

and $\bar{\bar{\mathbf{u}}} = [\bar{\bar{u}}_0 \ldots \bar{\bar{u}}_{L-1}]^T$ is the vector of the steady-state weighting error functions. From the solution of the weighting error function (see Appendix A.4), $\bar{\bar{\mathbf{u}}}$ is expressed as

$$\bar{\bar{\mathbf{u}}} = \Big[(\mathbf{I}_L + k_1 \mathbf{\Phi}) - |k_2|^2 \mathbf{E} \mathbf{\Phi} (\mathbf{I}_L + k_1^* \mathbf{\Phi})^{-1} \mathbf{E}^{-1} \mathbf{\Phi} \Big]^{-1} \Big[\mathbf{h} - k_2 \mathbf{E} \mathbf{\Phi} (\mathbf{I}_L + k_1^* \mathbf{\Phi})^{-1} \mathbf{h}^* \Big] \tag{5.20}$$

where $\mathbf{I}_L$ is the identity matrix of order L; $k_1 = \mu' \big(\eta_1 \eta_2^* + \xi_1^* \xi_2 \big)$, and $k_2 = \mu' \big(\eta_2^* \xi_1 + \eta_1^* \xi_2 \big)$ are constants representing the I/Q imbalance errors; $\mathbf{E} = \begin{bmatrix} 1 & 0 & \cdots & 0 \\ 0 & e^{j4\pi f_c T_d} & \cdots & 0 \\ \vdots & \vdots & \ddots & \vdots \\ 0 & \cdots & 0 & e^{j4\pi f_c (L-1) T_d} \end{bmatrix}$;

and $\mathbf{h} = [h_0 \; h_1 \ldots h_{L-1}]^T$ is the channel coefficients of L paths.

When there is no I/Q imbalance, i.e., $\rho_1 = \rho_2 = 1, \theta_1 = \theta_2 = 0$, thus $k_1 = \mu, k_2 = 0$, we have $\bar{\tilde{\mathbf{u}}} = (\mathbf{I}_L + \mu\mathbf{\Phi})^{-1}\mathbf{h}$. Note that the autocorrelation matrix can be decomposed as $\mathbf{\Phi} = \mathbf{Q}\mathbf{\Lambda}\mathbf{Q}^{-1}$ where $\mathbf{Q}$ is the orthonormal modal matrix whose columns are the L eigenvectors of $\mathbf{\Phi}$ and $\mathbf{\Lambda} = \begin{pmatrix} \lambda_0 & 0 & \cdots & 0 \\ 0 & \lambda_1 & \cdots & 0 \\ \vdots & \vdots & \ddots & \vdots \\ 0 & 0 & \cdots & \lambda_{L-1} \end{pmatrix}$ is a diagonal spectral matrix, and $\lambda_l, l = 0, \ldots, L-1$, are L eigenvalues of $\mathbf{\Phi}$. In this case, the residual SI is calculated as

$$\begin{aligned} P_0 &= \frac{1}{2}\mathbf{h}^H(\mathbf{I}_L + \mu\mathbf{\Phi})^{-1}\mathbf{\Phi}(\mathbf{I}_L + \mu\mathbf{\Phi})^{-1}\mathbf{h} \\ &= \frac{1}{2}\mathbf{h}^H\mathbf{Q}(\mathbf{I}_L + \mu\mathbf{\Lambda})^{-1}\mathbf{Q}^{-1}\mathbf{Q}\mathbf{\Lambda}\mathbf{Q}^{-1}(\mathbf{I}_L + \mu\mathbf{\Lambda})^{-1}\mathbf{Q}^{-1}\mathbf{h} \\ &= \frac{1}{2}\mathbf{h}^H\mathbf{Q}\text{diag}\Big\{\frac{\lambda_l}{(1+\mu\lambda_l)^2}\Big\}\mathbf{Q}^{-1}\mathbf{h} \end{aligned} \tag{5.21}$$

where $\text{diag}\{\frac{\lambda_l}{(1+\mu\lambda_l)^2}\}, l = 1, \ldots, L$, is an $L \times L$ diagonal matrix whose main diagonal elements are $\frac{\lambda_1}{(1+\mu\lambda_1)^2}, \ldots, \frac{\lambda_L}{(1+\mu\lambda_L)^2}$. It is seen that P_0 is the same as the result derived in [9, Eq. (37)]. From (5.19) and (5.21), when there are I/Q imbalances present, we will see that I/Q imbalances of the modulators and demodulators not only lead to the change of the residual SI power, but also result in the involvement of the carrier frequency in the performance of the ALMS loop.

To quantify the impact of I/Q imbalance on the level of cancellation, the degradation factor DF is defined as

$$\begin{aligned} DF &= 10\log_{10}\frac{P_d}{P_0} \\ &= 10\log_{10}\frac{\bar{\tilde{\mathbf{u}}}^H\mathbf{\Phi}\bar{\tilde{\mathbf{u}}}}{\mathbf{h}^H\mathbf{Q}\text{diag}\Big\{\frac{\lambda_l}{(1+\mu\lambda_l)^2}\Big\}\mathbf{Q}^{-1}\mathbf{h}}. \end{aligned} \tag{5.22}$$

From (5.20) and (5.22), in addition to the I/Q imbalance, the DF is also related to other factors such as the SI channel $\mathbf{h}$, the transmitted signal properties (shown in $\mathbf{\Phi}$), and the carrier frequency of the transmitted signal (shown in the matrix $\mathbf{E}$). Therefore, two questions can be raised at this point. First, *what is the DF on average over many realizations of the SI channel*? Second, *what is the possible maximum level of the DF*? The latter is very important as it provides an analytical upper bound useful for the system design. These two questions are addressed as follows.

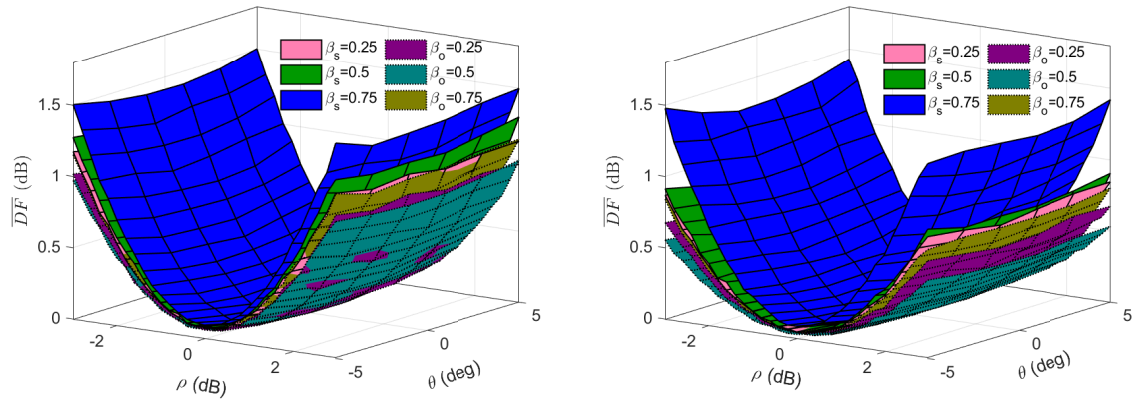

(a) (b)

Figure 5.4: $\overline{DF}$ versus amplitude and phase errors with different β for $L = 8$ and (a) $f_c = 2432$ MHz and (b) $f_c = 5200$ MHz.

5.3.2.1 Averaged Degradation Factor

To evaluate the overall impact of the SI channel in the DF, defining an averaged degradation factor $\overline{DF}$ as

$$\overline{DF} = 10\log_{10}\frac{E_h\{P_d\}}{E_h\{P_0\}} \tag{5.23}$$

where $E_h\{.\}$ stands for expectation over the SI channel.

Assuming that proper propagation domain suppression has been performed so that the SI mainly comes from multi-path reflections. All the coefficients of the SI channel which includes L propagation paths are independent and Gaussian distributed with a zero mean. An exponential distribution is chosen for the power delay profile of the channel. Its root mean square delay spread is selected as $\sigma = LT_s/4$. The transmitter has symbol duration $T_s = 20$ ns. The ALMS loop has the tap delay $T_d = T_s/2$. When operating in the multi-carrier mode, the parameters of the transmitted OFDM signal are selected following the IEE802.11a standard. For simplicity, assuming that the phase shifters in the modulators and demodulators have the same degree of imperfections, i.e., $\rho_1 = \rho_2 = \rho$ and $\theta_1 = \theta_2 = \theta$. Fig. 5.4 and Fig. 5.5 present $\overline{DF}$ obtained by averaging over 10000 realizations of the SI channel over a range of the amplitude (-3 dB $\le \rho \le 3$ dB) and phase error ($-5^\circ \le \theta \le 5^\circ$) for the systems with carrier frequencies of 2432 MHz and 5200 MHz, respectively. These two carrier frequencies are chosen as examples because they are common worldwide IEEE 802.11 frequency bands. In Fig. 5.4, β_s and β_o stand for the roll-off factors of the pulse shaping filter and the windowing function in the

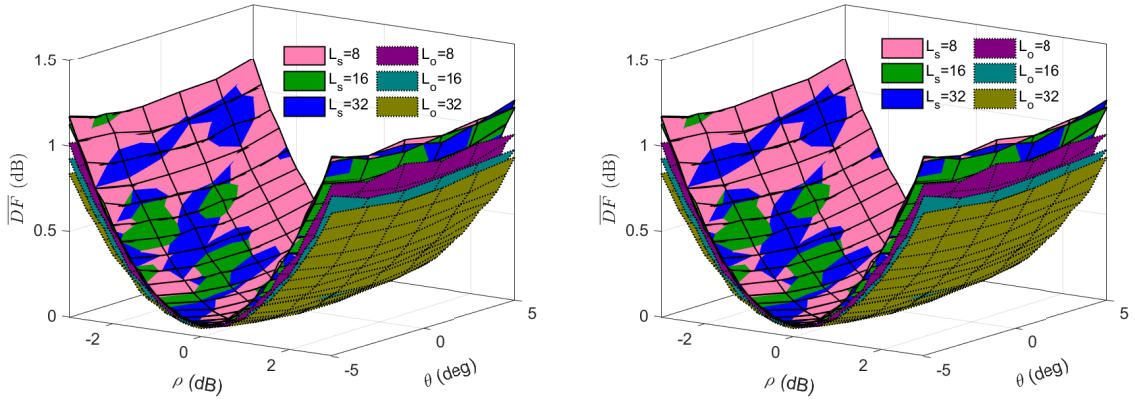

(a) (b)

Figure 5.5: $\overline{DF}$ versus amplitude and phase errors with different L for $\beta = 0.25$ and (a) $f_c = 2432$ MHz and (b) $f_c = 5200$ MHz.

single-carrier and OFDM basebands, respectively. In Fig. 5.5, all the roll-off factors are fixed at $\beta = 0.25$ and $\overline{DF}$ is calculated for different number of taps L in the ALMS loop.

From these figures, some observations are drawn as follows.

1. $\overline{DF}$ is more impacted by the amplitudes than the phase errors. It is seen that $\overline{DF}$ is almost stable over the whole range of θ for a given value of ρ.

2. When $\theta = 0$ and $\rho = 1$, $\overline{DF} = 0$ dB, i.e., there is no I/Q imbalance.

3. Signal properties (β and f_c) have more influence on $\overline{DF}$ than the number of taps in the loop.

4. $\overline{DF}$ does not exceed 1.5 dB for most of the cases. It is slightly greater than 1.5 dB when $\beta_s \geq 0.75$. However, these conditions unlikely happen in practice.

It can be concluded that, considering the average effect of the SI channel, the ALMS loop is resilient to its frequency-independent I/Q imbalance. This resilience can be explained as follows. The ALMS loop is designed to minimize the level of the residual SI power. The adaptive adjustment of the weighting coefficients ensures that the ALMS loop always works at its optimized condition. Therefore, the impact of the I/Q imbalance occurred in the ALMS loop on the SIC performance is not serious as that of the I/Q imbalance occurred in the signal transmission path on the information detection performance.

5.3.2.2 Upper Bound of Degradation Factor

From the system design perspective, it is essential to estimate the level of degradation of SIC given by the ALMS loop under a given condition of I/Q imbalance. This degradation of SIC in the RF domain can be compensated at other stages such as propagation domain attenuation or digital domain cancellation. Therefore, the upper bound of the degradation factor, denoted as DF_u, is derived as follows.

In the ideal case when the roll-off factor of the pulse shaping filter is zero, the tap delay T_d can be chosen as $T_d = T_s$. In this case, the autocorrelation matrix $\mathbf{\Phi}$ is a diagonal matrix and all of its eigenvalues are equal, i.e., $\lambda_0 = \lambda_1 = \cdots = \lambda_{L-1} = \bar{\lambda} = A^2$. Therefore, from (5.20), the weighting error functions $\bar{\bar{\mathbf{u}}}$ becomes

$$\begin{aligned}\bar{\bar{\mathbf{u}}} &= \Big[(\mathbf{I}_L + k_1\mathbf{\Phi}) - |k_2|^2\mathbf{E}\mathbf{\Phi}(\mathbf{I}_L + k_1^*\mathbf{\Phi})^{-1}\mathbf{E}^{-1}\mathbf{\Phi}\Big]^{-1}\Big[\mathbf{h} - k_2\mathbf{E}\mathbf{\Phi}(\mathbf{I}_L + k_1^*\mathbf{\Phi})^{-1}\mathbf{h}^*\Big] \\ &= \Big[(1+k_1A^2) - \frac{|k_2|^2A^4}{1+k_1^*A^2}\Big]^{-1}\Big[\mathbf{h} - \frac{k_2A^2}{1+k_1^*A^2}\mathbf{E}\mathbf{h}^*\Big] \\ &= \kappa\Big[(1+k_1^*A^2)\mathbf{h} - k_2A^2\mathbf{E}\mathbf{h}^*\Big]\end{aligned} \tag{5.24}$$

where $\kappa = \Big[1 + 2\mathrm{Re}\{k_1\}A^2 + (|k_1|^2 - |k_2|^2)A^4\Big]^{-1}$. Substituting (5.24) into (5.19), we have

$$\begin{aligned}P_d &= \frac{1}{2}\kappa^2A^2\Big[(1+k_1A^2)\mathbf{h}^H - k_2^*A^2\mathbf{h}^T\mathbf{E}^{-1}\Big]\Big[(1+k_1^*A^2)\mathbf{h} - k_2A^2\mathbf{E}\mathbf{h}^*\Big] \\ &= \frac{1}{2}\kappa^2A^2\Big[(1 + 2\mathrm{Re}\{k_1\}A^2 + (|k_1|^2 + |k_2|^2)A^4)\sum_{l=0}^{L-1}|h_l|^2 \\ &\quad - 2\Big\{\big|k_2^*A^2(1+k_1^*A^2)\big|\sum_{l=0}^{L-1}|h_l|^2\cos(-4\pi f_c l T_d + 2\phi_{h_l} + \phi_k)\Big\}\Big]\end{aligned} \tag{5.25}$$

where ϕ_{h_l} and ϕ_k are the phases of the SI channel coefficient h_l and the complex number $k_2^*A^2(1+k_1^*A^2)$, respectively. Since $-1 \le \cos(x) \le 1$ for any angle x and $\mathrm{Re}\{z\} \le |z|$ for any complex number z, we have the upper bound of the residual SI power as

$$\begin{aligned}P_d &\le \frac{1}{2}\kappa^2A^2\Big[(1 + 2\mathrm{Re}\{k_1\}A^2 + (|k_1|^2 + |k_2|^2)A^4)\sum_{l=0}^{L-1}|h_l|^2 + 2\Big\{\big|k_2^*A^2(1+k_1^*A^2)\big|\sum_{l=0}^{L-1}|h_l|^2\Big\}\Big] \\ &\le \frac{1}{2}\kappa^2A^2\Big[1 + 2(|k_1| + |k_2|)A^2 + (|k_1|^2 + 2|k_1k_2| + |k_2|^2)A^4\Big]\sum_{l=0}^{L-1}|h_l|^2 \\ &= \frac{1}{2}\kappa^2A^2[1 + (|k_1| + |k_2|)A^2]^2\sum_{l=0}^{L-1}|h_l|^2.\end{aligned} \tag{5.26}$$

Under the same condition, P_0 is found to be $P_0 = \frac{A^2}{2(1+\mu A^2)^2}\sum_{l=0}^{L-1}|h_l|^2$. Therefore, DF_u can be found as

$$\begin{aligned} DF_u &= 10\log_{10}\frac{\frac{1}{2}\kappa^2 A^2\left[1+(|k_1|+|k_2|)A^2\right]^2\sum_{l=0}^{L-1}|h_l|^2}{\frac{A^2}{2(1+\mu A^2)^2}\sum_{l=0}^{L-1}|h_l|^2} \\ &= 10\log_{10}\frac{\left[1+(|k_1|+|k_2|)A^2\right]^2(1+\mu A^2)^2}{[1+2\mathrm{Re}\{k_1\}A^2+(|k_1|^2-|k_2|^2)A^4]^2}. \end{aligned} \tag{5.27}$$

Assuming that μA^2 is very large so that $1/\mu A^2 \approx 0$, and by dividing both numerator and denominator in (5.27) by $(\mu A^2)^4$, we have

$$DF_u = 10\log_{10}\frac{\frac{(|k_1|+|k_2|)^2}{\mu^2}}{(\frac{|k_1|^2-|k_2|^2}{\mu^2})^2}. \tag{5.28}$$

Let the phase shifters in the modulators and demodulators have the same degree of imperfections, i.e., $\rho_1 = \rho_2 = \rho$ and $\theta_1 = \theta_2 = \theta$. Substituting the definition of k_1, k_2 and $\mu' = 2\mu/(1+\rho^2)$ into (5.28), we have

$$\begin{aligned} DF_u &= 10\log_{10}\frac{\frac{\mu^2\left(1+\rho^2+\sqrt{1-2\rho^2\cos 2\theta+\rho^4}\right)^2}{(1+\rho^2)^2\mu^2}}{(\frac{\mu^2[(1+\rho^2)^2-(1-2\rho^2\cos 2\theta+\rho^4)]}{(1+\rho^2)^2\mu^2})^2} \\ &= 20\log_{10}\frac{(1+\rho^2)\left(1+\rho^2+\sqrt{1-2\rho^2\cos 2\theta+\rho^4}\right)}{4\rho^2\cos^2\theta}. \end{aligned} \tag{5.29}$$

Fig. 6 presents DF_u calculated from (5.29) as a function of ρ and θ. It is seen that DF is mainly determined by the amplitudes, while it is almost the same over the range of phase errors. Hence, when selecting the modulators and demodulators for the ALMS loop, it is better to choose those with small amplitude errors. In addition, in the worst scenarios when $\rho = \pm 3$ dB, DF_u is about 3.5 dB only. This 3.5 dB deterioration of SIC can be compensated at other stages such as propagation domain suppression and digital domain cancellation.

5.4 Simulation Results

In this section, simulations are performed to justify the theoretical results shown in Section 5.3. The FD system with configuration as in Fig. 5.1 is employed with QPSK modulation and $T_s = 20$ ns. When operating in the multi-carrier mode, the OFDM symbol of duration $T_o = 80T_s$ is generated from 64-point IFFT with cyclic prefix added. The

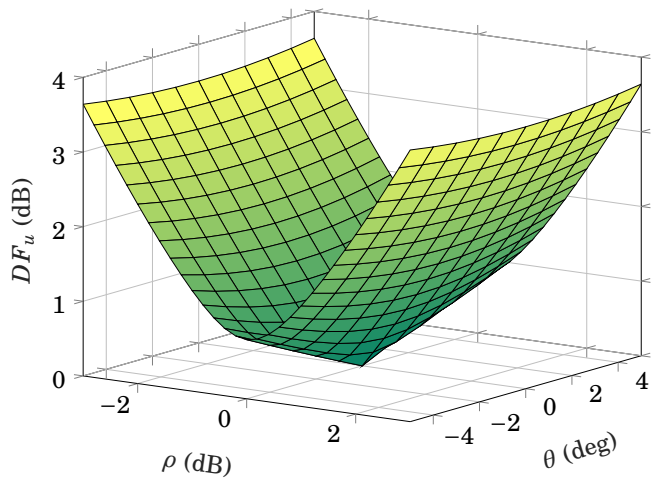

Figure 5.6: DF versus amplitude and phase errors when $\beta = 0$ and $T_d = T_s$.

OFDM symbols are then passed through the IEEE 802.11a windowing function and the RC pulse shaping filter before sending to the RF front-end. All the roll-off factors of the pulse shaping filter and windowing function are $\beta = 0.25$. The RF transmitted signal has power of 0 dBm over a 50 Ohm load or $0\text{dBm} + 10\log_{10}(50) = 17$ dBm over 1 Ohm load. Hence, the RMS voltage of the (baseband) transmitted signal for 1 Ohm load can be found as $V_X^2 = 2 \times 10^{(17-30)/10} = 0.1\ V^2$. The ALMS loop has 8 taps with the tap spacing $T_d = T_s/2$. The demodulators and modulators in all taps have the same multiplier constants which are selected as $K_1 K_2 = 0.001\ V^2$. Due to the separation of the transmit and receive antennas, the SI power at the input of the receiver is attenuated 25 dB compared to the transmitted signal power. The channel impulse response presented in [9, Fig. 10] is adopted in this Chapter for simulation. Accordingly, the SI channel includes three paths and is modeled as $h(t) = 10^{\frac{-25}{20}} \{[\frac{\sqrt{2}}{2} - 0.5j]\delta(t) - 0.4\delta(t - T_s) + 0.3\delta(t - 3T_s)\}$, i.e., the delays of reflected paths are multiples of T_s. The LNA in the receiver is designed so that its gain can be varied in order to compensate for the change of the total loop gain. In case of no I/Q imbalance, the LNA gain 2μ is selected as 26 dB, i.e., $\mu = 10$.

The modulators and demodulators in the ALMS loop are chosen such that their phase shifters have the same I/Q imbalance parameters as $\rho_1 = \rho_2 = \rho = 3$ dB, $\theta_1 = \theta_2 = \theta = 5^\circ$. Due to these imperfections, the OFDM transmitted signals presented at the modulators and demodulators are illustrated in Fig. 5.7. To compare the performance under the same loop gain, the LNA gain is adjusted to $\mu' = 2\mu/(1 + \rho^2) = 6.6772$ when I/Q imbalance present at the ALMS loop.

Fig. 5.8(a) and Fig. 5.9(b) show the simulated results (blue curves) in comparison

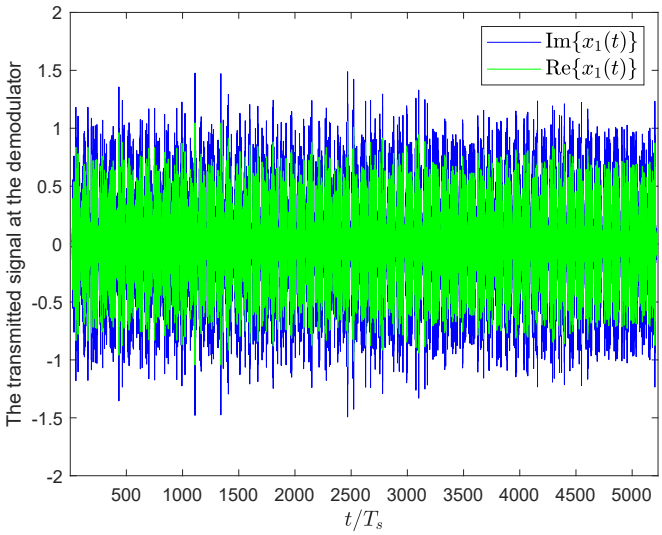

Figure 5.7: The complex signals $x_1(t)$ and $x_2(t)$ with $\rho_1 = \rho_2 = 3$ dB, $\theta_1 = \theta_2 = 5°$.

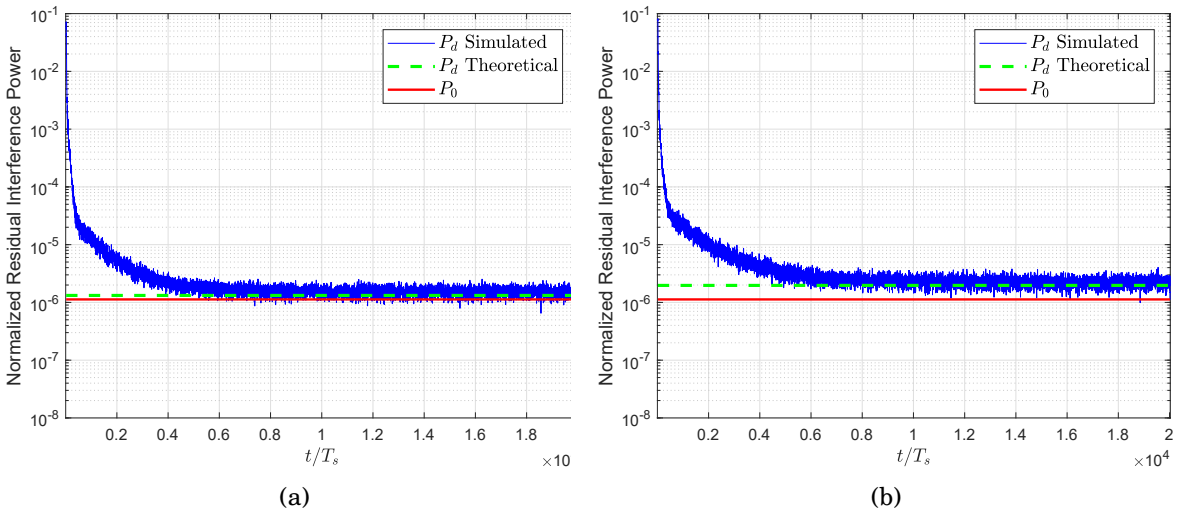

(a) (b)

Figure 5.8: Residual SI powers in single-carrier system with $\rho_1 = \rho_2 = 3$ dB, $\theta_1 = \theta_2 = 5°$ and (a) $f_c = 2432$ MHz and (b) and $f_c = 5200$ MHz.

to the theoretical results for carrier frequencies of $f_c = 2432$ MHz and $f_c = 5200$ MHz, respectively. The green-dashed line is the theoretical residual SI power (cf. (5.19)) for the case of the ALMS loop with I/Q imbalance. The red line is the residual SI power (cf. (5.21)) for the case of the ALMS loop under an I/Q imbalance-free condition. It can be seen from these figures that the convergence of the simulation results (blue curves) to the theoretical results (green-dashed lines) confirms the steady state analysis. In addition, the gaps between the green-dashed lines and the red lines in these figures show the

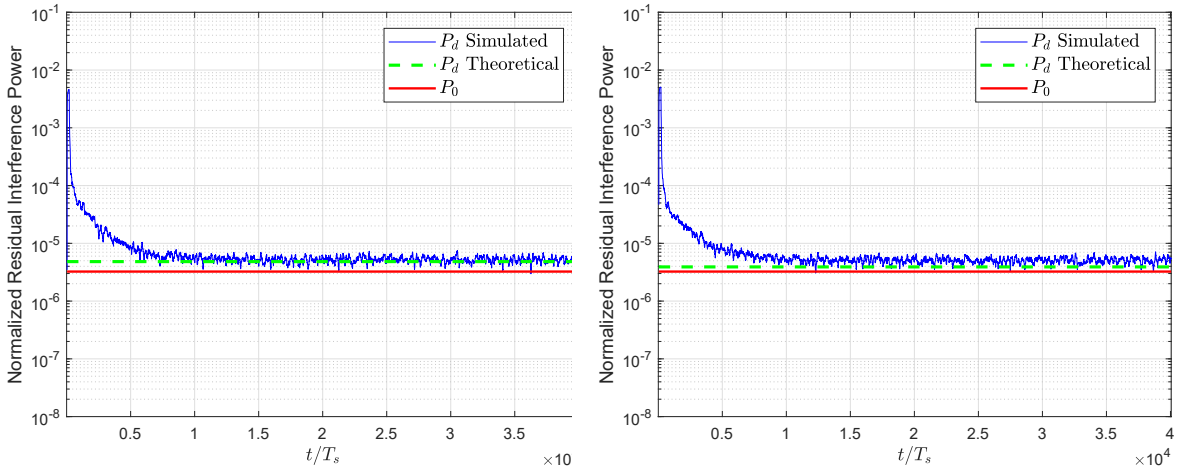

(a) (b)

Figure 5.9: Residual SI powers in OFDM system with $\rho_1 = \rho_2 = 3$ dB, $\theta_1 = \theta_2 = 5°$ and (a) $f_c = 2432$ MHz and (b) $f_c = 5200$ MHz.

DF of 0.6894 dB ($f_c = 2432$ MHz) and 2.426 dB ($f_c = 5200$ MHz) in the single-carrier case and 1.7242 dB ($f_c = 2432$ MHz) and 0.8067 dB ($f_c = 5200$ MHz) in the OFDM case, respectively for the given SI channel. Note that the difference in the levels of DFs in these cases does not show the trend of DF versus carrier frequency and transmitted signal properties, but they are calculated from (5.22) for a specific SI channel and carrier frequencies.

5.5 Conclusion

In this chapter, the effects of frequency-independent I/Q imbalances in the ALMS loop have been investigated. It is shown that I/Q imbalance leads to the loop gain variation and reduces the level of SIC provided by the ALMS loop. While the change in the loop gain can be simply compensated by adjusting the gain at other stages inside the loop, the degradation in the level of SIC is proved to be insignificant over numerous observations of the SI channels. The upper bound of this degradation is also derived so that the maximum level of deterioration can be estimated under a given degree of imperfections.

CHAPTER 6

ALMS LOOP FOR IN-BAND FULL-DUPLEX MIMO SYSTEMS

6.1 Introduction

The next generation wireless communication systems will leap forward the data transmission performance in many aspects such as higher data rate, lower round-trip latency, and less power consumption [68]. To achieve these objectives, many disruptive technologies have been developed, including IBFD and massive MIMO transmission [69, 70]. With IBFD operation, a transceiver can simultaneously transmit and receive signals in the same frequency band so that the throughput can be doubled compared to its half-duplex counterpart [71]. Massive MIMO is promising because it can support many users by using beamforming technique with increased spectral and energy efficiencies. Naturally, combining IBFD with massive MIMO can further improve spectral efficiency [72] and reduce the round-trip latency in networks requiring two-way relay channels [73].

However, it is very challenging to mitigate SI in IBFD MIMO systems due to the complexity of the SI channels. In particular, in an $N \times N$ antenna IBFD MIMO system, at each receive (Rx) chain, there are presented SIs caused by the cross-talks from N transmit (Tx) antennas. One advantage of MIMO systems is that beamforming techniques can be used to exploit spatial suppression in IBFD MIMO systems [23, 24, 74–77]. To further mitigate the level of SI, analog domain cancellation should be used. Among many

different approaches, a multi-tap canceller has been proved as a promising structure for SIC in IBFD single antenna systems [9, 39, 40, 78]. This is because the transmitted RF signal is utilized in this structure so that it can also mitigate the Tx noise and nonlinear distortions of the transmitter [10]. However, if a cancellation circuit is used for each pair of Tx and Rx antennas, an $N \times N$ antenna IBFD MIMO system will need N^2 cancellation circuits [78]. Therefore, some strategies of using analog cancellation circuits have been introduced in the literature to reduce the number of cancellers [45, 78–80]. However, the multi-tap structures used in these publications require channel state information (CSI) and digital signal processing (DSP) to synthesize the weighting coefficients in each tap. As a result, such IBFD MIMO has to operate in the half-duplex mode when estimating the SI channel. In addition, since the optimization depends on the cross-talk between each pair of co-located Tx and Rx antennas, the complexity of DSP algorithms increases quadratically with the size of IBFD MIMO systems [78]. The increase of DSP complexity results in larger digital hardware resources such as field programmable gate array (FPGA) and higher power consumption. As an example, DSP computations for 16 cancellation circuits in a 4×4 IBFD MIMO system will consume up to 80 W [78].

Unlike the multi-tap structures mentioned above, the ALMS loop presented in [9] is an adaptive filter without any DSP involvement. Instead, a simple Resistor-Capacitor (RC) LPF is utilized to synthesize the weighting coefficients for each tap. The behaviors of the ALMS loop in different IBFD single antenna systems have been presented in [9, 58, 59, 61, 67, 81]. Obviously, adopting the ALMS loop for SIC in IBFD MIMO systems can significantly reduce the complexity of DSP at RF front-end.

In this chapter, a beam-based SIC structure which employs ALMS loops as the adaptive filters for SI mitigation is proposed for IBFD massive MIMO systems. Since the transmitted signal power per antenna in IBFD massive MIMO systems is low, all Tx chains can be assumed to be linear. In this case, the SI at the receiver side can be considered as a linear combination of the transmitted beam signals for K users. As a result, instead of using N cancellers to cancel the SI from N Tx antennas for each receive antenna, only K adaptive filters are sufficient. Since $K \ll N$, the number of cancellation circuits is significantly reduced. The contributions of this chapter are summarized as follows.

- A mathematical model of the SI in IBFD beamforming MIMO systems is derived, which shows that the SI to each receive antenna is a linear combination of the transmitted beam signals. This model suggests that the reference signals can be the linear combinations of the beam signals rather than using all transmitted

signals.

- By employing the ALMS loop which does not require the CSI for tuning its weighting coefficients, the proposed structure can save significant FPGA resources and hence reduce energy consumption.

- The problem of generating the reference signals from transmitted beam data is comprehensively investigated. In particular, the reference signals can be generated by employing additional transmit chains. In this way, given that the all the adaptive filters in the proposed beam-based analog SIC structure have the same configuration of the ALMS loop, the ISR calculated across all the receiver chains is the same as that in the single antenna system. To further reduce the complexity of the proposed structure, a novel method is proposed to select the reference signals for the ALMS loops from available transmitted signals. The reference signal selection method not only reduces the hardware complexity, but also enhances the level of cancellation given by the ALMS loops.

The rest of this chapter is organized as follows. The proposed beam-based cancellation architecture for IBFD MIMO systems and signal models are described in Section 6.2. In Section 6.3, stationary analysis is presented to evaluate the performance of the proposed structure with the reference signals generated by additional transmit chains. Section 6.4 shows a method to select the reference signals from transmitted signals. Finally, conclusions are drawn in Section 6.5.

Notation: Boldface lowercase and boldface capital letters (e.g., $\mathbf{a}$ and $\mathbf{A}$) are used to indicate vectors and matrices, respectively. $\mathbf{A}^T$ and $\mathbf{A}^H$ denote the transpose and Hermitian transpose of $\mathbf{A}$, respectively, and $\otimes$ is the Kronecker product. $\text{diag}\{\lambda_i\}, i = 1,\cdots,MKL$, is used to denote an $M\times K\times L$ diagonal matrix whose main diagonal elements are $\lambda_1,\cdots,\lambda_{MKL}$. $\mathbf{I}_M$ represents the identity matrix of order M. $E\{.\}$ stands for the ensemble expectation operation, and $\mathbb{C}$ is the complex set.

6.2 Principle of Beam-Based Analog SIC

6.2.1 Beam-Based SIC

Consider an IBFD MIMO digital beamforming system with N Tx and M Rx antennas as shown in Fig. 6.1. The transmitted data symbols for K directions, denoted as $s_k(i), i = -\infty,\ldots,\infty, k = 1,\ldots,K$, are multiplied with the corresponding array vector $\mathbf{a}(\theta_k)$ before

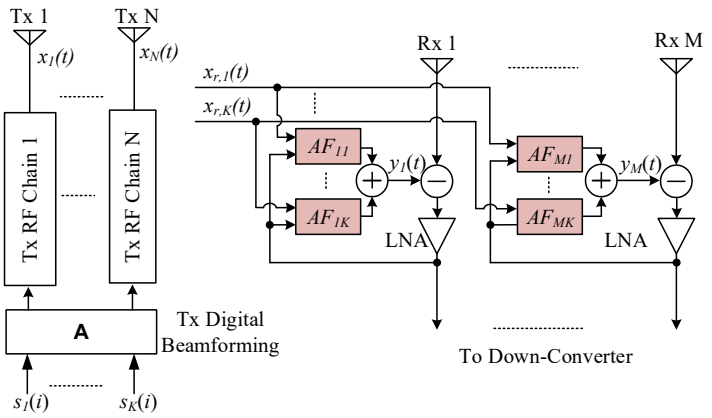

Figure 6.1: Proposed beam-based analog SIC structure.

added together and transmitted by N Tx chains. The vector of RF transmitted signals at N antennas is expressed as

$$\mathbf{x}(t) = \mathrm{Re}\left\{\mathbf{X}(t)e^{j2\pi f_c t}\right\} \tag{6.1}$$

where $\mathbf{X}(t) = [X_1(t) \cdots X_N(t)]^T$ is the baseband equivalent vector. $\mathbf{X}(t)$ can be expressed as

$$\mathbf{X}(t) = \mathbf{A}\mathbf{S}(t) = \begin{bmatrix} a_0(\theta_1) & \cdots & a_0(\theta_K) \\ \vdots & \ddots & \vdots \\ a_{N-1}(\theta_1) & \cdots & a_{N-1}(\theta_K) \end{bmatrix} \begin{bmatrix} S_1(t) \\ \vdots \\ S_K(t) \end{bmatrix} \tag{6.2}$$

where $a_n(\theta_k) = e^{jn\frac{2\pi}{\lambda}d\sin\theta_k}$, $n = 0,\ldots,N-1$, is the array vector of the beam at direction θ_k, d is the distance between antenna elements, $S_k(t) = \sum_{i=-\infty}^{\infty} s_k(i)p(t-iT_s)$ is the low-pass equivalent of the transmitted signal for the k-th user, $s_k(i)$ is the complex data symbol whose interval is T_s, and $p(t)$ is the pulse shaping filter. In the rest of this chapter, the following assumptions are applied.

1. Transmit data for all directions are independent, i.e.,

$$E\{s_k(i)^* s_{k'}(i')\} = \begin{cases} 1, \text{ for } k = k' \text{ and } i = i' \\ 0, \text{ for } k \neq k' \text{ or } i \neq i' \end{cases}. \tag{6.3}$$

2. All Tx and Rx chains are linear and have the same configuration. The gain of the power amplifier is absorbed into the pulse shaping filter.

Due to the IBFD operation, at the inputs of M Rx chains, there are M SI signals caused by N transmitted antennas, denoted as

$$\mathbf{z}(t) = \mathrm{Re}\{\mathbf{Z}(t)e^{j2\pi f_c t}\} = \mathrm{Re}\Big\{[Z_1(t),\ldots,Z_M(t)]^T e^{j2\pi f_c t}\Big\}.$$

Assuming that the SI channel between a pair of co-located Tx and Rx antennas includes L paths, and the transmitted signal in the l-th path is delayed by lT_d, $l = 0,\ldots,L-1$, where T_d is the time delay between two adjacent paths. The baseband equivalents of all of the SI signals can be represented as

$$\mathbf{Z}(t) = [Z_1(t)\cdots Z_M(t)]^T = \sum_{l=0}^{L-1} \mathbf{H}^H(l)\mathbf{A}\mathbf{S}(t-lT_d) \tag{6.4}$$

where $\mathbf{H}(l)= \begin{bmatrix} h_{1,1}(l) & \cdots & h_{1,M}(l) \\ \vdots & \ddots & \vdots \\ h_{N,1}(l) & \cdots & h_{N,M}(l) \end{bmatrix}$ is the $N \times M$ coefficient matrix at the l-th path of all SI channels.

It can be seen from (6.4) that the vector $\mathbf{Z}(t)$ is a linear combination of all basis vectors $\mathbf{S}(t-lT_d), l = 0,\ldots,L-1$. The concept of beam-based cancellation is that the vector of cancellation signals can be obtained by a linear transformation of the same basis $\mathbf{S}(t-lT_d), l = 0,\ldots,L-1$. This concept leads to two important points in the construction of the cancellation structure. Firstly, multi-tap adaptive filters to approximate all the SI channels should be used. Secondly, the reference signals for the cancellation circuit should be generated from the K beam signals. As illustrated in Fig. 6.1, at the input of the m-th Rx chain, K adaptive filters ($AF_{m,k}, k = 1,\ldots,K$) are employed to correspondingly modify the K reference signals $x_{r,k}(t), k = 1,\ldots,K$. The outputs of the K adaptive filters are added together to generate the cancellation signal $y_m(t), M = 1,\cdots,M$. If each adaptive filter also has L taps with the tap delay T_d, the vector of cancellation signals $\mathbf{y}(t) = [y_1(t),\ldots,y_M(t)]^T$ is represented by

$$\mathbf{y}(t) = \mathrm{Re}\Big\{\sum_{l=0}^{L-1} \mathbf{W}^H(l,t)\mathbf{x}_r(t-lT_d)\Big\} \tag{6.5}$$

where $\mathbf{W}(l,t) = \begin{bmatrix} w_{1,1}(l,t) & \cdots & w_{1,M}(l,t) \\ \vdots & \ddots & \vdots \\ w_{K,1}(l,t) & \cdots & w_{K,M}(l,t) \end{bmatrix}$ is the weighting coefficient matrix at the l-th tap of all adaptive filters, and $\mathbf{x}_r(t) = [x_{r,1}(t),\ldots,x_{r,K}(t)]^T$ is the vector of reference signals generated from beam signals $s_k(i), k = 1,\ldots,K$.

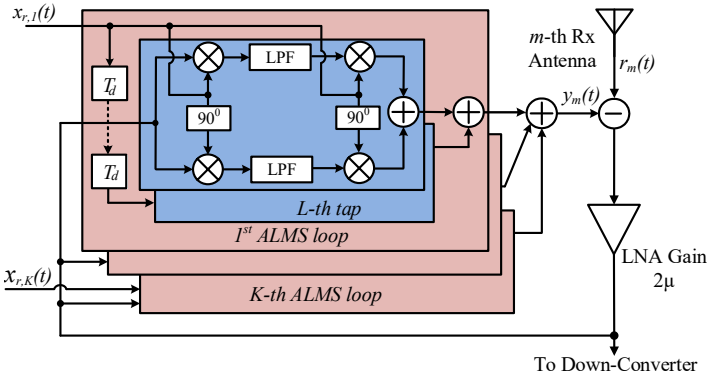

Figure 6.2: ALMS loop for beam-based cancellation structure.

6.2.2 ALMS Loop

As mentioned in Section 6.1, all adaptive filters can be implemented by ALMS loops as presented in Fig. 6.2. From the concept of beam-based cancellation, at the m-th Rx chain, K ALMS loops are employed to generate the cancellation signal. Operation of the ALMS loop is described as follows. Each ALMS loop has L taps in which each tap includes a tap delay, a quadrature demodulator, LPFs, and a quadrature modulator. The ALMS loop has two inputs for the reference and the looped-back signals and one output for the cancellation signal. For simplicity, the losses caused by power splitters for both reference and looped-back signals are normalized to one. Considering the k-th ALMS loop, at the l-th tap, the delayed reference signal $x_{r,k}(t-l)T_d), l = 0, \cdots, L-1$, is multiplied by the looped-back signal at the demodulator. The outputs of this demodulator are then filtered by the RC LPFs to obtain the weighting coefficients $w_{k,m}(l,t)$ which will modulate a copy of the delayed reference signal $x_{r,k}(t-lT_d)$ at the modulator. The outputs of all L taps are added together before combined with the outputs of other ALMS loops to generate the cancellation signal $y_m(t)$ which is used to cancel the SI $z_m(t)$ at the input of the m-th Rx chain. The residual signal is amplified and looped-back to the inputs of all ALMS loops.

The receive signal at the m-th Rx chain, denoted as $r_m(t)$, includes the desired signal from the remote end $s_{m,r}(t)$, the SI from N co-located transmitters $z_m(t)$ and the additive Gaussian noise $n_m(t)$, i.e., $r_m(t) = z_m(t) + s_{m,r}(t) + n_m(t) = \text{Re}\{[Z_m(t) + S_{m,r}(t) + N_m(t)]e^{j2\pi f_c t}\}$ where $Z_m(t), S_{m,r}(t)$ and $N_m(t)$ are the low-pass equivalents of these signals, respectively. Without loss of generality, we assume that the transmitted data $S_k(t), k = 1, \ldots, K$, $S_{m,r}(t)$, and $N_m(t), m = 1, \ldots, M$, are all independent.

From [9, Eq. (5)], the vector of weighting coefficients at the m-th Rx chain $\mathbf{w}_m(l,t) = [w_{1,m}(l,t),\ldots,w_{K,m}(l,t)]^T, l = 0,\ldots,L-1$, is obtained by

$$\mathbf{w}_m(l,t+t_0) = \frac{2\mu\alpha}{K_1K_2}\int_{t_0}^{t+t_0} e^{-\alpha(t-\tau)}[r_m(\tau)-y_m(\tau)]\mathbf{X}_r(\tau-lT_d)e^{j2\pi f_c(\tau-lT_d)}d\tau \tag{6.6}$$

where K_1 and K_2 are the dimensional constants of the multipliers inside the demodulators and modulators, respectively, 2μ is the gain of the LNA, $\alpha = 1/RC$ is the decay constant of the LPF with resistance R and capacitance C, $\mathbf{X}_r(t)$ is the vector of baseband equivalents of the reference signals, and $0 \le t_0 < T_s$ is an initial starting time.

6.3 Stationary Analysis

In this section, stationary analysis is applied to analyze the performance of the proposed structure. Strictly speaking, the signals in a digital communication system demonstrate cyclostationary properties [9]. Stationary analysis performs time averaging on the signals over one symbol duration T_s so that the system performance at macro scale can be tractably evaluated. Therefore, for stationary analysis, both ensemble expectation and time averaging (over one T_s) operations, denoted as $\bar{E}\{.\}$, are applied to evaluate the random processes. From the assumptions in Section 6.3, the normalized auto-correlation functions of the transmitted signals $S_k(t), k = 1,\ldots,K$, are defined as

$$\Phi_{k,k'}(\tau) = \frac{1}{K_1K_2}\bar{E}\left\{S_k^*(t)S_{k'}(t-\tau)\right\} = \begin{cases}\Phi(\tau) & \text{for } k = k'\\ 0 & \text{for } k \neq k'\end{cases} \tag{6.7}$$

where $\Phi(\tau) = \frac{1}{K_1K_2T_s}\int_0^{T_s} p^*(t)p(t-\tau)dt$.

6.3.1 Cancellation Performance

The cancellation performance of the proposed structure can be presented by the interference suppression ratio (ISR) which is the ratio between the total residual SI power $P_{\mathbf{d}}(t)$ after cancellation and the total SI power $P_{\mathbf{z}}$ across all Rx chains. Denoting the residual signal at the m-th Rx chain as $d_m(t) = z_m(t) - y_m(t)$, ISR is defined as

$$ISR(t) = \frac{P_{\mathbf{d}}(t)}{P_{\mathbf{z}}} \tag{6.8}$$

where $P_{\mathbf{d}}(t) = \sum_{m=1}^{M} P_{d_m}(t)$ and $P_{\mathbf{z}} = \sum_{m=1}^{M} P_{z_m}$. In this evaluation, we evaluate the performance of the proposed structure under one realization of the SI channels but with

random transmitted data symbols. Therefore, $P_{\mathbf{z}}$ does not change over the time. Meanwhile, the residual SI power is a function of time to show the convergence property of all ALMS loops. When the SI channels vary, the weighting coefficients of all ALMS loops will adapt accordingly. To derive $ISR(t)$, $P_{\mathbf{z}}$ and $P_{\mathbf{d}}(t)$ are calculated as follows.

6.3.1.1 Total SI power

In general, the SI signal at the m-th Rx chain can be expressed as

$$Z_m(t) = \sum_{n=1}^{N} \int_{-\infty}^{\infty} h_{n,m}^*(\tau) X_n(t-\tau) d\tau \tag{6.9}$$

where $h_{n,m}(\tau)$ as a function of time variable is the actual SI channel between the n-th Tx and m-th Rx antenna. The total normalized (to K_1K_2) SI power across all M Rx chains is calculated as

$$\begin{aligned} P_{\mathbf{z}} &= \sum_{m=1}^{M} \frac{1}{K_1K_2} \bar{E}\{z_m^2(t)\} = \sum_{m=1}^{M} \frac{1}{2K_1K_2} \bar{E}\{|Z_m(t)|^2\} \\ &= \frac{1}{2K_1K_2} \sum_{m=1}^{M} \sum_{n=1}^{N} \sum_{n'=1}^{N} \int_{-\infty}^{\infty} \int_{-\infty}^{\infty} h_{n,m}^*(\tau) \bar{E}\{X_n(t-\tau) X_{n'}^*(t-\tau')\} h_{n',m}(\tau') d\tau d\tau' \\ &= \frac{1}{2K_1K_2} \sum_{m=1}^{M} \sum_{n=1}^{N} \sum_{n'=1}^{N} \int_{-\infty}^{\infty} \int_{-\infty}^{\infty} h_{n,m}^*(\tau) \Phi(\tau-\tau') \mathbf{a}_n \mathbf{a}_{n'}^H h_{n',m}(\tau') d\tau d\tau' \end{aligned} \tag{6.10}$$

where $\mathbf{a}_n$ is the n-th row of the matrix $\mathbf{A}$.

The ALMS loop is designed based on the assumption that the SI channel can be approximated as a L-stage filter, i.e.,

$$Z_m(t) = \sum_{n=1}^{N} \int_{-\infty}^{\infty} h_{n,m}^*(\tau) X_n(t-\tau) d\tau \approx \sum_{n=1}^{N} \sum_{l=0}^{L-1} h_{n,m}^*(l) X_n(t-lT_d). \tag{6.11}$$

Therefore, the vector $h_{n,m}(l), l = 0,\ldots,L-1, n = 1,\ldots,N$, can be found by minimizing the following modeling error

$$\epsilon_m^2 = \frac{1}{K_1K_2} \bar{E}\Big\{ \Big| \sum_{n=1}^{N} \int_{-\infty}^{\infty} h_{n,m}^*(\tau) X_n(t-\tau) d\tau - \sum_{n=1}^{N} \sum_{l=0}^{L-1} h_{n,m}^*(l) X_n(t-lT_d) \Big|^2 \Big\}. \tag{6.12}$$

Geometrically, $X_n(t-lT_d), n = 1,\cdots,N,$ and $l = 0,\cdots,L-1$, can be seen as an orthogonal basis in the space $\mathbb{C}^{N\times L}$. From the principle of orthogonality, the modeling error is minimized when $h_{n,m}^*(l)X_n(t-lT_d)$ are the projections of $Z_m(t)$ on $\mathbb{C}^{N\times L}$, i.e.,

$$\bar{E}\Big\{ X_n(t-lT_d) \Big[\sum_{n'=1}^{N} \int_{-\infty}^{\infty} h_{n',m}(\tau) X_{n'}^*(t-\tau) d\tau - \sum_{n'=1}^{N} \sum_{l'=0}^{L-1} h_{n',m}(l') X_{n'}^*(t-l'T_d) \Big] \Big\} = 0 \tag{6.13}$$

for $n = 1,\ldots,N$ and $l = 0,\ldots,L-1$. After some manipulations and extensions for M Rx chains (see Appendix A.5), we find the vector of modeled channel coefficients $\mathbf{h} = [h_{1,1}(0),\ldots h_{1,1}(L-1),\ldots h_{N,M}(0)\ldots h_{N,M}(L-1)]^T$ as

$$\mathbf{h} = [\mathbf{I}_{NM} \otimes \mathbf{\Phi}]^{-1} \begin{bmatrix} \int_{-\infty}^{\infty} \Phi(-\tau) h_{1,1}(\tau) d\tau \\ \vdots \\ \int_{-\infty}^{\infty} \Phi((L-1)T_d - \tau) h_{N,M}(\tau) d\tau \end{bmatrix} \tag{6.14}$$

where $\mathbf{\Phi} = \begin{bmatrix} \Phi(0) & \Phi(-T_d) & \cdots & \Phi(-(L-1)T_d) \\ \vdots & \vdots & \ddots & \vdots \\ \Phi((L-1)T_d) & \Phi((L-2)T_d) & \cdots & \Phi(0) \end{bmatrix}$ is the auto-correlation matrix of the transmitted signals. Therefore, when calculating the signal power using the SI channel model, we need to take into account the total modeling error, denoted as ϵ, derived in Appendix A.5 as

$$\epsilon^2 = \sum_{m=1}^{M} \epsilon_m^2 = \sum_{m=1}^{M} \sum_{n=1}^{N} \sum_{n'=1}^{N} \int_{-\infty}^{\infty} \int_{-\infty}^{\infty} h_{n,m}^*(\tau) \Phi(\tau - \tau') \mathbf{a}_n \mathbf{a}_{n'}^H h_{n',m}(\tau') d\tau d\tau' - \underline{\mathbf{h}}^H [\mathbf{I}_M \otimes \mathbf{\Theta}] \underline{\mathbf{h}} \tag{6.15}$$

where $\underline{\mathbf{h}} = [\mathbf{I}_M \otimes (\mathbf{A}^H \otimes \mathbf{I}_L)]\mathbf{h}$, and $\mathbf{\Theta} = \mathbf{I}_K \otimes \mathbf{\Phi}$. Hence, the total normalized SI power at all M Rx chains can also be calculated as

$$P_{\mathbf{z}} = \frac{1}{2}\epsilon^2 + \frac{1}{2}\underline{\mathbf{h}}^H [\mathbf{I}_M \otimes \mathbf{\Theta}] \underline{\mathbf{h}}. \tag{6.16}$$

6.3.1.2 Residual SI power

Following the same steps above, the power of the residual SI at the m-th Rx chain can be calculated as

$$\begin{aligned} P_{d_m}(t) &= \frac{1}{K_1 K_2} \bar{E}\{[z_m(t) - y_m(t)]^2\} = \frac{1}{2K_1 K_2} \bar{E}\{|Z_m(t) - Y_m(t)|^2\} \\ &= \frac{1}{2K_1 K_2} \bar{E}\Big\{\Big|\big[Z_m(t) - \sum_{l=0}^{L-1} \mathbf{h}_m^H(l) \mathbf{X}(t - lT_d)\big] + \\ &\sum_{l=0}^{L-1} \big[\mathbf{h}_m^H(l) \mathbf{X}(t - lT_d) - \mathbf{w}_m^H(l,t) e^{-j2\pi f_c l T_d} \mathbf{X}_r(t - lT_d)\big]\Big|^2\Big\} \end{aligned} \tag{6.17}$$

where $\mathbf{h}_m(l), \mathbf{w}_m(l)$ are the m-th column vectors of the matrices $\mathbf{H}(l), \mathbf{W}(l)$, respectively, $\mathbf{X}_r(t) = \mathbf{A}_r \mathbf{S}(t)$ is the low-pass equivalent of K reference signals selected from $\mathbf{X}(t)$, and $\mathbf{A}_r \subset \mathbf{A}$ is a $K \times K$ matrix obtained from $\mathbf{A}$. Since $\mathbf{X}_r(t)$ is a subset of $\mathbf{X}(t)$, from the

principle of orthogonality, $P_{d_m}(t)$ can be rewritten as

$$P_{d_m}(t) = \frac{1}{2}\epsilon_m^2 + \frac{1}{2K_1K_2}\bar{E}\left\{\left|\sum_{l=0}^{L-1}\left[\mathbf{h}_m^H(l)\mathbf{A} - \mathbf{w}_m^H(l,t)e^{-j2\pi f_c l T_d}\mathbf{A}_r\right]\mathbf{S}(t-lT_d)\right|^2\right\}. \tag{6.18}$$

Denote $\mathbf{u}_m(l,t) = [u_{m,1}(l,t),\ldots,u_{m,K}(l,t)]^T = \mathbf{A}^H\mathbf{h}_m(l) - \mathbf{A}_r^H\mathbf{w}_m(l,t)e^{j2\pi f_c l T_d}$ as the vector of weighting error functions, which shows the difference between the channel coefficients of the l-th tap in the SI channel and the weighting coefficients of the same tap in the K ALMS loops at the m-th Rx chain. The expression of $P_{d_m}(t)$ becomes

$$\begin{aligned}
P_{d_m}(t) &= \frac{1}{2}\epsilon_m^2 + \frac{1}{2K_1K_2}\bar{E}\left\{\left|\sum_{l=0}^{L-1}\mathbf{u}_m^H(l,t)\mathbf{S}(t-lT_d)\right|^2\right\} \\
&= \frac{1}{2}\epsilon_m^2 + \frac{1}{2K_1K_2}\bar{E}\left\{\sum_{l=0}^{L-1}\mathbf{u}_m^H(l,t)\mathbf{S}(t-lT_d)\sum_{l'=0}^{L-1}\mathbf{S}^H(t-l'T_d)\mathbf{u}_m(l',t)\right\} \\
&= \frac{1}{2}\epsilon_m^2 + \frac{1}{2}\sum_{l=0}^{L-1}\sum_{\substack{l'=0\\l'\neq l}}^{L-1}\bar{\bar{\mathbf{u}}}_m^H(l,t)\boldsymbol{\Theta}((l-l')T_d)\bar{\bar{\mathbf{u}}}_m(l',t) + \frac{1}{2}\Phi(0)\sum_{l=0}^{L-1}\sum_{k=1}^{K}\bar{\bar{u}}_{m,k}^2(l,t) \\
&= \frac{1}{2}\epsilon_m^2 + \frac{1}{2}\bar{\bar{\mathbf{u}}}_m^H(t)\boldsymbol{\Theta}\bar{\bar{\mathbf{u}}}_m(t) + \frac{1}{2}\Phi(0)\left[\sum_{l=0}^{L-1}\sum_{k=1}^{K}\bar{\bar{u}}_{m,k}^2(l,t) - \bar{\bar{\mathbf{u}}}_m^H(t)\bar{\bar{\mathbf{u}}}_m(t)\right]
\end{aligned} \tag{6.19}$$

where $\bar{\bar{\mathbf{u}}}_m(l,t) = \bar{E}\{\mathbf{u}_m(l,t)\}$ and $\bar{\bar{u}}_{m,k}^2(l,t) = \bar{E}\{u_{m,k}^2(l,t)\}$. Hence, the total residual SI power of all M Rx chains is represented by

$$\begin{aligned}
P_{\mathbf{d}}(t) &= \sum_{m=1}^{M}P_{d_m}(t) \\
&= \frac{1}{2}\epsilon^2 + \frac{1}{2}\bar{\bar{\mathbf{u}}}^H(t)[\mathbf{I}_M\otimes\boldsymbol{\Theta}]\bar{\bar{\mathbf{u}}}(t) + \frac{1}{2}\Phi(0)\left[\sum_{m,k,l}\bar{\bar{u}}_{m,k}^2(l,t) - \bar{\bar{\mathbf{u}}}^H(t)\bar{\bar{\mathbf{u}}}(t)\right]
\end{aligned} \tag{6.20}$$

where $\bar{\bar{\mathbf{u}}}(t) = [\bar{\bar{u}}_{1,1}(0,t),\ldots,\bar{\bar{u}}_{1,1}(L-1,t),\ldots,\bar{\bar{u}}_{M,K}(L-1,t)]^T$. Therefore, we need to derive the weighting error function vector $\bar{\bar{\mathbf{u}}}(t)$ and $\sum_{m,k,l}\bar{\bar{u}}_{m,k}^2(l,t)$ to calculate the residual SI power.

Substituting the definition of the weighting error function into (6.6), after some multiplications (see Appendix A.6), we have the equation that the expected weighting error function vector should satisfy

$$\bar{\bar{\mathbf{u}}}(t) = \underline{\mathbf{h}} - \mu\alpha\int_0^t e^{-\alpha(t-\tau)}\boldsymbol{\Psi}\bar{\bar{\mathbf{u}}}(\tau)d\tau \tag{6.21}$$

where $\boldsymbol{\Psi} = \mathbf{I}_M\otimes\left[(\mathbf{B}\otimes\mathbf{I}_L)\boldsymbol{\Theta}\right]$ with $\mathbf{B} = \mathbf{A}_r^H\mathbf{A}_r$. It is seen that (6.21) has the same form as that in the single antenna case [9, Eq. (26)]. Following similar steps shown in [9], the

solution of the expected the weighting error function vector is obtained as

$$\begin{aligned}
\bar{\tilde{\mathbf{u}}}(t) &= \mathbf{Q}\text{diag}\Big\{\frac{1}{1+\mu\lambda_i}+\frac{\mu\lambda_i}{1+\mu\lambda_i}e^{-(1+\mu\lambda_i)\alpha t}\Big\}\mathbf{Q}^{-1}\underline{\mathbf{h}},\\
\sum_{m,k,l}\bar{\tilde{u}}^2_{m,k}(l,t) &= \underline{\mathbf{h}}^H\mathbf{Q}\text{diag}\Big\{\frac{1}{(1+\mu\lambda_i)^2}+\frac{2\mu\lambda_i}{(1+\mu\lambda_i)^2}\times\\
&e^{-(1+\mu\lambda_i)\alpha t}+\frac{(\mu\lambda_i)^2e^{-2(1+\mu\lambda_i)\alpha t}}{(1+\mu\lambda_i)^2}-e^{-2(1+\mu\bar{\lambda})\alpha t}\Big\}\mathbf{Q}^{-1}\underline{\mathbf{h}}
\end{aligned} \tag{6.22}$$

where $\lambda_i, i = 1,\ldots,M\times K\times L$, are the eigenvalues of $\mathbf{\Psi}$ and $\mathbf{Q}$ is the orthonormal modal matrix whose columns are the $M\times K\times L$ eigenvectors of $\mathbf{\Psi}$, and $\bar{\lambda} = \Phi(0)$.

From (6.16) and (6.20), we obtain the ISR as

$$\begin{aligned}
ISR(t) &= \frac{P_{\mathbf{d}}(t)}{P_{\mathbf{z}}}\\
&= \frac{\epsilon^2+\bar{\tilde{\mathbf{u}}}^H(t)[\mathbf{I}_M\otimes\mathbf{\Theta}]\bar{\tilde{\mathbf{u}}}(t)+\bar{\lambda}\Big[\sum\limits_{m,k,l}\bar{\tilde{u}}^2_{m,k}(l,t)-\bar{\tilde{\mathbf{u}}}^H(t)\bar{\tilde{\mathbf{u}}}(t)\Big]}{\epsilon^2+\underline{\mathbf{h}}^H[\mathbf{I}_M\otimes\mathbf{\Theta}]\underline{\mathbf{h}}}.
\end{aligned} \tag{6.23}$$

Eq. (6.23) represents the performance of the proposed structure at time instance t. We can see that when $t\gg\frac{1}{\alpha(1+\mu\bar{\lambda})}$, all the ALMS loops will converge to their stable state. In this case, $\bar{\tilde{\mathbf{u}}}(t)\to\bar{\tilde{\mathbf{u}}} = \mathbf{Q}\text{diag}\Big\{\frac{1}{1+\mu\lambda_i}\Big\}\mathbf{Q}^{-1}\underline{\mathbf{h}}$ and $\sum\limits_{m,k,l}\bar{\tilde{u}}^2_{m,k}(l,t)\to\bar{\tilde{\mathbf{u}}}^H\bar{\tilde{\mathbf{u}}}$, (6.23) becomes

$$\begin{aligned}
ISR &= ISR(t)|_{t\gg\frac{1}{\alpha(1+\mu\bar{\lambda})}}\\
&= \frac{\epsilon^2+\bar{\tilde{\mathbf{u}}}^H[\mathbf{I}_M\otimes\mathbf{\Theta}]\bar{\tilde{\mathbf{u}}}}{\epsilon^2+\underline{\mathbf{h}}^H[\mathbf{I}_M\otimes\mathbf{\Theta}]\underline{\mathbf{h}}}.
\end{aligned} \tag{6.24}$$

From (6.24), when $M = N = K = 1$ corresponding to an IBFD single antenna system, (6.24) becomes [9, Eq. (39)]. It means that the ALMS loop in the IBFD single antenna system is a special case of this beam-based cancellation structure. Hence, the properties of the ALMS loop presented in [9, 58, 59, 61, 81], such as the interference suppression lower bound and convergence speed, are also applicable in this case. It can also be seen from (6.22) and (6.24) that, apart from the parameters of the ALMS loops employed in the adaptive filters, the performance of this beam-based analog SIC structure also depends on the reference signals whose impact is represented by the matrix $\mathbf{B}$ incorporated in $\mathbf{\Psi}$. The problem of generating the reference signals is studied in the next Section.

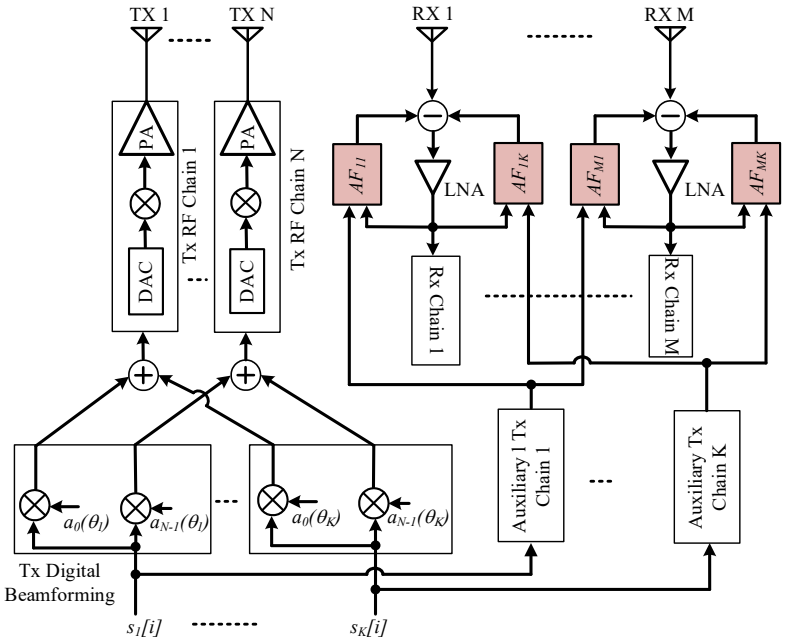

Figure 6.3: Beam-based analog SIC with auxilary transmit chains.

6.4 Reference Signals Generation

6.4.1 Using Additional Transmit Chains

6.4.1.1 The Structure

The easiest way to generate the reference signals from the transmitted beam data is employing additional transmit chains. As shown in Fig. 6.3, K auxiliary Tx chains whose configurations are the same as those in the main Tx paths, are used to up-convert the Tx beam data into reference signals.

In this case, $\mathbf{x}(t) = \mathbf{S}(t)$, so that $\mathbf{B} = \mathbf{I}_K$, $\mathbf{\Psi} = \mathbf{I}_M \otimes \mathbf{\Theta} = \mathbf{I}_{MK} \otimes \mathbf{\Phi}$, (7.3) becomes

$$ISR = \frac{\epsilon^2 + \underline{\mathbf{h}}^H \mathbf{Q} \text{diag}\{\frac{\lambda_i}{(1+\mu\lambda_i)^2}\} \mathbf{Q}^{-1} \underline{\mathbf{h}}}{\epsilon^2 + \underline{\mathbf{h}}^H \mathbf{Q} \text{diag}\{\lambda_i\} \mathbf{Q}^{-1} \underline{\mathbf{h}}}. \tag{6.25}$$

From the property of the Kronecker product, since the eigenvalues of $\mathbf{I}_{MK}$ are all one, $\lambda_i, i = 1, \ldots, MKL$, are $M \times K$ replica of the eigenvalues of $\mathbf{\Phi}$. Therefore, (6.25) gives the same result as [9, Eq. (39)] in single antenna systems. It means that if additional Tx chains were employed to generate the reference signals for the $M \times K$ ALMS loops, the SIC performance would be the same as that of the ALMS loop in a single antenna IBFD system.

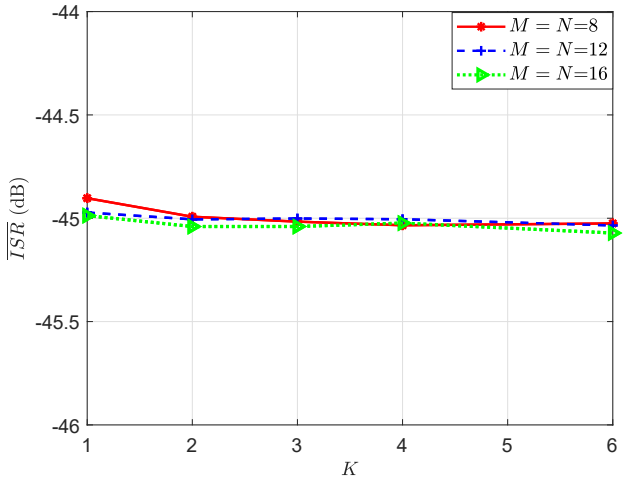

Figure 6.4: The averaged and converged interference suppression ratio.

In order to confirm the above analyses, the ISR calculated in (6.25) is evaluated over many realizations of the SI channel using the averaged interference suppression ratio $\overline{ISR} = \bar{E}_h\{ISR\}$ where $\bar{E}_h$ stands for expectation over the SI channel. Fig. 6.4 presents $\overline{ISR}$ obtained by averaging over 1000 realizations of the SI channel whose coefficients are assumed to be independent and have Gaussian distribution with zero mean. We can see that $\overline{ISR}$ is almost stable with different number of transmit and receive antennas as well as the number of beams. It means that the beam-based cancellation architecture works as expected and the level of SI mitigation can be determined by the performance of the adaptive filters.

6.4.1.2 Simulation Results

The simulations are then performed for beamforming IBFD MIMO systems with the distance between antenna elements is selected at a half of wave-length. The QPSK modulated data symbols for all beams have duration of $T_s = 20$ ns and the carrier frequency is $f_c = 5$ GHz. The transmit chains in both main paths and auxiliary paths employ root-raised cosine filters with roll-off factors $\beta = 0.25$. The power of the transmitted signal per antenna is 0 dBm, and the multiplier dimensional constants are $K_1K_2 = 0.001\ V^2$. The LNA gain 2μ in all the receiver chains is selected as $\mu = 10$. The ALMS loop is designed with $L = 8$ taps and the tap delay is selected as $T_d = T_s/2$. The SI channel between a pair of transmit and receive antenna is modeled with $L = 8$ taps and the propagation delay of each tap is the same as that in the ALMS loop. The propagation losses of all SI channels are set to be 25 dB.

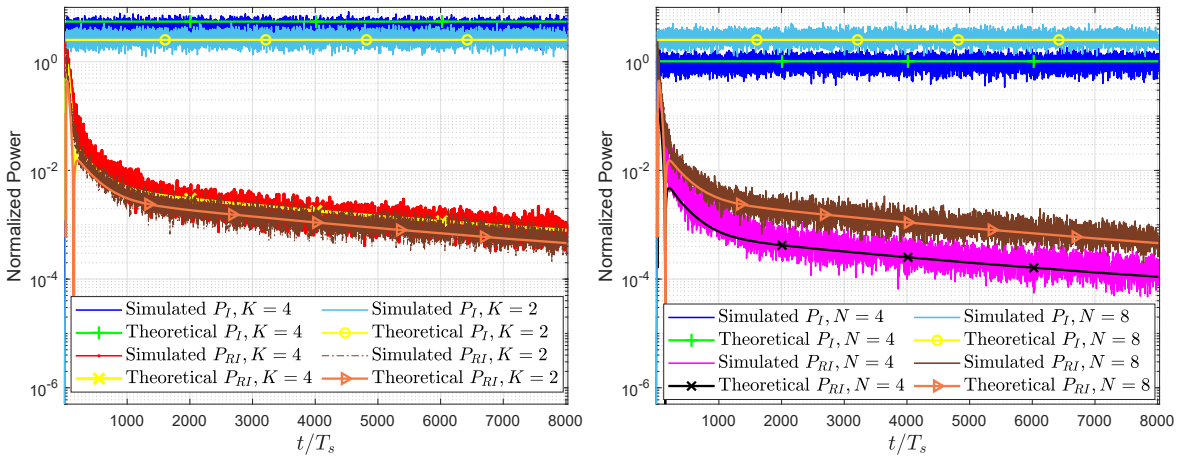

(a) (b)

Figure 6.5: Normalized SI and residual SI powers for (a) 8×8 IBFD MIMO systems and (b) 2 beams IBFD MIMO systems.

In the first simulation, an 8×8 IBFD MIMO system is simulated with two cases of the number of beams $K = 2$ and $K = 4$. In the second simulation, the number of beams is fixed at $K = 2$ for a 4×4 and 8×8 IBFD MIMO systems. The SI powers and residual SI powers in the first and second simulations are plotted in Fig. 6.5 (a) and (b), respectively. From these figures, the theoretical results match the simulated results in all cases which confirm the theoretical analyses presented in Section 6.4.1.1. We can also see that the level of the SI power increases with the number of beams and transmit antennas. However, the ISRs in all cases are almost the same at $t = 8000T_s$.

6.4.2 Selecting from Transmitted Signals

6.4.2.1 The Structure

The structure in Fig. 6.3 is still complicated with the auxiliary Tx chains required. To further reduce the hardware complexity, the reference signals from N Tx signals can be chosen as shown in Fig. 6.6. Since no additional Tx chain is employed in this structure, a new factor affecting its performance is how to select the reference signals from N transmitted signals. A method to select the reference signals from N Tx signals is proposed as follows. From (7.3), the performance of the proposed structure can be represented by the weighting error function vector $\bar{\bar{\mathbf{u}}}$. The smaller $\bar{\bar{\mathbf{u}}}$ is, the lower ISR will be obtained. From the definition of $\bar{\bar{\mathbf{u}}}$, the problem of reference signal selection can be stated as how to select a $K \times K$ matrix $\mathbf{A}_r$ from the given $N \times K$ matrix $\mathbf{A}$ to minimize $\bar{\bar{\mathbf{u}}}$.

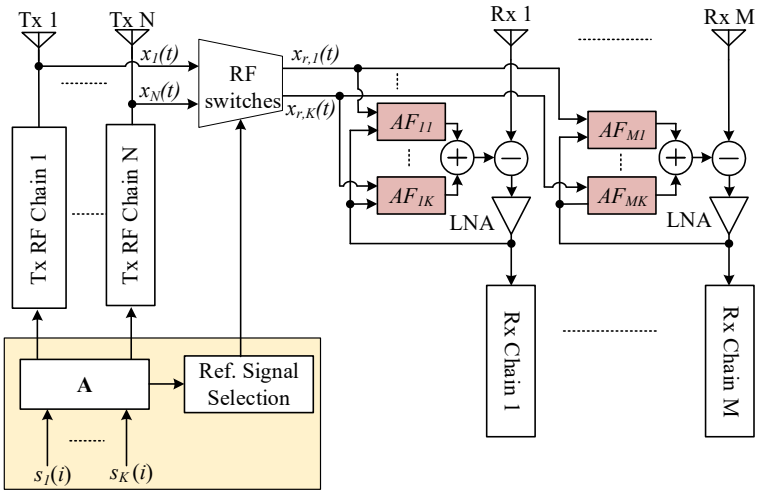

Figure 6.6: Proposed beam-based analog SIC structure.

Since both $\mathbf{A}^H\mathbf{h}_m(l)$ and $\mathbf{A}_r^H\mathbf{w}_m(l,t)e^{j2\pi f_c l T_d}$ result in two vectors in the same space $\mathbb{C}^K$, the solution of this problem always exist. However, as $\mathbf{w}_m(l,t)$ is unknown, it is unable to find the solution using conventional least square approach. Instead, an algorithm is proposed to find a sub-optimal solution as follows.

Defining $\mathbf{\Omega} = \mathbf{Q}\text{diag}\left\{\frac{1}{1+\mu\lambda_i}\right\}\mathbf{Q}^{-1}, i = 1,\ldots,M\times K\times L$, from $\bar{\underline{\mathbf{u}}} = \mathbf{\Omega}\underline{\mathbf{h}}$, we see that $\mathbf{\Omega}$ is the transformation matrix of vector $\underline{\mathbf{h}}$, and $|\det(\mathbf{\Omega})|$ is the scaling factor of this transformation. As an example, Fig. 6.7 shows the transformation from $\underline{\mathbf{h}}$ to $\bar{\underline{\mathbf{u}}}$ when they are in the two dimensional space. The area of the rectangular defined by $\bar{\underline{\mathbf{u}}}$ (blue) is equal to that of the rectangular defined by $\underline{\mathbf{h}}$ (green) multiplied by $|\det(\mathbf{\Omega})|$. Therefore, $\mathbf{A}_r$ can be selected based on $|\det(\mathbf{\Omega})|$. From $\det(\mathbf{\Omega}) = \prod_{i=1}^{M\times K\times L}\frac{1}{1+\mu\lambda_i}$, $\mathbf{A}_r$ can be found if the eigenvalues of the

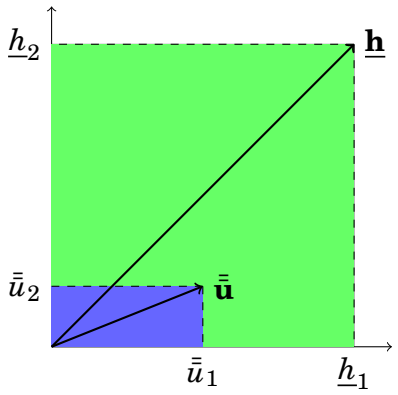

Figure 6.7: Transformation from $\underline{\mathbf{h}}$ to $\bar{\underline{\mathbf{u}}}$.

matrix $\mathbf{\Psi}$ satisfy that $D_\Omega = |\prod_{i=1}^{M\times K\times L}(1+\mu\lambda_i)|$ is maximized. The solution found in this way is sub-optimal because there may be several selections of $\mathbf{A}_r$ that give the same D_Ω, and ISR is determined by the modulus of $\bar{\bar{\mathbf{u}}}$ rather than its volume. However, this is a simple method and the solution will always be found even though $\mathbf{A}$ may not be full ranked. The algorithm to select the reference signals is given in Algorithm 1 and is described as follows. Since $\mathbf{A}_r$ is formed by a combination of K rows from N rows in the matrix $\mathbf{A}$, there are $\binom{N}{K}$ possible selections which are indexed as $Rind$. $\mathbf{A}_r$ and $\mathbf{\Psi}$ are then constructed, and D_Ω is calculated for all $\binom{N}{K}$. The sub-optimal $\mathbf{A}_r$ is found if it gives the highest D_Ω. In Fig. 6.6, Algorithm 1 can be run in the reference signal selection block in the digital domain. From the users' beam angle information and transmitted signal autocorrelation matrix, the reference signals are determined and then connected to the cancellation circuits by the corresponding RF switches.

Algorithm 1 Selection of reference signals

procedure FIND($\mathbf{A}_r$)
  Input $\mathbf{A}, \mathbf{\Phi}$.
  Number of selections: $NoS = \binom{N}{K}$.
  Possible combinations of N rows of A: $Rind = \binom{[1:N]}{K}$.
  for $n = 1$ to NoS **do**
    Generate $\mathbf{A}_r$ from $\mathbf{A}$: $\mathbf{A}_r = \mathbf{A}(Rind(n),:)$;
    Compute $\mathbf{\Psi}$ and its eigenvalues λ_i;
    Compute $D_\Omega(n) = \prod_{i=1}^{M\times K\times L}(1+\mu\lambda_i)$;
  end for
  Find the maximum of D_Ω
  Optimal reference signals found!
end procedure

As an example, consider an 8×8 beamforming IBFD systems with 4 distinguished beams at angles $\theta_k = k\pi/8, k = 1,\ldots,4$. All SI channels have 8 paths each with the path delay being the same as the tap delay in the ALMS loops. From 8 transmitted signals, there are 70 possible selections of the reference signals. Figure 6.8(a) presents the geometric mean of D_Ω calculated for all possible selections of $\mathbf{A}_r$ as well as the case of $\mathbf{A}_r = \mathbf{I}_K$. It is seen that the maximum of D_Ω appears at $n = 22$ and $n = 30$. $\mathbf{A}_r$ constructed at either these two positions is acceptable because the difference of ISRs given by them is negligible as can be seen in Fig. 6.8(b). It is also worth noting that the optimal selection of the reference signals in the proposed structure provides higher level of cancellation than the case with additional Tx chains. This is because the beamforming matrix has

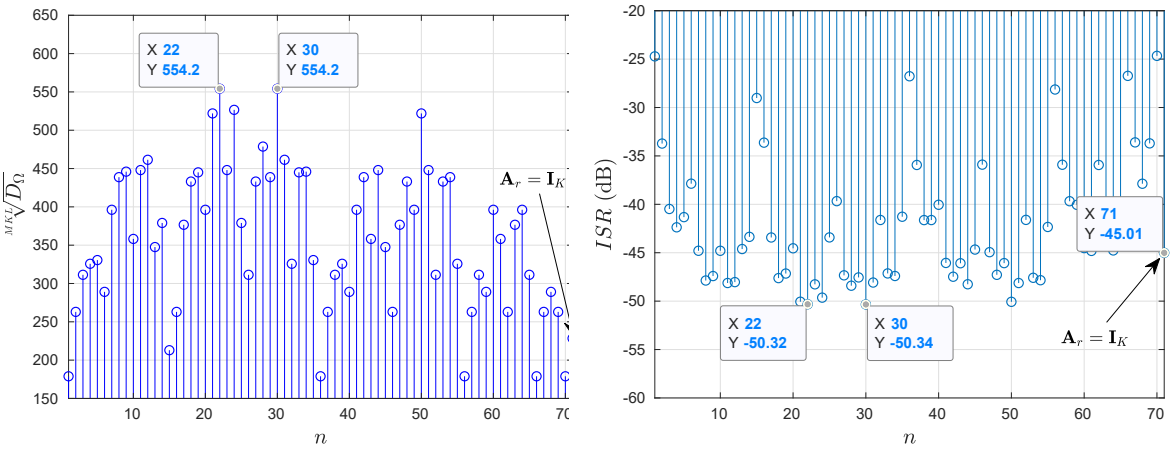

(a) (b)

Figure 6.8: (a) Geometric mean of D_Ω and (b) ISR for all possible selections of $\mathbf{A}_r$

an impact on the autocorrelation function of the transmitted signals so that the level of cancellation can be improved.

6.4.2.2 Simulation Results

Simulations are performed to illustrate the behaviors of the proposed cancellation structure. In all simulations, an 8×8 beamforming IBFD MIMO system communicates with four users at angles of $\theta_k = k\pi/8, k = 1, \ldots, 4$. The antenna elements are spaced at 30 mm which is a half of the wave-length of the transmitted carrier frequency $f_c = 5$ GHz. Data for all users are independent and QPSK modulated with symbol duration of $T_s = 20$ ns. In all Tx chains, root-raised cosine pulse shaping filters with roll-off factor $\beta = 0.25$ are employed. The power of the transmitted signal per antenna is 0 dBm for 50 Ohm load. The transmitted signals at the outputs of 8 antennas are labeled from 1 to 8 for reference signal selections. On the receiver side, the LNA gain 2μ in each Rx chain is selected as $\mu = 10$. The ALMS loops are designed with $L = 8$ taps equally spaced at $T_d = T_s/2$. The multiplier dimensional constants are set at $K_1 K_2 = 0.001\ V^2$. The LPF parameter of all ALMS loop is chosen as $\alpha T_s = 1.7655 \times 10^{-5}$ which is the same as that in [9]. The propagation losses of all SI channels are set to be 25 dB. In the first two simulations, the reference signals are chosen based on Algorithm 1, which are coupled at the outputs of Tx chains 1, 3, 5 and 8.

In the first simulation, the SI channel between a pair of Tx and Rx antennas is modeled with $L = 8$ paths and the multipaths have arbitrary delays. Specifically, the delay

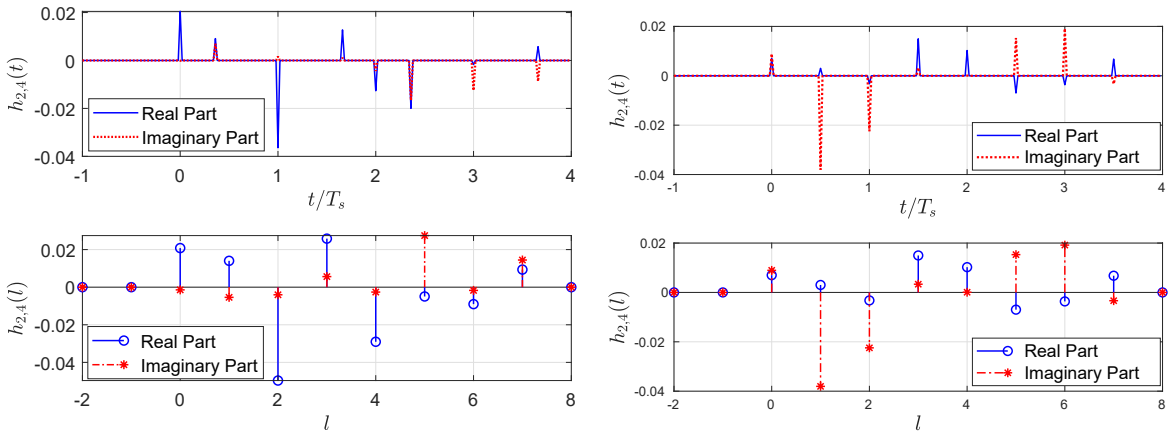

Figure 6.9: SI channel impulse response $h_{2,4}(t)$ (top) and modeled tap coefficients $h_{2,4}(l)$ (bottom) for (a) arbitrary and (b) T_d spaced delay between multipaths.

of the l-th path is chosen as $(l-1.5+rand)T_d$ where $rand$ is an uniformly distributed random number between 0 to 1. It means that the maximum delay experienced by the SI signals is limited to be smaller than LT_d which is the delay range covered by the ALMS loops. Fig. 6.9(a) presents the impulse response (top) and the modeled tap coefficients (bottom) of the SI channel from the fourth transmit antenna to the second received antenna. The modeling error calculated from (6.15) in this case is 0.002. In the second simulation, the SI channels for all pairs of Tx and Rx antennas are modeled to have the same number of paths and path delays as those in the ALMS loop so that the modeling error is zero. The channel impulse response and the modeled channel coefficients for the same SI channel in the first simulation are presented in Fig. 6.9(b).

Results of these two simulations are presented in Fig. 6.10. It can be seen in both simulations that the simulated results match the theoretical $ISR(t)$ (obtained from (6.23)) and hence confirm the analyses presented in Section 6.3. Due to the modeling error in the first simulation, the level of cancellation given by the ALMS loops is about 5 dB less than that in the second simulation. However, a level of 38 dB cancellation is still achieved.

In the third simulation, the reference signals are selected from the first four transmitted signals while the SI channels are modeled in the same way as in the second simulation. The simulation result for this case is presented in Fig. 6.11. It is seen that even though the ALMS loop has exactly the same tap delay as in the SI channel, the performance of the ALMS loop is worse than that in the first simulation. These results

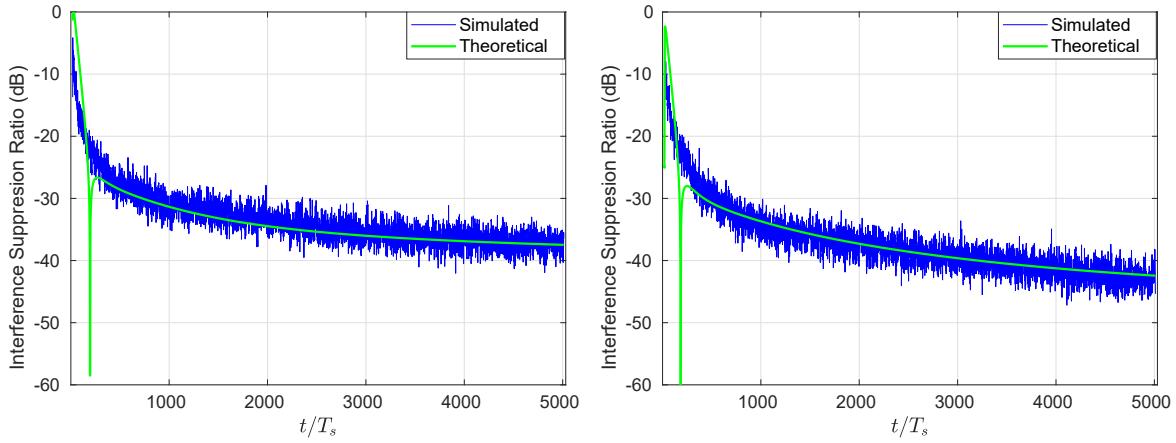

Figure 6.10: Interference suppression ratio under (a) arbitrary delay interference channel and (b) T_d spaced interference chanel.

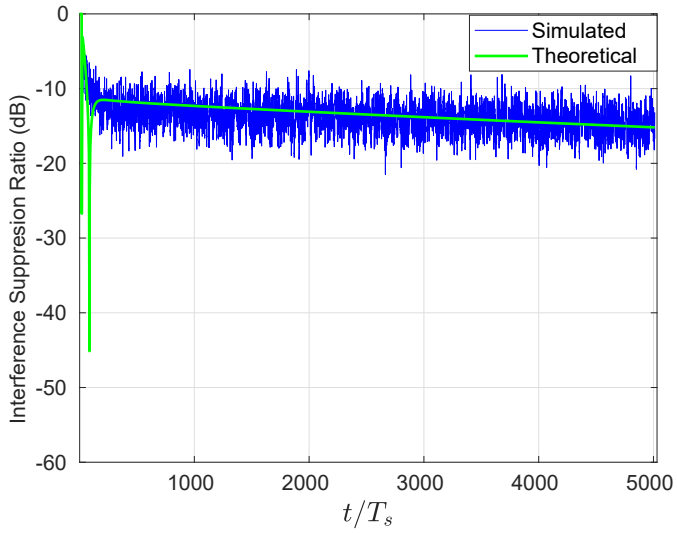

Figure 6.11: Interference suppression ratio with the worst reference signals.

demonstrate the importance of the selection of reference signals on the performance of the ALMS loop.

The complexity and performance of the proposed structure are compared with those of some other existing RF domain cancellation methods [45, 78, 79, 82, 83] as summarized in Table 6.1. In this comparison, the complexity of each work includes the analog circuits, the requirement of CSI, and the involvement of DSP for tuning the cancellation circuits. The performance of these methods in terms of ISR is also provided for information and reference purpose since these IBFD MIMO systems have different number of antennas

Table 6.1: Comparison with existing methods for IBFD MIMO

	Complexity			ISR (dB)	Comments
	Analog circuits	DSP	CSI		
[24]	O(ML)	Involved	Required	40	3×3 MIMO
[28]	O(MNL)	Involved	Required	40	2×2 MIMO
[29], [38], [39]	O(M)+MUX/DEMUX	Involved	Required	N/A	4×4 MIMO
Proposed	O(MKL)	No	No	38-42	8×8 MIMO

and transmission bandwidths. In addition, some baselines [45, 82, 83] present the sum-rate rather than ISR. As can be seen in Table 6.1, all other baselines require DSP and CSI for tuning analog cancellation circuits.

6.5 Conclusion

In this chapter, a novel beam-based analog SIC architecture has been proposed, which significantly reduces both hardware and signal processing complexities conventionally required for SI mitigation in IBFD MIMO systems. Considering interference at the receiver side as a linear combination of the data transmitted from all beams, it has proved that the number of adaptive filters at each Rx chain is reduced to the number of transmitted beams rather than as high as the number of Tx antennas. Further, different methods of generating reference signals have been investigated. Apart from using additional Tx chains, a novel method has been proposed to select the optimized reference signals for the adaptive filters from the Tx antennas. Stationary analysis shows that, the level of SIC given by the proposed structure is higher than that obtained by employing ALMS loops for the same number of adaptive filters with reference signals generated by additional Tx chains.

CHAPTER 7

ALMS LOOP - A PRACTICAL PERSPECTIVE

7.1 Introduction

The analyses shown in the previous chapters reveal all the properties of the ALMS loop in different applications. However, these results are only confirmed by simulations in MATLAB, rather than by hardware experiments. In addition, although the ALMS loop has a simple structure, its implementation using off-the-shelf components is still a challenging task. For example, the multipliers with a high conversion gain required in the loop are not available for RF signals.

Therefore, this chapter focuses on the practical perspective of the ALMS loop. In particular, the implementation of various RF multi-tap adaptive filters for SI cancellation published in the literature is firstly reviewed. Then, a practical structure of the ALMS loop is proposed, and a prototype of the loop is implemented to provide experimental results. Contributions of this chapter are summarized as follows.

- A comprehensive review on the implementation of the state-of-the art adaptive filters for the RF domain cancellation in IBFD radios is presented.
- A practical structure of the ALMS loop for its future applications is proposed. Although adaptive filters employing the least mean square algorithm in the analog domain had been implemented as in [84, 85], they are for low frequency (lower than 1 MHz) applications only. Based on the proposed structure, a prototype of the

ALMS loop including two taps in an IBFD system at the carrier frequency of 2.4 GHz is implemented.

- For the first time, experimental results are provided to validate the theoretical analyses in our previous publications. Measured results show that 39 dB and 33 dB of SI mitigation can be achieved by the prototype in the system with 20 MHz and 50 MHz bandwidths, respectively. From the parameters of the components used in the prototype, the level of cancellation can be verified by the analytical formula of interference suppression ratio provided in [61]. Considering the degradation factor given in [81], the practical results agree with the theoretical ones. The level of cancellation is also measured with different roll-off factors of the pulse shaping filter to confirm the analyses shown in [59]. Finally, the prototype is evaluated with a 20 MHz-bandwidth OFDM signal to confirm that the ALMS loop works well in both single-carrier and multi-carrier signaling systems as mentioned in [58, 59, 81].

The remainder of this chapter is organized as follows. Section 7.2 reviews some related works. In Section 7.3, the practical structure of the ALMS loop is proposed, and the implementation of the prototype using off-the-shelf components is described. In Section 7.4, experimental results are presented. Finally, Section 7.5 concludes the chapter.

7.2 Related Works

7.2.1 Analog Multi-Tap Adaptive Filters

As indicated in the introduction, the RF domain cancellation is an essential step to mitigate the SI. The authors in [10] pointed out that among different approaches in the RF domain cancellation, multi-tap adaptive filters are able to cancel the transmit noise and nonlinear distortion components since they utilize the transmitted signal to generate the cancellation signal. A generalized structure of this approach is depicted in Fig. 7.1. Since the SI channel includes multi-paths, this approach aims to mimic the SI channel by a multi-tap structure. Each tap includes a delay line and a mechanism to independently modify the amplitude (by an attenuator) and phase (by a phase shifter) of the delayed reference signal. The outputs of all the taps are combined together before canceling the SI at the input of the receiver.

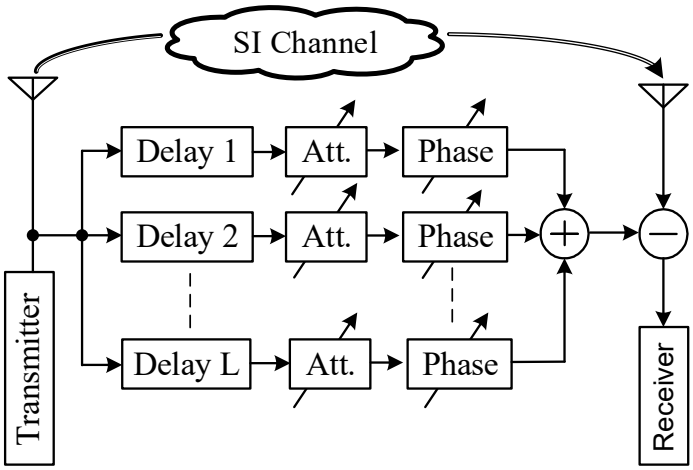

Figure 7.1: Multi-tap adaptive filter structure.

Table 7.1: Comparison of existing multi-tap adaptive filters

	# of taps	Delay line	Tap weight control	ISR (dB)	Bandwidth (MHz)
[8]	8	Microstrip trace	FPGA	45	80
[39]	2	Anaren IC	Down converter + Integrator	33	20
[38]	4	Coaxial cable	FPGA	21.6	20
[40]	8	Microstrip trace	FPGA	38	20

Although analog multi-tap adaptive filters are similar in principle, they are implemented in different ways, especially in the mechanism to tune the amplitude and phase of the reference signal. Some prototypes of analog multi-tap adaptive filters are compared in Table 7.1. This comparison focuses on the implementation aspect of these structures. The performance aspect represented by the ISR is for reference only since these prototypes are evaluated and designed for IBFD systems with different transmission bandwidths at different transmit powers. It can be seen that most of these cancellers [8, 38, 40] require DSP performed by FPGA to synthesize the weighting coefficients for the tuning mechanism. The authors in [39] employed down-converters to calculate the weighting coefficients in the baseband by integrator. In addition, the delay line can be implemented by either integrated circuits (IC) [39], microstrip traces [8, 40], or coaxial cables [38]. One advantage of the IC delay line is that it can provide a long delay time comparable to microstrip traces and coaxial cables in a compact size. It is also worth noting that, with

Table 7.2: Summary of publications on ALMS loops

	Signalling	Findings	Methods
[9]	single-carrier	ISR vs. loop gain & β	Cyclostationary & stationary
[58]	Multi-carrier	ISR vs. windowing function	Cyclostationary & stationary
[59]	Single & multi-carrier	ISRLB vs. β	Cyclostationary
[67]	Chirp signal	Tap delay design for deterministic signal	Stationary
[61]	single-carrier	ISRLB in analog and digital domains	Stationary
[81]	Single & multi-carrier	Degradation factor vs. I/Q imbalance	Stationary

only two taps, the level of RF domain cancellation can reach 33 dB in a 20 MHz IBFD system as in [39].

7.2.2 ALMS Loop

Table 7.2 summarizes some publications on the ALMS loop. In [9], the ALMS loop is firstly introduced and its performance related to the loop gain and the roll-off factor β of the pulse shaping filter is presented through cyclostationary and stationary analyses. Then, the performance of the ALMS loop with different transmitted signal properties is analyzed in [58, 59, 67]. Furthermore, in [61], the loop gain, roll-off factor, tap delay and number of taps are all considered. It is shown that when LT_d is sufficiently large, the level of cancellation will approach an ISRLB, defined as the lower bound of the ratio between the residual SI power after cancellation and the SI power without cancellation and given by

$$ISRLB = \frac{1+\beta(\sqrt{a+1}-1)}{(1+a)^2} \tag{7.1}$$

where $a = \mu \frac{V_X^2}{K_1 K_2} \frac{T_s}{T_d}$ and β is the roll-off factor of the pulse shaping filter. From (7.1), it is seen that high-gain multipliers are generally required to achieve the lower ISRLB. Finally, the impacts of in-phase/quadrature (I/Q) imbalances of the quadrature multipliers on the level of cancellation are evaluated in [81]. In particular, a degradation factor of the level of cancellation caused by I/Q imbalances is determined over a range of amplitude and phase errors of the quadrature multipliers.

However, all these findings are only based on theoretical analyses and verified by simulations in MATLAB. A prototype, therefore, is necessary to obtain practical results to validate these theoretical findings. In the next section, a practical structure of the ALMS loop is proposed using discrete components.

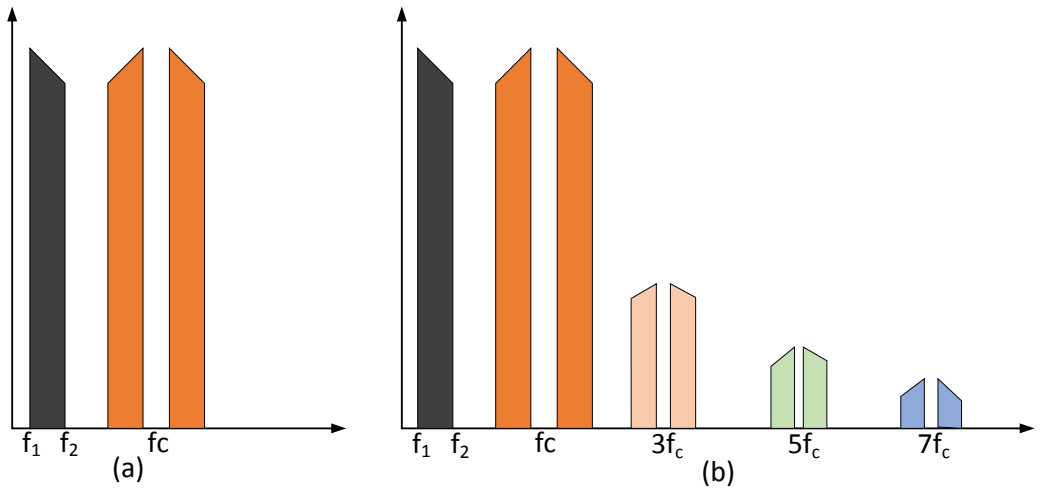

Figure 7.2: Output spectra of (a) a multiplier or a modulator with an LPF and (b) an unfiltered modulator.

7.3 Implementation of ALMS loop

Although the ALMS loop structure is simple, it is still challenging to be implemented using off-the-shelf components. In particular, the high-gain quadrature multipliers in the ALMS loop are unavailable in the RF range. Therefore, quadrature demodulators and modulators combined with amplifiers are adopted to replace the ideal multipliers. However, this replacement faces some new problems. Firstly, unlike an ideal multiplier which can accept any signal in its frequency range, a modulator/demodulator normally requires a single tone with a stable amplitude as a local oscillation (LO) signal. In addition, the multipliers in the ALMS loop are assumed to have a high conversion gain, which is not normally applicable to modulators/demodulators. Therefore, when a modulator and a demodulator are used in the ALMS loop, the reference signal should be provided to their LO ports. Then, a variable gain amplifier is used at these ports to ensure an adequate level of the LO signal. The low conversion gain of the modulator/demodulator can be compensated by an amplifier after combining all the outputs of the taps. Another problem is that, while a multiplier is a linear device, a modulator/demodulator is nonlinear [86]. This means the output of the latter includes some odd harmonics of the carrier frequency as shown in Fig. 7.2(b). If an LPF is used following the modulator/demodulator, these harmonics can be removed and the modulator/demodulator can produce the same output spectrum as that of an ideal multiplier as shown in Fig. 7.2(a) [86]. In the structure of the ALMS loop (cf. Fig. 2.9), the LPFs are not only used to synthesize the weighting coefficients, but also eliminate the odd harmonics at the output of the demodulator. As

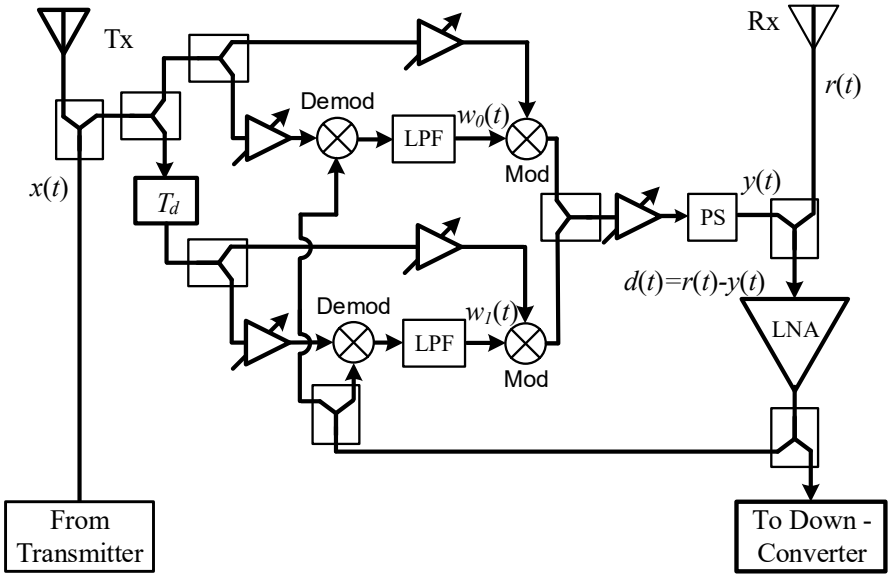

Figure 7.3: A practical structure of the ALMS loop.

for the modulator, since its output will be amplified by an amplifier, the harmonics at the output of the modulator will also be attenuated if the cut-off frequency of this amplifier is suitably selected (see Section 7.3 for more details).

As can be seen in Fig. 2.9, many power splitters are required to split and combine signals. Therefore, Wilkinson dividers are used for both splitters and combiners. The subtractor at the input of the receiver can also be implemented by a Wilkinson divider with a phase shifter, which makes an 180 degree phase shift to the cancellation signal. However, one problem with the Wilkinson divider is that it is a lossy component. Hence, a variable gain amplifier should be used at the input of the RF port of each demodulator to compensate this loss.

The implementation structure of a 2-tap ALMS loop is presented in Fig. 7.3. Due to the presence of the aforementioned extra components, the loop gain of this structure now can be calculated as

$$G = \mu \frac{V_{LO}^2}{K_1 K_2} G_O \tag{7.2}$$

where V_{LO} is the root-mean square amplitude of the reference signal at the LO ports of the modulators and demodulators and G_O is the power gain of the amplifier at the output of the cancellation circuit after compensating the losses of the phase shifter and the power combiner. Therefore, the interference suppression ratio, denoted as ISR, given

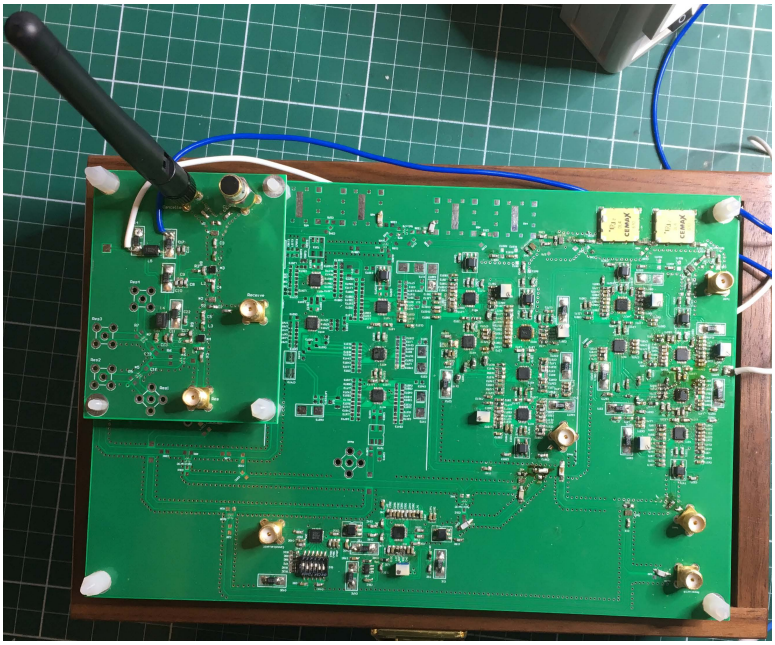

Figure 7.4: Prototype of the ALMS loop and a part of the receiver.

by the prototype can be expected to be

$$ISR \leq \frac{(1+a')^2}{1+\beta(\sqrt{a'+1}-1)} \tag{7.3}$$

where $a' = G\frac{T_s}{T_d}$. Note that ISR here is defined as the ratio between the power of the SI without cancellation and that of the residual SI after cancellation.

The prototype of the ALMS loop is designed and fabricated on Roger 4350B printed circuit board material with all surface mount devices as shown in Fig. 7.4. Since this prototype is implemented to demonstrate the ALMS loop and validate the theoretical results, it is designed in a versatile form so that it can have one to four taps. The amount of delay for each tap can also be changed by cascading multiple delay lines. Therefore, the size of the prototype is 20 cm × 13 cm. In fact, when the ALMS loop is optimized for a specific IBFD system, its size will be much smaller. The dimension of the ALMS loop can be further minimized if it is manufactured in an analog IC.

Detailed descriptions of the components in the ALMS loop are provided as follows. The delay line of the second tap is chosen as $T_d = 4$ ns (DL4 RN2 Technologies). In each tap, the demodulator (Analog Devices ADL5382) and the modulator (ADL5373) are selected for the first and the second multiplier pairs, respectively, because they both have a quadrature structure with differential outputs/inputs for the ease of interfacing. In addition, these components have a very small level of I/Q imbalances, which are less than

0.3 degree in phase imbalance and 0.07 dB in amplitude imbalance. Therefore, according to [81], the level of cancellation will be only degraded by about 0.3 dB (cf. Fig. 6 in [81]). Both ADL5382 and ADL5373 require a 0 dBm LO signal so that V_{LO} is calculated as

$$V_{LO} = \sqrt{2P_{LO}R} = \sqrt{2 \times 10^{(0+17-30)/10}} = 0.3166 \text{ V}, \tag{7.4}$$

where 17 dB is added to convert the power with a 50 Ohm load to that of an 1 Ohm load. From the ADL5382 datasheet, its conversion gain is 3.5 dB at 2.4 GHz if $P_{LO} = 0$ dBm. Since the conversion gain is defined by the ratio between the output power and the input power at the RF port, the dimensional constant K_1 can be calculated as $K_1 = 0.3166/10^{(3.5/20)} = 0.2116$ V. In case of ADL5373, the output power will be 5 dBm if the baseband input voltage is 1.4 V and $P_{LO} = 0$ dBm. Therefore, K_2 is found as

$$K_2 = \frac{1.4 \times 0.3166}{\sqrt{2 \times 10^{(5+17-30)/10}}} = 0.7873 \text{ V} \tag{7.5}$$

All the power splitters/combiners are Anaren PD2328J5050S2HF which have only 0.5 dB insertion loss. The phase shifter MACOM MAPS-010143 is used along with a power combiner to form the subtractor. The variable gain amplifier (VGA Analog Devices ADL5330) is used since its gain can be changed by a controlled voltage which is adjusted by a potentiometer. In addition, the operating frequency of this VGA is from 10 MHz to 3 GHz only, thus the odd harmonics at the outputs of modulators will be attenuated. The ADL5330 at the output of the cancellation circuit is set to have a 22 dB gain. Due to the losses caused by the power combiner (0.5 dB) and the phase shifter (4.5 dB), G_O is 17 dB.

Fig. 7.4 also shows a part of the receiver including the power combiner of the subtractor and a LNA (MACOM MAAL - 011078), which can provide a 22 dB gain at 2.4 GHz. After the LNA, a power divider is used to provide the loop-back signal and the residual SI signal for measurements. Since the power splitter causes a 0.5 dB loss at each output, the LNA gain in the loop is 21.5 dB, i.e., $\mu = 5.9425$. From these parameters and Eq. (7.2), the loop gain of the prototype can be determined as $G = 20.1$, or 26.06 dB.

7.4 Measurement Results

7.4.1 Measurement Setup

In order to evaluate the performance of the prototype, a measurement setup is built as shown in Fig. 7.5. An arbitrary waveform generator (Keysight M8190A) is used as a transmitter. Since one channel of the M8190A has two outputs which can generate the

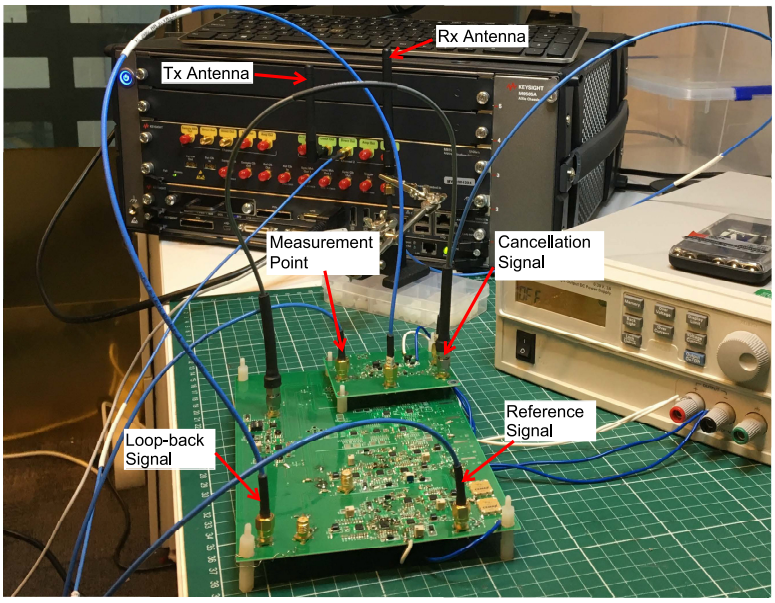

Figure 7.5: The measurement setup.

same signals, one of them can be used for the transmitter, and the other is used for the reference signal. In all the tests, the transmitted signal is configured at 2.4 GHz carrier frequency and set at the highest power level of -7.75 dBm. A 2.4 GHz rod antenna is connected directly to one output of M8190A while the other port provides the reference signal for the cancellation circuit. The receive antenna is located at a distance of 75 mm to the transmit antenna. Since the cancellation circuit and the receiver are not electromagnetically shielded, they are located away from the transmitter to reduce the interference to their microstrip lines.

The signal from the receive antenna is connected to one port of the power combiner, while the cancellation signal is connected to the other port. After subtraction, the residual signal is amplified by the LNA and fed into a power splitter, which provides the loop-back signal to the cancellation circuit. The other port of the power splitter is connected to the signal analyzer (Keysight PXA N9030A) for measurements.

7.4.2 Measurement Results

7.4.2.1 Measurement with different bandwidths

The level of cancellation given by the prototype is evaluated using the transmitted signals with different bandwidths in the single-carrier IBFD system. Transmitted data is modulated with quadrature phase shift keying (QPSK) and then filtered by the RRC

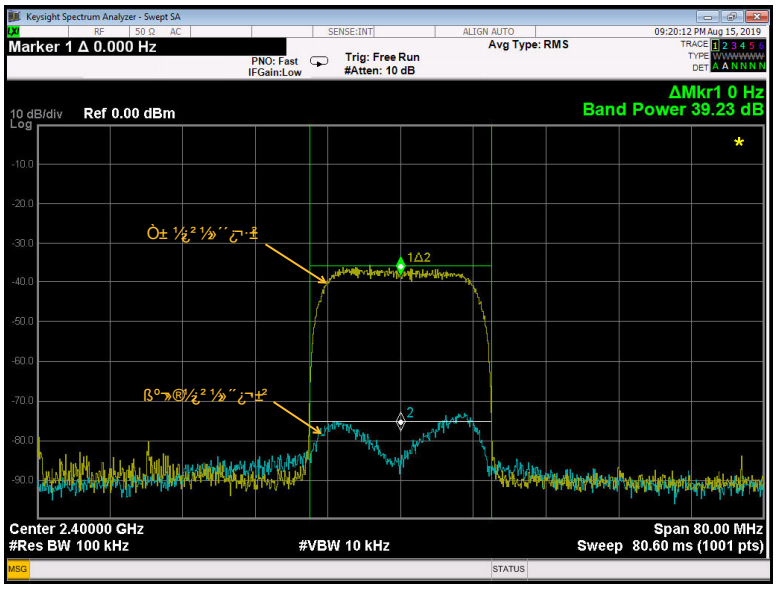

Figure 7.6: Measurement results for 20 MHz bandwidth.

pulse shaping filter before up-converted to the RF frequency. The first measurement is conducted with a 20 MHz transmit signal in which the data symbol period is set to $T_s = 62.5$ ns (i.e., $\beta = 0.25$). Fig. 7.6 shows the level of cancellation given by the prototype in this case. Marker 1 indicates the difference between the signal power in 20 MHz bandwidth measured at 2.4 GHz of Trace 1 and that of Trace 2. Clearly, a cancellation level of 39.23 dB is achieved by the prototype. In the second measurement, the transmitter is set to 50 MHz bandwidth, i.e., $T_s = 25$ ns and $\beta = 0.25$. The results of this test are depicted in Fig. 7.7. It is seen that a cancellation level of 39.23 dB is achieved in this case.

These experimental results can be used to validate the theoretical results presented in [61] and [81]. Given the symbol period, the parameter a' is determined as 314.06 and 125.625 in the 20 MHz and 50 MHz systems, respectively. Hence, the maximum levels of ISR expected by the ALMS loop calculated from Eq. (7.3) in these two cases are 42.82 dB and 36.53 dB, respectively. Considering I/Q imbalances of the demodulators and modulators, the maximum levels of cancellation will degrade by about 0.3 dB [81], i.e., 42.52 dB and 36.23 dB, respectively. This means that the level of cancellation achieved in the prototype is about 3 dB lower than these analytical maximum levels. This is justifiable because the maximum level of cancellation can only be achieved when the number of taps and tap delay in the loop satisfy the condition that LT_d covers the maximum path delay of the SI channel.

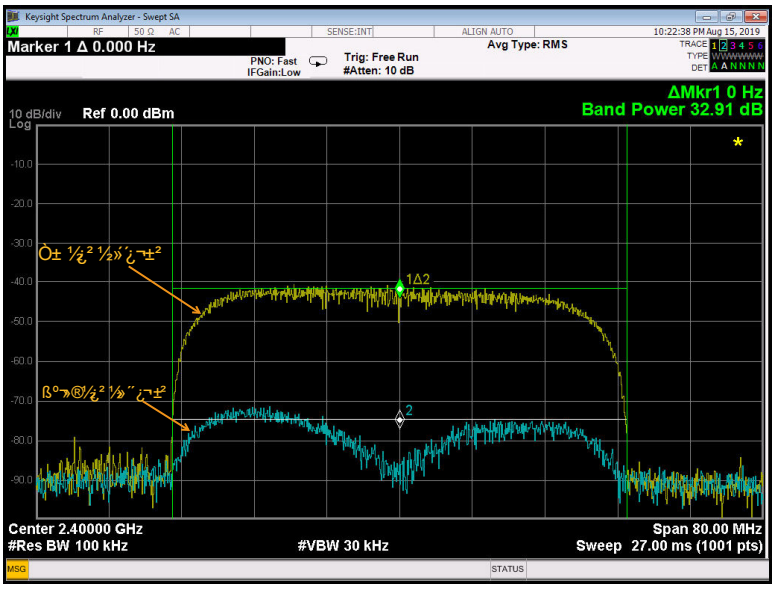

Figure 7.7: Measurement results for 50 MHz bandwidth.

7.4.2.2 Measurement with Different Signal Properties

In this test, the effect of transmitted signal spectrum on the ALMS loop performance is evaluated. Firstly, the roll-off factor of the pulse shaping filter in the transmitter is configured with different values while the symbol period of the transmit data is fixed at $T_s = 62.5$ ns. Fig. 7.8 depicts the results of the third test. Measurement results show that the level of cancellation is 39.23 dB, 38.10 dB, and 37.0 dB when the roll-off factor is 0.25, 0.5, and 0.75, respectively. The decrease of ISR with the increased roll-off factor confirms the analyses shown in [61] and [59].

In the last test, the performance of the ALMS loop with a multi-carrier signal is considered. The transmitter is configured to transmit the OFDM signal based on the IEEE 802.11 a/g format over a bandwidth of 20 MHz. As shown in Fig. 7.9, the level of cancellation in this case is also about 39 dB, which is the same as that in the single-carrier system. It means that the ALMS loop works well with both single-carrier and multi-carrier signalling schemes as concluded in [58, 59, 81].

7.5 Conclusion

This chapter presents a practical structure and implementation of the ALMS loop using off-the-shelf components. The measurement results show that 39.23 dB and 32.91 dB

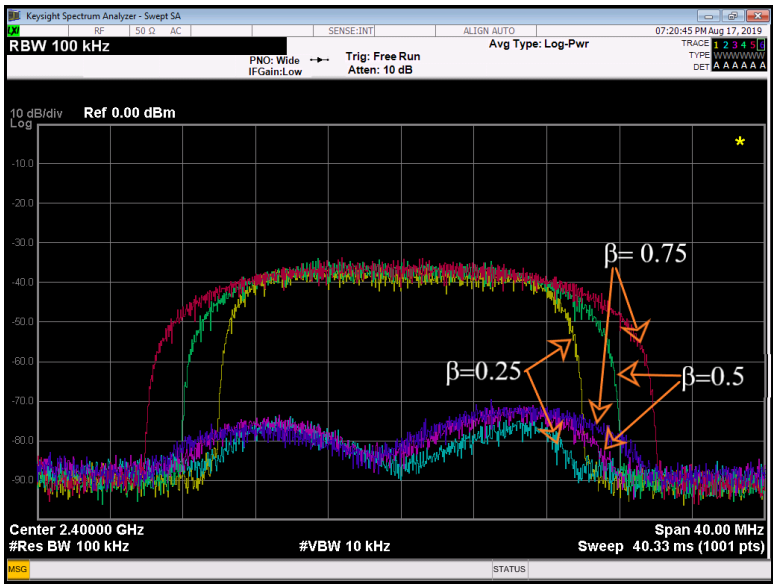

Figure 7.8: Cancellation performances with different roll-off factors.

Figure 7.9: Cancellation performances with OFDM signal.

of SI mitigations can be achieved by the prototype for IBFD systems with 20 MHz and 50 MHz bandwidths, respectively. The experimental results with different values of the roll-off factor of the transmit pulse shaping filter also prove that the level of cancellation is affected by the roll-off factor of the pulse shaping filter as analyzed in our previous publications. Finally, the experiment with the IEEE 802.11 a/g OFDM signal proves that the ALMS loop performs well with both single-carrier and multi-carrier signalling

schemes. The proposed ALMS loop implementation structure provides a useful practical solution for IBFD communication applications.

CHAPTER 8

CONCLUSION AND FUTURE WORK

8.1 Conclusion

In-band full-duplex transmission is one of the key technologies for future wireless communications due to its great advantages in doubling throughput, avoiding collisions, and reducing round-trip latency. A fundamental problem of IBFD systems is SI which prevents the receiver from the signal of interest. To mitigate the SI to below the level of noise floor, numerous approaches have been proposed in three stages namely propagation, RF, and digital domains. Among them, ALMS loop is a promising structure to cancel the SI in the RF domain without any requirements of DSP and CSI.

This research aims at adopting the ALMS loop for any IBFD systems. Therefore, the impact of transmitted signal properties has firstly investigated in Chapter 3. It has shown that the ALMS loop can work with both single-carrier and multi-carrier signallings. By applying cyclostationary analysis, it has realized that the weighting error function will not converge to a stable value but it always varies in a range which depends on the loop gain, the roll-of factor of the transmit pulse shaping and the symbol duration. Due to this variation, the interference will not be canceled completely, but there exist an irreducible interference. Therefore, under the same condition of the ALMS loop, the SI can be potentially canceled to a lower level compare to that in OFDM systems. The reason is that the symbol duration in single-carrier system is much smaller than that in the multi-carrier counterpart. In addition, the ALMS loop can work with both random bearing signals as in communication systems and deterministic signals in SAR systems.

A design suggestion is provided for the case of deterministic signals. The work conducted in Chapter 3 is published in my journal publication [5] and conference publications [8,9].

This thesis also successfully characterizes the behavior of the ALMS loop in the frequency domain by applying eigenvalue decomposition. The property of the ALMS loop in amplifying the high frequency components at the edge of the residual SI spectrum is revealed in the RF domain. However, the peaks of the residual SI spectrum will be removed by the matched filter so that the level of cancellation will be much higher when considered in the digital domain. Furthermore, this analysis also leads to the derivation of the interference suppression ratio lower bounds in both RF and digital domains. This is an essential tool to estimate the level of cancellation given by the ALMS loop from its parameters. The work conducted in Chapter 4 is published as listed in my journal publication [4].

The problem of I/Q imbalance in the structure of the ALMS loop is considered in Chapter 5. By incorporating the amplitude and phase errors of the quadrature multipliers into the signal models, the impact of I/Q imbalances on the loop gain has been determined and compensated by adjusting the gain at other point of the loop. However, even the loop gain is compensated, I/Q imbalance still deteriorates the cancellation performance of the ALMS loop which can represented by a degradation factor. Evaluating the degradation factor shows that the ALMS loop is robust to its frequency-independent I/Q imbalance. In addition, an upper bound of the degradation factor is derived to estimate the level of compensation should be achieved from other means of SIC. The work conducted in Chapter 5 is published as listed in my journal publication [3].

To adopt the ALMS loop for IBFD MIMO systems, a beam-based analog SIC structure has been proposed to significantly reduce the hardware complexity from a square number of Tx antennas (assumed to be equal to that of Rx antennas) to linear scaled number of Tx beams. The fundamental of this structure is that the SI at each Rx antenna can be seen as a linear transformation of the beam signal. Hence, the cancellation signal generated by adaptive filters is another transformation of the same source. As a result, the number of adaptive filters at each receiver chain is reduced to the number of Tx beams. In addition, two ways of generating the reference signals for the adaptive filters have been presented. The first way is employing additional Tx chains to up-convert the beam data into RF reference signals. The second way is choosing them from available Tx signals.A novel selection algorithm is proposed for the second way to avoid increasing hardware complexity in the first way. The work conducted in Chapter 6 is published as listed in my journal publication [1] and conference publication [7].

Finally, a practical structure of the ALMS loop is proposed in Chapter 7 to overcome the challenges in implementation of the ALMS loop using off-the-shelf components. A prototype with two taps is then developed based on the proposed structure to obtain some experimental results. Firstly, the levels of cancellation achieved by the prototype in IBFD systems with 20 MHz and 50 MHz bandwidths are about 39 dB and 33 dB, respectively which are justifiable with the theoretical values calculated from the formulae provided in Chapter 4 and Chapter 5. Then, the experiments with different roll-off factors of the pulse shaping filter and an OFDM signal confirm the analyses in Chapter 3. The work conducted in Chapter 7 is published as listed in my journal publication [2] and conference publication [6].

Through this study, it is concluded that the ALMS loop can be applied for any IBFD systems. The estimation tools obtained through theoretical analyses are critical for system design while the practical structure can be a reference for future implementations of the ALMS loop.

8.2 Future Work

This study has proved the potential applications of the ALMS loop for SIC in various IBFD systems. Future research directions may include developing complete IBFD systems and adopting the ALMS loop for other applications.

To develop a complete IBFD system, several research problems will need to be tackled. Firstly, the noise performance of the ALMS loop should be investigated. This thesis focuses on the achievable level of cancellation given by the ALMS loop in different scenarios. Since signal to noise ratio is crucial for all receivers, evaluating the noise properties of the ALMS loop is necessary to design the receiver. Secondly, to sufficiently mitigate the SI power to below the level of noise floor, a combination of the ALMS loop with other approaches in the propagation domain and the digital domain should be studied. Thirdly, prototyping a complete IBFD single antenna system with a wider bandwidth and a higher transmit power should also be considered. Fourthly, future works will be the consideration of SIC for IBFD hybrid beamforming MIMO systems and derivation of an optimal precoding matrix that enhances both SIC and beamforming performance. Additionally, the behaviors of the ALMS loop in IBFD MIMO systems with different transmitted baseband signals may also investigated, such as those proposed in [87, 88], and with different wireless network topologies [89, 90]. Finally, to minimize the physical size and increase the potential applications of the ALMS loop, an integrated

circuit form of the ALMS loop should be developed.

Another research direction is to adopt the ALMS loop for other applications. Since the ALMS loop is an adaptive filter which is purely implemented in the RF domain, it can potentially be applied in applications which require adaptive processing in the RF front-end. In that case, the structure of the ALMS loop may be adjusted to suit with the target requirements.

APPENDIX A

APPENDIX

A.1 Proof of Constant $E_h\{H(e^{j\omega_k})\}$

For SI channels with independent and zero-mean tap coefficients, it can be proved that $E_h\{H(e^{j\omega_k})\}$ is a constant for all $k = 0, 1, \ldots, L-1$ as follow.

$$E_h\{|H(e^{j\omega_k})|^2\} = E_h\left\{\sum_{l=0}^{L-1} h_l e^{\frac{-j2\pi kl}{L}} \sum_{l'=0}^{L-1} h_{l'}^* e^{\frac{j2\pi kl'}{L}}\right\} = \sum_{l=0}^{L-1}\sum_{l'=0}^{L-1} E_h\{h_l h_{l'}^*\} e^{\frac{-j2\pi k(l-l')}{L}}. \quad \text{(A.1)}$$

Since the SI channel tap coefficients are independent with zero-mean, $E_h\{h_l h_{l'}^*\} = 0$ for $l \neq l'$. Therefore, $E_h\{|H(e^{j\omega_k})|^2\} = \sum_{l=0}^{L-1} E_h\{|h_l|^2\}$ for all $k = 0, 1, \ldots, L-1$ which is the mean power of the SI channel.

A.2 Derivation of $ISRLB_a$ and $ISRLB_d$

A.2.1 $ISRLB_a$

From $\int_{-\frac{1+\beta}{2T_s}}^{\frac{1+\beta}{2T_s}} P(f)df = 1$ and $T_d \leq \frac{T_s}{1+\beta}$, (4.29) can be simplified as

$$ISRLB_a = \frac{\int_{-1/2T_d}^{1/2T_d} \frac{A^2 P(f)}{\left[1+\mu\frac{A^2}{T_d}P(f)\right]^2} df}{\int_{-1/2T_d}^{1/2T_d} A^2 P(f) df} = 2\int_0^{\frac{1+\beta}{2T_s}} \frac{P(f)}{\left[1+\mu\frac{A^2}{T_d}P(f)\right]^2} df. \quad \text{(A.2)}$$

Substituting $P(f)$ from (4.22) into (A.2), we have

$$\begin{aligned}\int_0^{\frac{1+\beta}{2T_s}} \frac{P(f)}{\left[1+\frac{\mu A^2}{T_d}P(f)\right]^2}df &= \int_0^{\frac{1-\beta}{2T_s}} \frac{T_s}{\left[1+\mu A^2\frac{T_s}{T_d}\right]^2}df \\ &+ \int_{\frac{1-\beta}{2T_s}}^{\frac{1+\beta}{2T_s}} \frac{\frac{T_s}{2}\left[1+\cos\left(\frac{\pi T_s}{\beta}(f-\frac{1-\beta}{2T_s})\right)\right]}{\left\{1+\mu A^2\frac{T_s}{2T_d}\left[1+\cos\left(\frac{\pi T_s}{\beta}(f-\frac{1-\beta}{2T_s})\right)\right]\right\}^2}df.\end{aligned} \tag{A.3}$$

Denoting $a=\mu A^2\frac{T_s}{T_d}$ and $x=\frac{\pi T_s}{\beta}(f-\frac{1-\beta}{2T_s})$, (A.3) becomes

$$\int_0^{\frac{1+\beta}{2T_s}} \frac{P(f)}{\left[1+\frac{\mu A^2}{T_d}P(f)\right]^2}df = \frac{1-\beta}{2(1+a)^2}+\frac{\beta}{\pi}\int_0^{\pi}\frac{\frac{1}{2}(1+\cos x)}{\left[1+\frac{a}{2}(1+\cos x)\right]^2}dx. \tag{A.4}$$

Defining $t=\tan(x/2)$ so that $\cos x=\frac{1-t^2}{1+t^2}$ and $dx=\frac{2dt}{1+t^2}$, we have

$$\begin{aligned}\int_0^{\pi}\frac{\frac{1}{2}(1+\cos x)}{\left[1+\frac{a}{2}(1+\cos x)\right]^2}dx &= 2\int_0^{\infty}\frac{1}{(t^2+a+1)^2}dt \\ &= \frac{2\sqrt{a+1}}{(a+1)^2}\int_0^{\infty}\frac{1}{\left[(\frac{t}{\sqrt{a+1}})^2+1\right]^2}d(\frac{t}{\sqrt{a+1}}) \\ &= \frac{\pi}{2}\frac{\sqrt{a+1}}{(a+1)^2}.\end{aligned} \tag{A.5}$$

Substituting (A.5) into (A.4), the $ISRLB_a$ is obtained as in (4.31).

A.2.2 $ISRLB_d$

Following the same steps as above, $ISRLB_d$ is derived as

$$\begin{aligned}ISRLB_d &= \frac{\int_{-1/2T_d}^{1/2T_d}\frac{A^2P^2(f)}{\left[1+\mu\frac{A^2}{T_d}P(f)\right]^2}df}{\int_{-1/2T_d}^{1/2T_d}A^2P^2(f)df} \\ &= \frac{\int_0^{\frac{1+\beta}{2T_s}}\frac{P^2(f)}{\left[1+\mu\frac{A^2}{T_d}P(f)\right]^2}df}{\int_0^{\frac{1+\beta}{2T_s}}P^2(f)df}.\end{aligned} \tag{A.6}$$

Substituting $P(f)$ from (4.22) into (A.6) as well as applying the substitution of $x = \frac{\pi T_s}{\beta}(f - \frac{1-\beta}{2T_s})$ and then $t = \tan(x/2)$, we have

$$\begin{aligned}\int_0^{\frac{1+\beta}{2T_s}} \frac{P^2(f)}{\left[1+aP(f)\right]^2} df &= \frac{T_s(1-\beta)}{2(1+a)^2} + \frac{T_s\beta}{\pi}\int_0^{\pi} \frac{\frac{1}{4}(1+\cos x)^2}{\left[1+\frac{a}{2}(1+\cos x)\right]^2} dx \\ &= \frac{T_s(1-\beta)}{2(1+a)^2} + \frac{T_s\beta}{\pi}\int_0^{\infty} \frac{\frac{1}{(1+t^2)^2}}{(1+a\frac{1}{1+t^2})^2}\frac{2}{1+t^2} dt \\ &= \frac{T_s(1-\beta)}{2(1+a)^2} + \frac{T_s\beta}{\pi}\int_0^{\infty} \frac{2}{(t^2+a+1)^2(t^2+1)} dt.\end{aligned} \tag{A.7}$$

Note that $\frac{2}{(t^2+a+1)^2(t^2+1)}$ can be split as

$$\frac{2}{(t^2+a+1)^2(t^2+1)} = \frac{2}{a^2}\left[\frac{1}{(1+t^2)} - \frac{1}{(t^2+a+1)} - \frac{a}{(t^2+a+1)^2}\right]. \tag{A.8}$$

Therefore, by substituting (A.8) into (A.7), we obtain

$$\begin{aligned}\int_0^{\frac{1+\beta}{2T_s}} \frac{P^2(f)}{(1+aP(f))^2} df &= \frac{T_s(1-\beta)}{2(1+a)^2} + \frac{T_s\beta}{\pi}\frac{\pi}{a^2}\left[1 - \frac{1}{\sqrt{a+1}} - \frac{a\sqrt{a+1}}{2(a+1)^2}\right] \\ &= \frac{T_s}{2(1+a)^2}\left\{1+\beta\left[\frac{2(a+1)^2}{a^2}\left(1 - \frac{1}{\sqrt{a+1}} - \frac{a\sqrt{a+1}}{2(a+1)^2}\right) - 1\right]\right\}.\end{aligned} \tag{A.9}$$

The derivation of $\int_0^{\frac{1+\beta}{2T_s}} P^2(f)df$ is expressed as

$$\begin{aligned}\int_0^{\frac{1+\beta}{2T_s}} P^2(f)df &= T_s\frac{1-\beta}{2} + \frac{T_s\beta}{4\pi}\int_0^{\pi}(1+\cos x)^2 dx \\ &= \frac{T_s}{2}(1-\beta/4).\end{aligned} \tag{A.10}$$

From (A.9) and (A.10), $ISRLB_d$ is obtained as in (4.32).

A.3 Derivation of Residual SI Power

Substituting (5.17) into (5.18), we have

$$\begin{aligned}
P_d(t) &= \frac{1}{K_1K_2}\bar{E}\left\{\left|\mathrm{Re}\left\{\sum_{l=0}^{L-1} u_l^*(t)X(t-lT_d)e^{j2\pi f_c t}\right\}\right|^2\right\} \\
&= \frac{1}{4K_1K_2}\bar{E}\left\{\left[\sum_{l=0}^{L-1} u_l^*(t)X(t-lT_d)e^{j2\pi f_c t} + \sum_{l=0}^{L-1} u_l(t)X^*(t-lT_d)e^{-j2\pi f_c t}\right]\right. \\
&\left.\cdot\left[\sum_{l'=0}^{L-1} u_{l'}(t)X^*(t-l'T_d)e^{-j2\pi f_c t} + \sum_{l'=0}^{L-1} u_{l'}^*(t)X(t-l'T_d)e^{j2\pi f_c t}\right]\right\} \\
&= \frac{1}{2}\sum_{l=0}^{L-1}\sum_{l'=0,l'\neq l}^{L-1} \bar{u}_l^*(t)\Theta((l-l')T_d)\bar{u}_{l'}(t) + \frac{1}{2}\Theta(0)\sum_{l=0}^{L-1}\bar{E}\left\{|u_l(t)|^2\right\} \\
&+ \frac{1}{2K_1K_2}\bar{E}\left\{\mathrm{Re}\left[\sum_{l=0}^{L-1} u_l^*(t)X(t-lT_d)\sum_{l'=0}^{L-1} u_{l'}^*(t)X(t-l'T_d)e^{j4\pi f_c t}\right]\right\}.
\end{aligned} \tag{A.11}$$

Further assuming that the L paths of the SI channel are independent and hence, $u_l(t)$ and $u_{l'}(t)$ can be considered to be independent for $l \neq l'$, (A.11) becomes

$$\begin{aligned}
P_d(t) &= \frac{1}{2}\sum_{l=0}^{L-1}\sum_{l'=0,l'\neq l}^{L-1} \bar{u}_l^*(t)\Theta((l-l')T_d)\bar{u}_{l'}(t) + \frac{1}{2}\Theta(0)\sum_{l=0}^{L-1}\bar{E}\left\{\left|u_l(t)\right|^2\right\} \\
&+ \frac{1}{2K_1K_2}\bar{E}\left\{Re\left[\sum_{l=0}^{L-1}(u_l^*(t))^2X^2(t-lT_d)\right]\right\}.
\end{aligned} \tag{A.12}$$

Since $E\{X^2\} = 0$ for any zero mean complex random process X, we have

$$\bar{E}\left\{\mathrm{Re}\left[\sum_{l=0}^{L-1}(u_l^*(t))^2X^2(t-lT_d)\right]\right\} = 0.$$

In addition, from the fact that $E\{|X|^2\} \geq |E\{X\}|^2$ for any random process X, hence $\bar{E}\{|u_l(t)|^2\} \geq |\bar{u}_l(t)|^2$. Therefore,

$$\begin{aligned}
P_d(t) &\geq \frac{1}{2}\sum_{l=0}^{L-1}\sum_{l'=0,l'\neq l}^{L-1} \bar{u}_l^*(t)\Theta((l-l')T_d)\bar{u}_{l'}(t) + \frac{1}{2}\Theta(0)\sum_{l=0}^{L-1}|\bar{u}_l(t)|^2 \\
&= \frac{1}{2}\sum_{l=0}^{L-1}\sum_{l'=0}^{L-1} \bar{u}_l^*(t)\Theta((l-l')T_d)\bar{u}_{l'}(t).
\end{aligned} \tag{A.13}$$

It is also worth noting that the equality happens when $t \to \infty$ as $u_l(t)$ converges to its steady-state value as shown in [9, Eq. (30) and Eq. (35)]. Hence, by letting $t \to \infty$, we obtain the steady-state P_d as in (6.20).

A.4 Solution of Steady-State Weighting Error Function

Following the steps presented in [9, 61, 67] to derive the weighting error functions, and substituting the models of $r(t), y(t), x_1(t),$ and $x_2(t)$ into (5.6), we have the expression of $w_l(t)$ as

$$
\begin{aligned}
w_l(t+t_0) = & \\
& \frac{2\mu\alpha}{K_1K_2}\int_{t_0}^{t+t_0} e^{-\alpha(t+t_0-\tau)}\Big\{\frac{1}{2}\Big(\big[Z(\tau)+S(\tau)+N(\tau)\big]e^{j2\pi f_c t}+\big[Z^*(\tau)+S^*(\tau)+N^*(\tau)\big]e^{-j2\pi f_c t}\Big) \\
& -\frac{1}{2}\Big(\sum_{l'=0}^{L-1} w_{l'}^*(t)\big[\eta_2 X(t-l'T_d)e^{j2\pi f_c(t-l'T_d)}+\xi_2 X^*(t-l'T_d)e^{-j2\pi f_c(t-l'T_d)}\big] \\
& +\sum_{l'=0}^{L-1} w_{l'}(t)\big[\eta_2^* X^*(t-l'T_d)e^{-j2\pi f_c(t-l'T_d)}+\xi_2^* X(t-l'T_d)e^{j2\pi f_c(t-l'T_d)}\big]\Big)\Big\} \\
& \cdot\Big[\eta_1 X(\tau-lT_d)e^{j2\pi f_c(\tau-lT_d)}+\xi_1 X^*(\tau-lT_d)e^{-j2\pi f_c(\tau-lT_d)}\Big]d\tau \\
& =\frac{\mu\alpha}{K_1K_2}\int_{t_0}^{t+t_0} e^{-\alpha(t+t_0-\tau)}\Big\{\Big[\sum_{l'=0}^{L-1}(h_{l'}-[\eta_2^* w_{l'}(\tau)+\xi_2 w_{l'}^*(\tau)]e^{j2\pi f_c l'T_d})^* X(\tau-l'T_d) \\
& +S(\tau)+N(\tau)\Big]e^{j2\pi f_c\tau}+\Big[\sum_{l'=0}^{L-1}(h_{l'}-[\eta_2^* w_{l'}(\tau)+\xi_2 w_{l'}^*(\tau)]e^{j2\pi f_c l'T_d})X^*(\tau-l'T_d) \\
& +S^*(\tau)+N^*(\tau)\Big]e^{-j2\pi f_c\tau}\Big\}\Big[\eta_1 X(\tau-lT_d)e^{j2\pi f_c(\tau-lT_d)}+\xi_1 X^*(\tau-lT_d)e^{-j2\pi f_c(\tau-lT_d)}\Big]d\tau.
\end{aligned}
\tag{A.14}
$$

After filtering out by the LPF, the signal components centered about frequency $2f_c$ will be eliminated. Therefore, (A.14) becomes

$$
\begin{aligned}
w_l(t+t_0) = & \frac{\mu'\alpha}{K_1K_2}\int_{t_0}^{t+t_0} e^{-\alpha(t+t_0-\tau)}\Big\{\Big[\sum_{l'=0}^{L-1} u_{l'}^*(\tau)X(\tau-l'T_d)+S(\tau)+N(\tau)\Big]\xi_1 X^*(\tau-lT_d)e^{j2\pi f_c lT_d} \\
& +\Big[\sum_{l'=0}^{L-1} u_{l'}(\tau)X^*(\tau-l'T_d)+S^*(\tau)+N^*(\tau)\Big]\eta_1 X(\tau-lT_d)e^{-j2\pi f_c lT_d}\Big\}d\tau.
\end{aligned}
\tag{A.15}
$$

Assuming that the signal of interest and the AWGN are independent of the transmitted signal, i.e., $E\{S^*(t)X(t-\tau)\}=0$ and $E\{N^*(t)X(t-\tau)\}=0$ for all τ and taking ensemble

expectation of the two sides of the above equation, we have

$$\bar{w}_l(t+t_0) = \frac{\mu'\alpha}{K_1K_2}\int_{t_0}^{t+t_0} e^{-\alpha(t+t_0-\tau)}\Big\{\Big[\sum_{l'=0}^{L-1}\bar{u}^*_{l'}(\tau)E\{X(\tau-l'T_d)X^*(\tau-lT_d)\}\Big]\xi_1 e^{j2\pi f_c lT_d} + \Big[\sum_{l'=0}^{L-1}\bar{u}_{l'}(\tau)E\{X^*(\tau-l'T_d)X(\tau-lT_d)\}\Big]\eta_1 e^{-j2\pi f_c lT_d}\Big\}d\tau \tag{A.16}$$

where $\bar{w}_l(t) = E\{w_l(t)\}$ and $\bar{u}_l(t) = E\{u_l(t)\}$. Defining $\tau' = \tau - t_0$, we have

$$\bar{w}_l(t+t_0) = \frac{\mu'\alpha}{K_1K_2}\int_0^t e^{-\alpha(t-\tau')}\Big\{\Big[\sum_{l'=0}^{L-1}\bar{u}^*_{l'}(\tau'+t_0)E\{X(\tau'+t_0-l'T_d)X^*(\tau'+t_0-lT_d)\}\Big] \cdot\xi_1 e^{j2\pi f_c lT_d} + \Big[\sum_{l'=0}^{L-1}\bar{u}_{l'}(\tau'+t_0)E\{X^*(\tau'+t_0-l'T_d)X(\tau'+t_0-lT_d)\}\Big]\eta_1 e^{-j2\pi f_c lT_d}\Big\}d\tau'. \tag{A.17}$$

Taking time average over one symbol period T of $\bar{w}_l(t+t_0)$ with respect to the starting time t_0, we obtain the ensemble and time averaged weighting coefficients as in (A.18).

$$\begin{aligned}\bar{\bar{w}}_l(t) &= \frac{1}{T}\int_0^T \bar{w}_l(t+t_0)dt_0 \\ &= \frac{\mu'\alpha}{K_1K_2T}\int_0^T\int_0^t e^{-\alpha(t-\tau')}\Big\{\Big[\sum_{l'=0}^{L-1}\bar{u}^*_{l'}(\tau'+t_0)E\{X(\tau'+t_0-l'T_d)X^*(\tau'+t_0-lT_d)\}\Big]\xi_1 e^{j2\pi f_c lT_d} \\ &+ \Big[\sum_{l'=0}^{L-1}\bar{u}_{l'}(\tau'+t_0)E\{X^*(\tau'+t_0-l'T_d)X(\tau'+t_0-lT_d)\}\Big]\eta_1 e^{-j2\pi f_c lT_d}\Big\}d\tau' dt_0.\end{aligned} \tag{A.18}$$

Since α is very small, $\bar{u}_l(t)$ changes slowly and it can be seen as a constant in one symbol period of T, i.e., $\bar{u}_l(t+t_0) \approx \bar{\bar{u}}_l(t) = \frac{1}{T}\int_0^T \bar{u}_l(t+t_0)dt_0$ which is the ensemble and time averaged weighting error function $u_l(t)$. Thus (A.18) is expressed as

$$\begin{aligned}\bar{\bar{w}}_l(t) = \mu'\alpha\int_0^t e^{-\alpha(t-\tau')}\Big\{&\Big[\sum_{l'=0}^{L-1}\bar{\bar{u}}^*_{l'}(\tau')\Theta((l'-l)T_d)\Big]\xi_1 e^{j2\pi f_c lT_d} \\ &+ \Big[\sum_{l'=0}^{L-1}\bar{\bar{u}}_{l'}(\tau')\Theta((l-l')T_d)\Big]\eta_1 e^{-j2\pi f_c lT_d}\Big\}d\tau'.\end{aligned} \tag{A.19}$$

Substituting (A.19) into the definition of the weighting error function and using the property of the normalized autocorrelation function $\Theta(\tau) = \Theta(-\tau)$, we have

$$\begin{aligned}\bar{\tilde{u}}_l(t) = h_l - \mu'\alpha \int_0^t e^{-\alpha(t-\tau)} \sum_{l'=0}^{L-1} \Theta((l-l')T_d) \\ \cdot \Big[\big(\eta_2^*\xi_1 + \eta_1^*\xi_2\big)\bar{\tilde{u}}_{l'}^*(\tau) e^{j4\pi f_c l T_d} + \big(\eta_1\eta_2^* + \xi_1^*\xi_2\big)\bar{\tilde{u}}_{l'}(\tau) \Big] d\tau\end{aligned} \tag{A.20}$$

or in the matrix form

$$\bar{\tilde{\mathbf{u}}}(t) = \mathbf{h} - \mu'\alpha \int_0^t e^{-\alpha(t-\tau)} \Big[\big(\eta_2^*\xi_1 + \eta_1^*\xi_2\big)\mathbf{E}\boldsymbol{\Theta}\bar{\tilde{\mathbf{u}}}^*(\tau) + \big(\eta_1\eta_2^* + \xi_1^*\xi_2\big)\boldsymbol{\Theta}\bar{\tilde{\mathbf{u}}}(\tau) \Big] d\tau. \tag{A.21}$$

When $t \to \infty$, $\bar{\tilde{\mathbf{u}}}(t)$ converges to its steady-state value $\bar{\tilde{\mathbf{u}}}$ so that it can be moved outside the integral in (A.21). Since $\alpha \int_0^t e^{-\alpha(t-\tau)} d\tau \Big|_{t\to\infty} \to 1$, (A.21) becomes

$$\bar{\tilde{\mathbf{u}}} = \mathbf{h} - \mu' \Big[\big(\eta_2^*\xi_1 + \eta_1^*\xi_2\big)\mathbf{E}\boldsymbol{\Theta}\bar{\tilde{\mathbf{u}}}^* + \big(\eta_1\eta_2^* + \xi_1^*\xi_2\big)\boldsymbol{\Theta}\bar{\tilde{\mathbf{u}}} \Big], \tag{A.22}$$

or

$$\big[\mathbf{I}_L + \mu'\big(\eta_1\eta_2^* + \xi_1^*\xi_2\big)\boldsymbol{\Theta}\big]\bar{\tilde{\mathbf{u}}} + \mu'\big(\eta_2^*\xi_1 + \eta_1^*\xi_2\big)\mathbf{E}\boldsymbol{\Theta}\bar{\tilde{\mathbf{u}}}^* = \mathbf{h}. \tag{A.23}$$

Taking complex conjugation on two sides of (A.23) and noting that $\boldsymbol{\Theta}^* = \boldsymbol{\Theta}$ and $\mathbf{E}^* = \mathbf{E}^{-1}$, we have

$$\big[\mathbf{I}_L + \mu'\big(\eta_1^*\eta_2 + \xi_1\xi_2^*\big)\boldsymbol{\Theta}\big]\bar{\tilde{\mathbf{u}}}^* + \mu'\big(\eta_2\xi_1^* + \eta_1\xi_2^*\big)\mathbf{E}^{-1}\boldsymbol{\Theta}\bar{\tilde{\mathbf{u}}} = \mathbf{h}^*. \tag{A.24}$$

From (A.23) and (A.24), we have a set of equations

$$\begin{cases} (\mathbf{I}_L + k_1\boldsymbol{\Theta})\bar{\tilde{\mathbf{u}}} + k_2\mathbf{E}\boldsymbol{\Theta}\bar{\tilde{\mathbf{u}}}^* = \mathbf{h} \\ k_2^*\mathbf{E}^{-1}\boldsymbol{\Theta}\bar{\tilde{\mathbf{u}}} + (\mathbf{I}_L + k_1^*\boldsymbol{\Theta})\bar{\tilde{\mathbf{u}}}^* = \mathbf{h}^* \end{cases} \tag{A.25}$$

where $k_1 = \mu'\big(\eta_1\eta_2^* + \xi_1^*\xi_2\big)$ and $k_2 = \mu'\big(\eta_2^*\xi_1 + \eta_1^*\xi_2\big)$. From the second equation in (A.25), we can expressed $\bar{\tilde{\mathbf{u}}}^*$ as

$$\bar{\tilde{\mathbf{u}}}^* = (\mathbf{I}_L + k_1^*\boldsymbol{\Theta})^{-1}\big[\mathbf{h}^* - k_2^*\mathbf{E}^{-1}\boldsymbol{\Theta}\bar{\tilde{\mathbf{u}}}\big]. \tag{A.26}$$

Substituting (A.26) into the first equation in (A.25), we obtain the solution for the weighting error functions as in (5.20).

A.5 Derivation of Modeling Error

From (6.13), we have

$$\sum_{n'=1}^{N}\int_{-\infty}^{\infty} h_{n',m}(\tau)\bar{E}\{X_n(t-lT_d)X_{n'}^*(t-\tau)\}d\tau - \sum_{n'=1}^{N}\sum_{l'=0}^{L-1} h_{n',m}(l')\bar{E}\{X_n(t-lT_d)X_{n'}^*(t-l'T_d)\} = 0 \tag{A.27}$$

for $n = 0,\ldots,N,$ and $l = 0,\ldots,L-1$. Substituting $X_n(t) = \mathbf{a}_n\mathbf{S}(t)$ where $\mathbf{a}_n = [a_{n,1},\ldots,a_{n,K}]$ is the n-th row vector of $\mathbf{A}$ into (A.27), we get

$$\begin{aligned}&\sum_{n'=1}^{N}\int_{-\infty}^{\infty} h_{n',m}(\tau)\mathbf{a}_n\bar{E}\{\mathbf{S}(t-lT_d)\mathbf{S}^H(t-\tau)\}\mathbf{a}_{n'}^H d\tau \\ &- \sum_{n'=1}^{N}\sum_{l'=0}^{L-1} h_{n',m}(l')\mathbf{a}_n\bar{E}\{\mathbf{S}(t-lT_d)\mathbf{S}^H(t-l'T_d)\}\mathbf{a}_{n'}^H\} = 0.\end{aligned} \tag{A.28}$$

From $E\{S_k(t)S_{k'}(t-\tau)\} = 0$ for $k \neq k'$, (A.28) becomes

$$\sum_{n'=1}^{N}\left[\int_{-\infty}^{\infty} h_{n',m}(\tau)\Phi(lT_d-\tau)\mathbf{a}_n\mathbf{a}_{n'}^H d\tau - \sum_{l'=0}^{L-1} h_{n',m}(l')\Phi((l-l')T_d)\mathbf{a}_n\mathbf{a}_{n'}^H\right] = 0. \tag{A.29}$$

Therefore,

$$\int_{-\infty}^{\infty} h_{n,m}(\tau)\Phi(lT_d-\tau)d\tau = \sum_{l'=0}^{L-1} h_{n,m}(l')\Phi((l-l')T_d), \tag{A.30}$$

or, in the matrix form

$$\begin{bmatrix} \int_{-\infty}^{\infty}\Phi(-\tau)h_{n',m}(\tau)d\tau \\ \vdots \\ \int_{-\infty}^{\infty}\Phi((L-1)T_d-\tau)h_{n',m}(\tau)d\tau \end{bmatrix} = \mathbf{\Phi}\begin{bmatrix} h_{n',m}(0)d\tau \\ \vdots \\ h_{n',m}(L-1)d\tau \end{bmatrix}. \tag{A.31}$$

Extend (A.31) to the full form of $N\times M$ channel, the vector of modeled channel coefficients $\mathbf{h}$ is found as

$$\mathbf{h} = \begin{bmatrix} h_{1,1}(0) \\ \vdots \\ h_{N,M}(L-1) \end{bmatrix} = [\mathbf{I}_{NM}\otimes\mathbf{\Phi}]^{-1}\begin{bmatrix} \int_{-\infty}^{\infty}\Phi(-\tau)h_{1,1}(\tau)d\tau \\ \vdots \\ \int_{-\infty}^{\infty}\Phi((L-1)T_d-\tau)h_{N,M}(\tau)d\tau \end{bmatrix}. \tag{A.32}$$

The modeling error for SI channels from N Tx antennas to the m-th Rx antenna is calculated by

$$\begin{aligned}\epsilon_m^2 &= \frac{1}{K_1K_2}\bar{E}\left\{\left|\sum_{n=1}^{N}\int_{-\infty}^{\infty} h_{n,m}^*(\tau)X_n(t-\tau)d\tau - \sum_{n=1}^{N}\sum_{l=0}^{L-1} h_{n,m}^*(l)X_n(t-lT_d)\right|^2\right\} \\ &= \frac{1}{K_1K_2}\bar{E}\left\{\left[\sum_{n=1}^{N}\int_{-\infty}^{\infty} h_{n,m}^*(\tau)X_n(t-\tau)d\tau - \sum_{n=1}^{N}\sum_{l=0}^{L-1} h_{n,m}^*(l)X_n(t-lT_d)\right]\right. \\ &\quad\left.\cdot\left[\sum_{n'=1}^{N}\int_{-\infty}^{\infty} h_{n',m}(\tau')X_{n'}^*(t-\tau')d\tau' - \sum_{n'=1}^{N}\sum_{l'=0}^{L-1} h_{n',m}(l')X_{n'}^*(t-l'T_d)\right]\right\}.\end{aligned} \tag{A.33}$$

From (A.27), (A.33) becomes

$$\begin{aligned}
\epsilon_m^2 &= \sum_{n=1}^{N}\sum_{n'=1}^{N}\int_{-\infty}^{\infty}\int_{-\infty}^{\infty} h_{n,m}^*(\tau)\Phi(\tau-\tau')\mathbf{a}_n\mathbf{a}_{n'}^H h_{n',m}(\tau')d\tau d\tau' \\
&\quad - \sum_{n=1}^{N}\sum_{n'=1}^{N}\sum_{l'=0}^{L-1}\int_{-\infty}^{\infty} h_{n,m}^*(\tau)\Phi(\tau-l'T_d)\mathbf{a}_n\mathbf{a}_{n'}^H h_{n',m}(l')d\tau \\
&= \sum_{n=1}^{N}\sum_{n'=1}^{N}\int_{-\infty}^{\infty}\int_{-\infty}^{\infty} h_{n,m}^*(\tau)\Phi(\tau-\tau')\mathbf{a}_n\mathbf{a}_{n'}^H h_{n',m}(\tau')d\tau d\tau' \\
&\quad - \sum_{n=1}^{N}\sum_{n'=1}^{N}\sum_{l'=0}^{L-1}\sum_{l=0}^{L-1} h_{n,m}^*(l)\Phi((l-l')T_d)\mathbf{a}_n\mathbf{a}_{n'}^H h_{n',m}(l') \\
&= \sum_{n=1}^{N}\sum_{n'=1}^{N}\int_{-\infty}^{\infty}\int_{-\infty}^{\infty} h_{n,m}^*(\tau)\Phi(\tau-\tau')\mathbf{a}_n\mathbf{a}_{n'}^H h_{n',m}(\tau')d\tau d\tau' - \mathbf{h}_m^H[\mathbf{A}\otimes\mathbf{I}_L]\boldsymbol{\Theta}[\mathbf{A}^H\otimes\mathbf{I}_L]\mathbf{h}_m
\end{aligned} \tag{A.34}$$

where $\mathbf{h}_m = [h_{1,m}(0),\ldots,h_{N,m}(L-1)]^T$.

A.6 Derivation of Weighting Error Functions

From (6), we have

$$\begin{aligned}
\mathbf{w}_m(l,t+t_0) &= \frac{2\mu\alpha}{K_1K_2}\int_{t_0}^{t+t_0} e^{-\alpha(t+t_0-\tau)}\mathrm{Re}\Big\{\big[D_m(\tau)+S_{m,r}(\tau)+N_m(\tau)\big]e^{j2\pi f_c\tau}\Big\} \\
&\quad \cdot\mathbf{X}_r(\tau-lT_d)e^{j2\pi f_c(\tau-lT_d)}d\tau \\
&= \frac{\mu\alpha}{K_1K_2}\int_{t_0}^{t+t_0} e^{-\alpha(t+t_0-\tau)}\Big\{\big[D_m(\tau)+S_{m,r}(\tau)+N_m(\tau)\big]e^{j2\pi f_c\tau} \\
&\quad + \big[D_m^*(\tau)+S_{m,r}^*(\tau)+N_m^*(\tau)\big]e^{-j2\pi f_c\tau}\Big\}\mathbf{X}_r(\tau-lT_d)e^{j2\pi f_c(\tau-lT_d)}d\tau
\end{aligned} \tag{A.35}$$

where $D_m(t) = \sum_{l=0}^{L-1}\mathbf{h}_m^H(l)\mathbf{X}(t-lT_d) - \sum_{l=0}^{L-1}e^{-j2\pi f_c lT_d}\mathbf{w}_m^H(l,t)\mathbf{X}_r(t-lT_d)$ is the low-pass equivalent of the residual SI signal $d_m(t) = z_m(t) - y_m(t)$. Substituting $\mathbf{X}(t) = \mathbf{AS}(t)$ and $\mathbf{X}_r(t) = \mathbf{A}_r\mathbf{S}(t)$ into the expression of $D_m(t)$ and noting that $D_m(t)$ is a scalar function (hence $D_m^T(t) = D_m(t)$), we obtain

$$D_m^*(t) = \sum_{l=0}^{L-1}\mathbf{S}^H(t-lT_d)[\mathbf{A}^H\mathbf{h}_m(l) - \mathbf{A}_r^H e^{j2\pi f_c lT_d}\mathbf{w}_m(l,t)]. \tag{A.36}$$

Substituting (A.36) into (A.35), after some multiplications and noting that signal components centered about the frequency $2f_c$ are eliminated by the LPF whose bandwidth is

assumed to be very narrow compared to f_c, we get

$$\mathbf{w}_m(l,t+t_0)=\frac{\mu\alpha}{K_1K_2}\int_{t_0}^{t+t_0}e^{-\alpha(t+t_0-\tau)}\Big\{\sum_{l'=0}^{L-1}\mathbf{S}^H(\tau-l'T_d)[\mathbf{A}^H\mathbf{h}_m(l')-\mathbf{A}_r^He^{j2\pi f_cl'T_d}\mathbf{w}_m(l',\tau)] + S_r^*(\tau)+N^*(\tau)\Big\}\mathbf{A}_re^{-j2\pi f_clT_d}\mathbf{S}(\tau-lT_d)d\tau. \tag{A.37}$$

Multiplying both sides of (A.37) with $\mathbf{A}_r^He^{j2\pi f_clT_d}$ and defining $\mathbf{B}=\mathbf{A}_r^H\mathbf{A}_r$, we have

$$\mathbf{A}_r^He^{j2\pi f_clT_d}\mathbf{w}_m(l,t+t_0)=\frac{\mu\alpha}{K_1K_2}\int_{t_0}^{t+t_0}e^{-\alpha(t+t_0-\tau)}\Big\{\sum_{l'=0}^{L-1}\mathbf{S}^H(\tau-l'T_d)\Big[\mathbf{A}^H\mathbf{h}_m(l')- \mathbf{A}_r^He^{j2\pi f_cl'T_d}\mathbf{w}_m(l',\tau)\Big]+S_r^*(\tau)+N^*(\tau)\Big\}\mathbf{BS}(\tau-lT_d)d\tau. \tag{A.38}$$

Substituting the definition of $\mathbf{u}_m(l,t)=\mathbf{A}^H\mathbf{h}_m(l)-\mathbf{A}_r^He^{j2\pi f_clT_d}\mathbf{w}_m(l,\tau)$ into (A.38), we have

$$\mathbf{u}_m(l,t+t_0)=\mathbf{A}^H\mathbf{h}_m(l)-\frac{\mu\alpha}{K_1K_2}\int_{t_0}^{t+t_0}e^{-\alpha(t+t_0-\tau)}\Big[\sum_{l'=0}^{L-1}\mathbf{S}^H(\tau-l'T_d)\mathbf{u}_m(l',\tau) + S_r^*(\tau)+N^*(\tau)\Big]\mathbf{BS}(\tau-lT_d)d\tau. \tag{A.39}$$

Taking ensemble expectation on two sides of (A.39) and assuming that all the transmitted signals are independent to the received signals and noise, we have

$$\bar{\mathbf{u}}_m(l,t+t_0)=\mathbf{A}^H\mathbf{h}_m(l)-\frac{\mu\alpha}{K_1K_2}\int_{t_0}^{t+t_0}e^{-\alpha(t+t_0-\tau)}\sum_{l'=0}^{L-1}\mathbf{BS}(\tau-l'T_d)\mathbf{S}^H(\tau-lT_d)\bar{\mathbf{u}}_m(l',\tau)d\tau. \tag{A.40}$$

Taking time average over one symbol period T_s of $\bar{\mathbf{u}}_m(l,t+t_0)$ with respect to the starting time t_0, we obtain

$$\bar{\bar{\mathbf{u}}}_m(l,t)=\mathbf{A}^H\mathbf{h}_m(l)-\mu\alpha\int_0^t e^{-\alpha(t-\tau)}\sum_{l'=0}^{L-1}\mathbf{B}\boldsymbol{\Theta}((l-l')T_d)\bar{\mathbf{u}}_m(l',\tau)d\tau \tag{A.41}$$

where $\boldsymbol{\Theta}((l-l')T_d)=\Phi((l-l')T_d)\mathbf{I}_K$. In derivation of (A.41), $\bar{\mathbf{u}}_m(l,t)$ is assumed to change slowly and it can be seen as a constant during T_s, i.e., $\bar{\mathbf{u}}_m(l,t+t_0)\approx\bar{\bar{\mathbf{u}}}_m(l,t)=\frac{1}{T_s}\int_0^{T_s}\bar{\mathbf{u}}_m(l,t+t_0)dt_0$. Eq. (A.41) can be rewritten in the full form of L-taps as

$$\bar{\bar{\mathbf{u}}}_m(t)=(\mathbf{A}^H\otimes\mathbf{I}_L)\mathbf{h}_m-\mu\alpha\int_0^t e^{-\alpha(t-\tau)}\big[(\mathbf{B}\otimes\mathbf{I}_L)\boldsymbol{\Theta}\big]\bar{\bar{\mathbf{u}}}_m(\tau)d\tau. \tag{A.42}$$

Expanding (A.42) to all M Rx chains, we obtain the expected weighting error function vector as

$$\bar{\tilde{\mathbf{u}}}(t) = [\mathbf{I}_M \otimes (\mathbf{A}^H \otimes \mathbf{I}_L)]\mathbf{h} - \mu\alpha \int_0^t e^{-\alpha(t-\tau)} \Big\{ \mathbf{I}_M \otimes \big[(\mathbf{B} \otimes \mathbf{I}_L)\boldsymbol{\Theta} \big] \Big\} \bar{\tilde{\mathbf{u}}}(\tau) d\tau. \tag{A.43}$$

Denoting $\boldsymbol{\Psi} = \mathbf{I}_M \otimes \big[(\mathbf{B} \otimes \mathbf{I}_L)\boldsymbol{\Theta} \big]$ and $\underline{\mathbf{h}} = [\mathbf{I}_M \otimes (\mathbf{A}^H \otimes \mathbf{I}_L)]\mathbf{h}$, we obtain the final equation of $\bar{\tilde{\mathbf{u}}}(t)$ as in (6.21).

BIBLIOGRAPHY

[1] Cisco, "VNI Forecast and Methodology, 2017-2022," pp. 1–38, 2018.

[2] Z. Zhang, X. Chai, K. Long, A. V. Vasilakos, and L. Hanzo, "Full duplex techniques for 5G networks: Self-interference cancellation, protocol design, and relay selection," *IEEE Commun. Mag.*, vol. 53, no. 5, pp. 128–137, 2015.

[3] Y. S. Choi and H. Shirani-Mehr, "Simultaneous transmission and reception: Algorithm, design and system level performance," *IEEE Trans. Wireless Commun.*, vol. 12, no. 12, pp. 5992–6010, Oct. 2013.

[4] Z. Zhang, K. Long, A. V. Vasilakos, and L. Hanzo, "Full-duplex wireless communications: Challenges, solutions, and future research directions," *Proceedings of the IEEE*, vol. 104, no. 7, pp. 1369–1409, July 2016.

[5] T. Riihonen, D. Korpi, O. Rantula, H. Rantanen, T. Saarelainen, and M. Valkama, "In-band full-duplex radio transceivers: A paradigm shift in tactical communications and electronic warfare?" *IEEE Commun. Mag.*, vol. 55, no. 10, pp. 30–36, Oct 2017.

[6] A. Goldsmith and Andrea, *Wireless Communications*. Cambridge University Press, 2005.

[7] A. Sabharwal, P. Schniter, D. Guo, D. W. Bliss, S. Rangarajan, and R. Wichman, "In-band full-duplex wireless: Challenges and opportunities," *IEEE J. Sel. Areas Commun*, vol. 32, no. 9, pp. 1637–1652, Sept. 2014.

[8] D. Bharadia, E. McMilin, and S. Katti, "Full duplex radios," in *Proc. ACM SIGCOMM 2013*, Hong Kong, China, Aug. 2013, pp. 375–386.

[9] X. Huang and Y. J. Guo, "Radio frequency self-interference cancellation with analog least mean-square loop," *IEEE Trans. Microw. Theory Tech.*, vol. 65, no. 9, pp. 3336–3350, Sept. 2017.

[10] K. E. Kolodziej, B. T. Perry, and J. S. Herd, "In-band full-duplex technology: Techniques and systems survey," *IEEE Trans. Microw. Theory Techn.*, vol. 67, no. 7, pp. 3025–3041, July 2019.

[11] J. Choi, M. Jain, and K. Srinivasan, "Achieving single channel, full duplex wireless communication," in *Proc. 16th Annu. Int. Conf. Mobi. Commun.* Chicago, USA, Sept. 2010, pp. 1–12.

[12] M. Duarte, A. Sabharwal, V. Aggarwal, R. Jana, K. K. Ramakrishnan, C. W. Rice, and N. K. Shankaranarayanan, "Design and characterization of a full-duplex multiantenna system for WIFI networks," *IEEE Trans. Veh. Technol.*, vol. 63, no. 3, pp. 1160–1177, Mar 2014.

[13] B. Debaillie, D. J. Van Den Broek, C. Lavin, B. Van Liempd, E. A. M. Klumperink, C. Palacios, J. Craninckx, and B. Nauta, "RF self-interference reduction techniques for compact full duplex radios," in *IEEE Veh. Technol. Conf.*, vol. 2015, Glasgow, Scotland, 2015, pp. 1–5.

[14] E. Everett, A. Sahai, and A. Sabharwal, "Passive self-interference suppression for full-duplex infrastructure nodes," *IEEE Trans. Wireless Commun.*, vol. 13, no. 2, pp. 680–694, Feb. 2014.

[15] E. G. Tianang and D. S. Filipovic, "A dipole antenna system for simultaneous transmit and receive," in *IEEE Antennas Propag. Soc. AP-S Int. Symp.*, 2015.

[16] G. Makar, N. Tran, and T. Karacolak, "A high-isolation monopole array with ring hybrid feeding structure for in-band full-duplex systems," *IEEE Antennas Wireless Propag. Lett.*, 2017.

[17] J. M. Laco, F. H. Gregorio, G. Gonzalez, J. E. Cousseau, T. Riihonen, and R. Wichman, "Patch antenna design for full-duplex transceivers," in *EuCNC 2017 - Eur. Conf. Networks Commun.*, 2017.

[18] H. Nawaz and I. Tekin, "Three ports microstrip patch antenna with dual linear and linear co-polarisation characteristics," *Electron. Lett.*, vol. 53, no. 8, pp. 518–520, 2017.

[19] J. Wu, M. Li, and N. Behdad, "A Wideband, Unidirectional Circularly Polarized Antenna for Full-Duplex Applications," *IEEE Trans. Antennas Propag.*, vol. 66, no. 3, pp. 1559–1563, 2018.

[20] P. Deo, D. Mirshekar-Syahkal, G. Zheng, A. Pal, and A. Mehta, "Broadband antenna for passive self-interference suppression in full-duplex communications," in *2018 IEEE Radio Wireless Symp. (RWS)*, Jan 2018, pp. 243–245.

[21] A. T. Wegener and W. J. Chappell, "Coupled antenna scheme using filter design techniques and tunable resonators to show simultaneous transmit and receive," in *IEEE MTT-S Inter. Microw. Symp. Digest*, 2013.

[22] S. Khaledian, F. Farzami, B. Smida, and D. Erricolo, "Inherent self-interference cancellation for in-band full-duplex single-antenna systems," *IEEE Trans. Microw. Theory Tech.*, vol. 66, no. 6, pp. 2842–2850, June 2018.

[23] T. Snow, C. Fulton, and W. J. Chappell, "Transmit-receive duplexing using digital beamforming system to cancel self-interference," *IEEE Trans. Microw. Theory Techn.*, vol. 59, no. 12, pp. 3494–3503, Dec. 2011.

[24] E. Everett, C. Shepard, L. Zhong, and A. Sabharwal, "Softnull: Many-antenna full-duplex wireless via digital beamforming," *IEEE Trans. Wireless Commun.*, vol. 15, no. 12, pp. 8077–8092, Dec. 2016.

[25] T. Snow, C. Fulton, and W. J. Chappell, "Multi-antenna near field cancellation duplexing for concurrent transmit and receive," in *IEEE MTT-S Inter. Microw. Symp. Digest*, 2011.

[26] D. Korpi, T. Riihonen, V. Syrjälä, L. Anttila, M. Valkama, and R. Wichman, "Full-duplex transceiver system calculations: Analysis of ADC and linearity challenges," *IEEE Trans. Wireless Commun.*, vol. 13, no. 7, pp. 3821–3836, 2014.

[27] M. Adams and V. K. Bhargava, "Use of the recursive least squares filter for self interference channel estimation," in *IEEE Veh. Technol. Conf.*, 2016.

[28] L. Anttila, D. Korpi, E. Antonio-Rodriguez, R. Wichman, and M. Valkama, "Modeling and efficient cancellation of nonlinear self-interference in MIMO full-duplex transceivers," in *2014 IEEE Globecom Work. GC Wkshps 2014*, 2014.

[29] E. Ahmed, A. M. Eltawil, and A. Sabharwal, "Self-interference cancellation with nonlinear distortion suppression for full-duplex systems," in *Conf. Rec. - Asilomar Conf. Signals, Syst. Comput.*, 2013.

[30] K. Komatsu, Y. Miyaji, and H. Uehara, "Frequency-domain Hammerstein self-interference canceller for in-band full-duplex OFDM systems," in *IEEE Wireless Commun. Netw. Conf. WCNC*, 2017.

[31] F. H. Gregorio, G. J. Gonzalez, J. Cousseau, T. Riihonen, and R. Wichman, "Predistortion for power amplifier linearization in full-duplex transceivers without extra RF chain," in *ICASSP, IEEE Int. Conf. Acoust. Speech Signal Process. - Proc.*, 2017.

[32] X. Quan, Y. Liu, D. Chen, S. Shao, Y. Tang, and K. Kang, "Blind nonlinear self-interference cancellation for wireless full-duplex transceivers," *IEEE Access*, vol. 6, pp. 37 725–37 737, 2018.

[33] J. Li, H. Zhang, and M. Fan, "Digital self-interference cancellation based on independent component analysis for co-time co-frequency full-duplex communication systems," *IEEE Access*, vol. 5, pp. 10 222–10 231, 2017.

[34] H. Yang, H. Zhang, J. Zhang, and L. Yang, "Digital self-interference cancellation based on blind source separation and spectral efficiency analysis for the full-duplex communication systems," *IEEE Access*, vol. 6, pp. 43 946–43 955, 2018.

[35] J. Kim, M. S. Sim, M. Chung, D. K. Kim, and C.-B. Chae, *Full-duplex Radios in 5G: Fundamentals, Design and Prototyping*. John Wiley & Sons, Ltd, 2016, pp. 539–560. [Online]. Available: http://dx.doi.org/10.1002/9781119116493.ch22

[36] M. Duarte and A. Sabharwal, "Full-duplex wireless communications using off-the-shelf radios: Feasibility and first results," in *Conf. Rec. - Asilomar Conf. Signals, Systems Computers*, California, USA, Nov 2010, pp. 1558–1562.

[37] J. R. Krier and I. F. Akyildiz, "Active self-interference cancellation of passband signals using gradient descent," in *IEEE Int. Symp. Personal, Indoor Mobile Radio Commun., PIMRC*, 2013, pp. 1212–1216.

[38] K. E. Kolodziej, J. G. McMichael, and B. T. Perry, "Multitap RF canceller for in-band full-duplex wireless communications," *IEEE Trans. Wireless Commun.*, vol. 15, no. 6, pp. 4321–4334, June 2016.

[39] T. Huusari, Y. S. Choi, P. Liikkanen, D. Korpi, S. Talwar, and M. Valkama, "Wideband self-adaptive RF cancellation circuit for full-duplex radio: Operating prin-

ciple and measurements," in *Proc. 81st IEEE Veh. Technol. Conf. (VTC Spring)*, Glasgow, Scotland, May 2015, pp. 11–14.

[40] L. Zhang, M. Ma, and B. Jiao, "Design and implementation of adaptive multi-tap analog interference canceller," *IEEE Trans. Wireless Commun.*, vol. 18, no. 3, pp. 1698–1706, March 2019.

[41] J. Zhou, T.-H. Chuang, T. Dinc, and H. Krishnaswamy, "Integrated wideband self-interference cancellation in the RF domain for FDD and full-duplex wireless," *IEEE J. Solid-State Circuits*, vol. 50, no. 12, pp. 3015–3031, Dec. 2015.

[42] H. Krishnaswamy, G. Zussman, J. Zhou, J. Marasevic, T. Dinc, N. Reiskarimian, and T. Chen, "Full-duplex in a hand-held device - From fundamental physics to complex integrated circuits, systems and networks: An overview of the Columbia FlexICoN project," in *Conf. Rec. - Asilomar Conf. Signals, Syst. Comput.*, 2017.

[43] J. Zhou, N. Reiskarimian, J. Diakonikolas, T. Dinc, T. Chen, G. Zussman, and H. Krishnaswamy, "Integrated full duplex radios," *IEEE Commun. Mag.*, 2017.

[44] D. Korpi, J. Tamminen, M. Turunen, T. Huusari, Y. S. Choi, L. Anttila, S. Talwar, and M. Valkama, "Full-duplex mobile device: Pushing the limits," *IEEE Commun. Mag.*, vol. 54, no. 9, pp. 80–87, Sept. 2016.

[45] G. C. Alexandropoulos and M. Duarte, "Joint design of multi-tap analog cancellation and digital beamforming for reduced complexity full duplex MIMO systems," in *2017 IEEE Int. Conf. Commun. (ICC)*, May 2017, pp. 1–7.

[46] V. K. J. G.Proakis, *Digital Signal Processing using Matlab*. Thomson, 2010.

[47] B. Farhang-Boroujeny, *Adaptive Filters: Theory and Applications*. John Wiley & Sons, 2013.

[48] B. Widrow, P. E. Mantey, L. J. Griffiths, and B. B. Goode, "Adaptive antenna systems," *Proceedings of the IEEE*, vol. 55, no. 12, pp. 2143–2159, Dec 1967.

[49] A. Carusone and D. A. Johns, "Analogue adaptive filters: Past and present," *IEE Proceedings: Circuits, Devices and Systems*, 2000.

[50] J. P. Roesgen and G. H. Warren, "An analog front end chip for v.32 modems," in *1989 Proc. IEEE Custom Integrated Circuits Conference*, May 1989, pp. 16.1/1–16.1/5.

[51] O. Agazzi, D. Hodges, D. Messerschmitt, and W. Lattin, "Echo canceller for a 80kbs baseband modem," in *1982 IEEE Int. Solid-State Circuits Conf. Digest of Technical Papers*, vol. XXV, Feb 1982, pp. 144–145.

[52] F. Pecourt, J. Hauptmann, and A. Tenen, "An integrated adaptive analog balancing hybrid for use in ADSL modems," in *1999 IEEE Int. Solid-State Circuits Conf. Digest of Technical Papers. ISSCC. First Edition (Cat. No.99CH36278)*, Feb 1999, pp. 252–253.

[53] "IEEE Wireless LAN Medium Access Control (MAC) and Physical Layer (PHY) Specifications," *IEEE Std 802.11-1997*, 1997.

[54] Y. Nan, X. Huang, and Y. J. Guo, "A generalized continuous wave synthetic aperture radar," in *Proc. 85th IEEE Veh. Technol. Conf. (VTC Spring)*, Sydney, Australia, June 2017, pp. 1–5.

[55] A. Currie and M. A. Brown, "Wide-swath SAR," *IEE Proceedings F - Radar and Signal Processing*, vol. 139, no. 2, pp. 122–135, April 1992.

[56] A. Meta, "Signal processing of FMCW synthetic aperture radar data," Ph.D. dissertation, Delft University of Technology, Netherlands, Aug. 2006.

[57] B. Debaillie, D. J. Van Den Broek, C. Lavín, B. Van Liempd, E. A. M. Klumperink, C. Palacios, J. Craninckx, B. Nauta, and A. Pärssinen, "Analog/RF solutions enabling compact full-duplex radios," *IEEE J. Sel. Areas Commun.*, vol. 32, no. 9, pp. 1662–1673, 2014.

[58] A. T. Le, L. C. Tran, and X. Huang, "On performance of analog least mean square loop for self-interference cancellation in in-band full-duplex OFDM systems," in *Proc. 85th IEEE Veh. Technol. Conf. (VTC Spring)*, Sydney, Australia, June 2017, pp. 1–5.

[59] ——, "Cyclostationary analysis of analog least mean square loop for self-interference cancellation in in-band full-duplex systems," *IEEE Commun. Lett.*, vol. 21, no. 12, pp. 2738–2741, Sept. 2017.

[60] T. K. Moon and W. C. Stirling., *Mathematical Methods and Algorithms for Signal Processing*. New Jersey, USA: Prentice Hall, Jun 2000.

[61] A. T. Le, L. C. Tran, X. Huang, Y. J. Guo, and J. C. Vardaxoglou, "Frequency domain characterization and performance bounds of ALMS loop for RF self-interference cancellation," *IEEE Trans. Commun.*, vol. 67, no. 1, pp. 682–692, Jan. 2019.

[62] M. Sakai, H. Lin, and K. Yamashita, "Self-interference cancellation in full-duplex wireless with IQ imbalance," *Phys. Commun.*, vol. 18, no. P1, pp. 2–14, Mar. 2016.

[63] D. Korpi, L. Anttila, V. Syrjälä, and M. Valkama, "Widely linear digital self-interference cancellation in direct-conversion full-duplex transceiver," *IEEE J. Sel. Areas Commun.*, vol. 32, no. 9, pp. 1674–1687, Sept. 2014.

[64] Y. Pan, C. Zhou, G. Cui, W. Wang, and X. Li, "Self-interference cancellation with RF impairments suppression for full-duplex systems," in *Proc. 82nd IEEE Veh. Technol. Conf. (VTC-Fall)*, Boston, USA, Sept. 2015, pp. 1–5.

[65] F. Shu, J. Wang, J. Li, R. Chen, and W. Chen, "Pilot optimization, channel estimation, and optimal detection for full-duplex OFDM systems with IQ imbalances," *IEEE Trans. Vehicular Technol.*, vol. 66, no. 8, pp. 6993–7009, Aug 2017.

[66] H. Yu, F. Shu, Y. You, J. Wang, T. Liu, X. You, J. Lu, J. Wang, and X. Zhu, "Compressed sensing-based time-domain channel estimator for full-duplex OFDM systems with IQ-imbalances," *Science China Information Sciences*, vol. 60, no. 8, p. 082303, Mar 2017. [Online]. Available: https://doi.org/10.1007/s11432-016-0386-x

[67] A. T. Le, Y. Nan, L. C. Tran, X. Huang, Y. J. Guo, and Y. Vardaxoglou, "Analog least mean square loop for self-interference cancellation in generalized continuous wave SAR," in *Proc. IEEE 88th Vehicular Technol. Conf. (VTC-Fall)*, Aug 2018, pp. 1–5.

[68] J. G. Andrews, S. Buzzi, W. Choi, S. V. Hanly, A. Lozano, A. C. K. Soong, and J. C. Zhang, "What will 5G be?" *IEEE J. Sel. Areas Commun.*, vol. 32, no. 6, pp. 1065–1082, June 2014.

[69] F. Boccardi, R. W. Heath, A. Lozano, T. L. Marzetta, and P. Popovski, "Five disruptive technology directions for 5G," *IEEE Commun. Mag.*, vol. 52, no. 2, pp. 74–80, Feb. 2014.

[70] M. Agiwal, A. Roy, and N. Saxena, "Next generation 5G wireless networks: A comprehensive survey," *IEEE Commun. Surv. Tutor.*, vol. 18, no. 3, pp. 1617–1655, 2016.

[71] S. Goyal, P. Liu, S. S. Panwar, R. A. Difazio, R. Yang, and E. Bala, "Full duplex cellular systems: will doubling interference prevent doubling capacity?" *IEEE Commun. Mag.*, vol. 53, no. 5, pp. 121–127, May 2015.

[72] J. Koh, Y. Lim, C. Chae, and J. Kang, "On the feasibility of full-duplex large-scale MIMO cellular systems," *IEEE Trans. Wireless Commun.*, vol. 17, no. 9, pp. 6231–6250, Sept. 2018.

[73] G. Zheng, "Joint beamforming optimization and power control for full-duplex MIMO two-way relay channel," *IEEE Trans. Signal Process.*, vol. 63, no. 3, pp. 555–566, Feb. 2015.

[74] D. W. Bliss, P. A. Parker, and A. R. Margetts, "Simultaneous transmission and reception for improved wireless network performance," in *2007 IEEE/SP 14th Workshop Statistical Signal Process.*, Aug 2007, pp. 478–482.

[75] T. Riihonen, S. Werner, and R. Wichman, "Mitigation of loopback self-interference in full-duplex MIMO relays," *IEEE Trans. Signal Process.*, vol. 59, no. 12, pp. 5983–5993, Dec. 2011.

[76] E. Aryafar, M. A. Khojastepour, K. Sundaresan, S. Rangarajan, and M. Chiang, "MIDU: Enabling MIMO full duplex," in *Proc. Ann. Inter. Conf. Mobile Comput. Netw.*, ser. Mobicom '12. New York, NY, USA: ACM, 2012, pp. 257–268. [Online]. Available: http://doi.acm.org/10.1145/2348543.2348576

[77] J. P. Doane, K. E. Kolodziej, and B. T. Perry, "Simultaneous transmit and receive performance of an 8-channel digital phased array," in *2017 IEEE Int. Sympo. Antennas Propag. USNC/URSI Nat. Radio Science Meeting*, July 2017, pp. 1043–1044.

[78] D. Bharadia and S. Katti, "Full duplex MIMO radios," in *Proc. 11th USENIX Conf. Networked Systems Design Implementation*, ser. NSDI'14. Berkeley, CA, USA: USENIX Association, 2014, pp. 359–372. [Online]. Available: http://dl.acm.org/citation.cfm?id=2616448.2616482

[79] Y. Liu, D. Liu, X. Li, and C. Huang, "Multi-tap analog MIMO self-interference cancellation for full-duplex communications," in *2017 9th Int. Conf. Wireless Commun. Signal Process. (WCSP)*, Oct. 2017, pp. 1–6.

[80] H. Iimori and G. Thadeu Freitas de Abreu, "Two-way full-duplex MIMO with hybrid TX-RX MSE minimization and interference cancellation," in *2018 IEEE 19th Int. Workshop Signal Process. Advances Wireless Commun. (SPAWC)*, June 2018, pp. 1–5.

[81] A. T. Le, L. C. Tran, X. Huang, and Y. J. Guo, "Analog least mean square loop with I/Q imbalance for self-interference cancellation in full-duplex radios," *IEEE Trans. Vehicular Technol.*, vol. pp, no. 99, pp. 1–13, 2019.

[82] H. Iimori, G. Abreu, and G. C. Alexandropoulos, "MIMO beamforming schemes for hybrid SIC FD radios with imperfect hardware and CSI," *IEEE Trans. Wireless Commun.*, pp. 1–1, 2019.

[83] M. A. Islam, G. C. Alexandropoulos, and B. Smida, "A unified beamforming and A/D self-interference cancellation design for full duplex MIMO radios," in *IEEE Int. Symp. Personal, Indoor Mobile Radio Commun.*, Sep 2019, pp. 1–5.

[84] F. J. Kub and E. W. Justh, "Analog cmos implementation of high frequency least-mean square error learning circuit," *IEEE J. Solid-State Circuits*, vol. 30, no. 12, pp. 1391–1398, Dec 1995.

[85] J. E. Perez-Carmona, H. M. Perez-Meana, and J. C. Sanchez-Garcia, "Analog adaptive filter LMS algorithm using CMOS 0.5 μm technology," *WSEAS Trans. Circuits Syst.*, 2008.

[86] J. Bryant, "Multipliers vs. Modulators," https://www.analog.com/media/en/analog-dialogue/volume-47/number-2/articles/multipliers-vs-modulators.pdf, Last accessed on 2019-12-19.

[87] L. C. Tran, T. A. Wysocki, J. Seberry, A. Mertins, and S. S. Adams, "Novel constructions of improved square complex orthogonal designs for eight transmit antennas," *IEEE Trans. Inf. Theory*, vol. 55, no. 10, pp. 4439–4448, Oct 2009.

[88] L. C. Tran, A. Mertins, and T. A. Wysocki, "Unitary differential space-time-frequency codes for MB-OFDM UWB wireless communications," *IEEE Trans. Wireless Commun.*, vol. 12, no. 2, pp. 862–876, February 2013.

[89] ——, “Cooperative communication in space-time-frequency coded MB-OFDM UWB,” in *Proc. IEEE 68th Vehicular Technol. Conf.*, Sep. 2008, pp. 1–5.

[90] M. Sudjai, L. C. Tran, and F. Safaei, “Performance analysis of STFC MB-OFDM UWB in WBAN channels,” in *Proc. IEEE 23rd Int. Symp. Personal, Indoor Mobile Radio Commun. - (PIMRC)*, Sep. 2012, pp. 1710–1715.